DESIGN AND FABRICATION OF MEMBRANE-BASED PRESSURE SENSOR FOR CAPILLARY PRESSURE MEASUREMENT IN MICROMODELS

by

Nishagar Raventhiran

A thesis submitted in partial fulfillment
of the requirements for the degree

of

Master of Science

in

Mechanical Engineering

MONTANA STATE UNIVERSITY
Bozeman, Montana

July 2021

ACKNOWLEDGEMENTS

I am sincerely grateful to all those who have made this work possible. Foremost, I would like to express my sincere gratitude to my advisor Professor Yaofa Li for his encouragement, trust and support throughout this research. I would also like to thank my thesis reading committee: Professor Sarah Codd and Professor Eric Johnson for their effort in reviewing this work and their advices and clarifying remarks.

I would like to extend my appreciation to Montana Micro Fabrication facility, and staff members Andrew Lingley and Joshua Heinemann for the discussion and help with soft lithography process. Also, I would like to thank Razin Sazzad Molla, my laboratory colleague for sharing the invaluable ideas and helping with setting up the experimental apparatus with me.

Finally, I wish to express my sincere appreciation to my parents, brother and sister for their continuous and unconditional love and support.

TABLE OF CONTENTS

1. INTRODUCTION 1

1.1 Motivation 1
1.2 Objectives 5
1.3 Thesis Outline 5

2. LITREATURE REVIEW 6

2.1 Membrane design 6
2.2 Quantification of membrane deflection 9
2.3 Other Alternative Designs 16

3. EXPERIMENTAL DESCRIPTION 20

3.1 Pressure Sensor Design 20
3.1.1 The three-layer design 20
3.1.2 Mechanics of Thin PDMS membrane 21
3.1.3 Astigmatic particle tracking 23

3.2 Fabrication 25
3.2.1 Microchannel fabrication 25
3.2.2 Particle embedded membrane fabrication 34
3.2.3 Pressure tap fabrication 37
3.2.4 Assembling the micromodel 40

3.3 Image Acquisition 41
3.3.1 Optical setup 41
3.3.2 Image Acquisition 44

3.4 Calibration 45
3.4.1 Z position Calibration 45
3.4.2 Pressure Calibration 46

3.5 Image Analysis 48

4. RESULTS AND DISCUSSION 51

4.1 Pressure-Deflection Relation 51
4.2 Single-Phase flow 53
4.3 Multi-Phase flow 59

TABLE OF CONTENTS CONTINUED

4.4 Sensor stability Test 62

5. CONCLUSION AND FUTURE WORKS 64

5.1 Conclusion.....64
5.2 Recommendations for future work.....65

REFERENCES CITED.....66

APPENDICES 70

APPENDIX A: Profilometer readings 71
APPENDIX B: MATLAB code used for flowrate experiments.....74
APPENDIX C: MATLAB code used for flowrate experiments.....78
APPENDIX D: Uncertainty analysis for Single Phase flow- Air.....82
APPENDIX E: Uncertainty analysis for Single Phase flow- DI Water.....87

LIST OF FIGURES

Figure Page

2.1. Schematic illustrating a typical three-layer design of a membrane-based pressure sensor by Song et al. [18]. In this specific design the membrane deflection is characterized using interferometry as illustrated by the light rings at the bottom of the schemat……....….7

2.2. a) A pressure sensor design with a venting hole incorporated to increase measurement sensitivity, (b) top view of the sensor design, and (c) a photo of a real optofluidic chip fabricated in PDMS [19]. 8

2.3. Schematic of a multilayer PDMS sensor with auxiliary channels connecting pressure taps and the main flow channel [18]**. .....**.....8

2.4. a) A 2-D multiplex design for fluid pressure measurement by Orth et al. b) Pressure map of a steady state fluid flow with red and blue colors indication high and pressure, respectively [18]**. .....**.....9

2.5. Illustration of the design by Chung et al.: a) top view of the microdevice with flow channel, sensing channel and particle suspension channel. b) and c) illustrate the behavior of sensing chamber when the pressure is at atmospheric pressure and increased respectively. d) and e) are the top views of the sensing chamber deflection from its initial position [20]. 11

2.6. a) Working principle of the image contrast-based pressure sensor. b) The Z-scanning setup for measuring the distance between the glass-air and air-PDMS interfaces [17]. 13

2.7. Schematic of an ultra-thin high sensitive capacitive pressure sensor which mechanically coupled with a pressure sensing diaphragm [28].....15

2.8. Schematic of Fiber-Perot sensor by Zariko et al. [39] 16

2.9. Principle of Fiber Bragg Grating sensor and output of Fiber Bragg Grating [30].....17

2.10. Working principle of EFPI [30].....18

LIST OF FIGURES CONTINUED

Figure Page

3.1: (a) A schematic diagram illustrating the three-layer design of our pressure sensor with pressure taps within the supporting layer, the thin membrane and the microchannel layer shown from left to right; (b) the side view and top view of the three layer design and (c) the top view and side view of a pressure tap with a deformed membrane. 21

3.2. Example of a 3-D plot of the clamped circular membrane deflection (w(r)) as a function of radial coordinate (r) and polar angle (θ) for an applied pressure (P) of 1 kPa, with 100 μm membrane radius (a) and 5 μm membrane thickness (t) in cartesian plane. 22

3.3. The cylindrical lens attached to the microscope adaptor 24

3.4. The schematic representation of image astigmatism [32]. 24

3.5 The microchannel photomask consisting of four individual microchannels, of which three are 300 μm wide, one is 500 μm wide each with a 100 μm wide microchannel in the middle 26

3.6. Schematic diagram of a micromodel with microchannel and pressure taps (in colored circles) overlaid in the same plane for illustrative purpose. The narrow microchannel (L = 1.96 cm, h = 122.7 μm, w = 119.5 μm), within which the viscous pressure drop was measured to test the feasibility and sensitivity of the pressure sensors 27

3.7. Steps to fabricate the master using SU-8 on a silicon wafer.....29

3.8. Setup for the UV exposure step with a coated wafer sitting in the middle of the stage. 29

3.9. Cylindrical PVC container covered with plastic film tape. 30

3.10. Silicon wafer placed in the center of the cylindrical PVC container 31

3.11.The PVC container being degassed in the vacuum desiccator to remove the air bubbles in the PDMS solution. 32

3.12. Individual microchannels cut out from the cured PDMS slab. 33

3.13. Steps for PDMS molding based on the SU-8 maser. 33

LIST OF FIGURES CONTINUED

Figure Page

3.14. A complete microchannel fabricated from PDMS within inlet and outlet ports punched. 34

3.15. Flow diagram illustrating the spin coating procedure. 34

3.16. The Chemat Technology spin coater used to spin coat the PDMS membrane. 36

3.17. Relation of coating thickness (μm) as a function of spinning speed (RPM) (reproduced based on the data by [31]). 36

3.18. (a) The photomask design of pressure taps for four devices. Three of four devices have pressure taps of 200 μm in diameter and one has pressure taps of 300 μm in diameter. (b) design of one tile with pressure taps of 200 μm in diameter and (c) zoomed in view of 200 μm diameter pressure taps. 38

3.19. Setup for the fabrication of pressure taps using Norland Optical Adhesive 81. 39

3.20. Three-axis aligning system used to bond the microchannel with membrane to the glass substrate with pressure taps. The three-axis stage on the bottom is used to finely adjust the relative position of the pressure tap and microchannel layers, and the USB optical microscope on the top is used to guide this alignment process. 40

3.21. Final assembled micromodel. The inlet and outlet delivery ports were first attached to a clean microscope slide, on which two through hole were drilled and the microscope slides with attached delivery port were then bonded to the micromodel. 41

3.22. Schematic of the optical setup of the experiment. The green lines indicate the path of excitation light from the LED and the red lines indicate the path of fluorescence emitted by the particles. 43

3.23. Experimental setup showing the micromodel, the microscope, the camera and the LED controller. 43

LIST OF FIGURES CONTINUED

Figure Page

3.24. An example image capture using the aforementioned optical setup. The image is cropped to show the region of interest (ROI) better. The two ovals indicate the locations of the pressure taps and the rectangular channels are the venting channels connected to the atmosphere. The bright spots are images of fluorescent particles, which display different shapes depending on their distance from the microscope objective lens. 44

3.25. Representative particle images captured at different z locations: a) the initial position (0 μm); b) 20 μm away from the initial position, c) 50 μm away from the initial position. The shapes of the fluorescent particles change from vertical elongation to horizontal elongation as the objective is moved closer. 46

3.26. A schematic diagram of the setup used for pressure calibration. 47

3.27. Two representative images captured at reference pressure of 0 Pa (a), and a pressure of 2502 Pa (b), respectively. The change in shape of the fluorescent particles from vertical elongation to horizontal elongation can be observed. 48

3.28. The ROI selected for image analysis as indicted by the yellow box. 49

3.29. Cross-correlation coefficients between on pressure calibration image and all Z position calibration images. The location of the peak value represents the corresponding Z-position of the membrane under the applied pressure. 50

4.1. Calibrated relationship between pressure (kPa) and membrane deflection (μm) obtained for the 200 μm downstream pressure tap 52

4.2. Schematic of the viscous drop pressure measurement setup. The flowrate is controlled by the syringe pump connected to the inlet of the microchannel. The outlet is opened to atmosphere. The pressure drop across the microchannel is also measured with a differential pressure transducer. 53

LIST OF FIGURES CONTINUED

Figure Page

4.3. Pressure drops at various flow rates obtained using our sensor (blue symbols), the pressure transducer (green symbols) and theoretical prediction (red lines) for the single-phase air flow in the microchannel at various flowrates. The "Up" and "Down" plots correspond to increasing and decreasing flowrate measurements, respectively, and the dashed lines are the upper and lower bounds of the theoretical predictions based on propagated errors, which is approximately 4.4% of the predicted values. 56

4.4. Similar to Figure 4.3 but using water as the working fluid. Again, the dashed lines are the upper and lower bounds of the theoretical predictions based on propagated errors, which is approximately 4.4% of the predicted values. 58

4.5. (a) To measure the static contact angle, 20 μL of DI water is dispensed onto the surface of a PDMS slab to form a sessile droplet and images of the droplet shape were captured using a USB microscope (Koolertron, AS-SMXW33) viewing from the side. And the contact angle was measured in ImageJ using the "Drop Analysis" plugin. (b) To measure the receding contact angle, the same setup was used. The only difference is that the droplet shape was imaged as water was being withdrawn from the droplet using a pipette, which led to a shrinking droplet, generating the receding contact angle at the droplet edge. The static and receding contact angles are 110^{o} and 60°, respectively. 60

4.6. a) when the air – DI water interface is in the 100 μm narrow channel. b) when the air- DI water interface exiting the 100 μm narrow channel, c) and d) are the acquired particle shape corresponding to each interface locations. The arrow indicate the flow direction. 61

4.7. The Pressure - deflection calibration curves obtained for the same device on two consecutive days.....63

A.1. Profilometer measurement for height of the microchannel, which was 121.8 μm.....72

A.2. Profilometer measurement for width of the microchannel, which was 120.9 μm.....72

LIST OF FIGURES CONTINUED

Figure Page

A.3. Profilometer measurement for thickness of the membrane, which turns out to have a uniform thickness of 4.76 μm 73

D.1. Error analysis of Pressure vs. deflection curve for downstream pressure tap....83

D.2. Error analysis of Pressure vs. deflection curve for upstream pressure tap....84

D.3. Error analysis of Pressure drop vs. flowrate for downstream pressure tap 85

D.4. Error analysis of Pressure drop vs. flowrate for upstream pressure tap....85

D.5. Error propagation from theoretical calculation of rectangular channel 86

D.6. Uncertainty analysis of pressure drop vs. flowrate for Air 86

E.1. Error analysis of Pressure drop vs. flowrate for downstream pressure tap....88

E.2. Error analysis of Pressure drop vs. flowrate for upstream pressure tap 88

E.3. Error propagation from theoretical calculation of rectangular channel....89

E.4. Uncertainty analysis of pressure drop vs. flowrate for DI water....89

GLOSSARY

Abbreviations

1D..... One-Dimensional

2D..... Two-Dimensional

CMOS ..... Complementary Metal Oxide Semiconductor

DAQ..... Data Acquisition system

DI ..... Deionized

EFPI ..... Extrinsic Fiber Fabry-Perot

EMS ..... Electronic Micro System

FOV..... Field of view

FP ..... Fabry-Perot

Fps..... Frame per second

LED..... Light Emitting Diode

M-LEFT ..... Microfluidics Lab for Energy and Fluid Transport

MMF ..... Montana Micro Fabrication

MZ..... Mach-Zehnder

NA..... Numerical Aperture

NI .....National Instruments

PCC..... Phantom Camera Control

PDMS..... Polydimethylsiloxane

PVC..... Polyvinyl Chloride

GLOSSARY CONTINUED

ROI..... Region of interest

RMSD ..... Root Mean- Square Deviation

Si ..... Silicone

SMF..... Single mode filter

SNR..... Signal-to-Noise ratio

SSP..... Single-side Polished

TBA..... Tert Butyl Alcohol

UV..... Ultraviolet

Greek Letters

θ..... Contact Angle

σ ..... Surface Tension

μ ..... Dynamic Viscosity

ρ.....Density

ν.....Poisson's ratio

$\bar{\omega}$..... Average velocity

π..... Pi Constant

Symbols

a..... Radius

d..... Depth / Height

GLOSSARY CONTINUED

D ..... Flexural Rigidity

E ..... Young's Modulus

g ..... Gravitational Acceleration

h ..... Height

H ..... Height

L ..... Length

p^c ..... Capillary Pressure

Q ..... Flowrate

r ..... Radial Coordinate

R^2 ..... Square of the correlation coefficient

t ..... Thickness of membrane

w ..... width

$w(r)$ ..... Clamped circular membrane deflection

ABSTRACT

Pressure is a fundamental quantity in virtually all problems in fluid dynamics from macro-scale to micro/nano scale flows. Although technologies are well developed for its measurement at the macro-scale, pressure quantification at the microscale is still not trivial. Yet, precise pressure mapping at microscale such as in microfluidics is imperative in a variety of applications, including porous media flows and biomedical engineering. In particular, pore-scale capillary pressure is a defining variable in multiphase flow in porous media and has rarely been directly measured. To that end, this study aims to design and fabricate an on-chip sensor that enables quantification of capillary pressure in microfluidic porous media, called micromodels. The micromodel is fabricated in polydimethylsiloxane (PDMS) using soft lithography with a thin membrane incorporated that deflects with pressure variations in the fluid flow. Employing a microscope coupled with a high-speed camera and the astigmatism particle tracking principle, precise pressure measurement is achieved with an accuracy of ~ 60Pa. This sensor is then applied to characterize the viscous pressure drop in single phase flows, and the capillary pressure in a water-air multiphase in microchannels, and good agreement is obtained between the sensor measurement, theoretical values and measurements employing a commercial pressure transducer. This thesis provides a novel method for *in-situ* quantification of local pressure and potentially 2D pressure field in microfluidics and thus opens the door to a renewed understanding of pore-scale physics of multiphase flow in porous media.

CHAPTER 1

INTRODUCTION

1.1 Motivation

Pressure is a fundamental quantity of interest in fluid mechanics to describe and understand various flow characteristics. Particularly, in microfluidic devices and systems, accurate measurement and control of pressure with high spatial and temporal resolutions are key to numerous scientific and engineering applications ranging from evaluation of capillary pressure in enhanced oil recovery to sample manipulation in biological studies [1 - 5]. For instance, capillary pressure and capillarity are central to the description of multiphase flow in porous media [6 - 13]. Over decades, practical and theoretical descriptions of multiphase flow in porous media have been inevitably relying on empirical relations between capillary pressure and phase saturation, which have long been recognized to be hysteretic. Extensive studies have been devoted to understanding and mitigating such hysteresis in hope of achieving a unique description of the state of the porous medium flow system. In such an effort, direct *in-situ* measurement of pore-scale capillary pressure would be extremely valuable to identify new physics as well as to validated new hypotheses. In biomedical studies, the changes in rheological properties of red blood cells and white blood cells in the microchannel flows have been shown to give rise to pressure fluctuations, suggesting that accurate pressure measurement in microscale blood flow can be informative for the medical diagnosis of various diseases [14]. As another example, in heat transfer studies such as flow boiling in microchannels, local vapor pressure in a bubble plays a crucial role in the bubble growth and departure dynamics, and thus defines the overall heat transfer performance [15].

Despite its critical importance, measurement of pressure in microfluidic devices with high accuracy yet without significantly disturbing the flows can be extremely challenging primarily due to the small sizes of typical microfluidic devices and systems. Moreover, in many applications, such as the quantification of capillary pressure in multiphase flow in porous media, single-point pressure measurement is insufficient. Instead it is often desirable in these scenarios to map the instantaneous variations of 2D pressure fields with high spatial and temporal resolutions (*i.e.*, multiplex pressure measurement), adding another layer of complexity to this problem.

To overcome these challenges, a number of on-chip pressure measurement methods have been developed over the past couple of decades. As reviewed and discussed in detail in Chapter 2, these methods are based on various principles. For instance, there is one design called a differential manometer by Abkarian et al. [14], where the pressure is measured based on the displacement of the interface of two immiscible fluids. Alternatively, pressure has also been measured by monitoring the compression of a trapped air bubble [16] in microchannels.

Probably the most popular approach is the membrane design. The general idea is to have a thin membrane as a sensing layer which deflects subject to pressure variation, due to fluid flow through a microchannel. A typical membrane-based design consists of three layers: a bottom layer called sensing chamber with pressure taps whose depth can range from few tens to hundreds of micrometers, a sensing membrane with a thickness ranging from a few to tens of micrometers, and a top layer with the designed microchannel whose depth can range from a few hundred micrometers to a few millimeters depending on the specific purpose of the microchannel. Some designs incorporate circular side ports that are connected to the flow channel [18], while others put circular chambers directly on either top or bottom of the flow channel to detect the deflection

[17,19,20]. To quantify the membrane deflections, various approaches have been proposed and tested, which can be classified into two main categories: the optical and the electrical schemes. The optical readout scheme often involves using a microscope and a camera to measure quantitively the deflection of the membrane. The electrical scheme is based on the measurement of electrical signals, where electrodes are deposited onto the sensing membrane, and its deformation is quantified through the change of its resistance [21], or capacitance, [22]. By employing a pre-calibrated relationship between the applied pressure and the membrane deflection, the *in-situ* pressure can be inferred.

While these previous methods and designs have greatly improved our capability to characterize pressure in microfluidic devices, our survey of literature suggests that a few desirable features that are critical to our application (*i.e.*, multiphase flow in porous media) are still lacking from the previous designs. For instance, although a couple of previous design are able to perform multiplex measurement, the number of measurement locations and thus the spatial resolution are relatively low. And most other designs essentially only perform single-point measurements as opposed to pressure field measurement. Additionally, most previous designs require auxiliary channels for signal readout, which can reduce the device responsiveness as well as complicate the fabrication process. Moreover, previous designs (electrically or optically based) often require complex electrical control or expensive optical equipment and complicated imaging processing to detect membrane displacement. Therefore, new designs are needed not only to address our specific need, but also to satisfy the needs in a much broader range of applications by offering simpler fabrication, easier implementation, better versatility, and higher accuracy.

It is also worth noting that although a number of miniature pressure sensors are commercially available with the advancement of technology including piezoresistive, capacitive, optical, Fabry Perot (FP) interferometric and optofluidic pressure sensors [17], it is usually hard to integrate such sensors directly into microfluidic devices because of their relatively large sizes and the multistep fabrication processes required to fabricate a microfluidic device.

To that end, we aim to design and fabricate an on-chip sensor that enables direct pressure measurement in 1D microchannels and potentially in 2D microfluidic porous media called micromodels. The microfluidic device used herein is fabricated in polydimethylsiloxane (PDMS) using soft lithography with a thin membrane incorporated which deflects subject to pressure variations in the fluid flow. With this technique, pressure drop for single and multiphase flow in a microchannel can be inferred through a pre-calibrated correlation between the membrane deflection and pressure change. This method uses a high-speed camera and a microscope as an optical readout, allowing for possible simultaneous quantification of other flow characteristics, such as velocity fields, phase distribution and interfacial area. In this research, we hope to provide a novel method for direct quantification of viscous pressure drop and capillary pressure at the pore scale, which will potentially lead to a renewed understanding of pore-scale physics of multiphase flow in porous media.

1.2 Objectives

Our goal of this research is to fabricate a microfluidic pressure sensor by means of simple soft lithography to achieve fast and precise pressure measurement in 1D microchannels. The membrane deflection will be detected through the incorporation of the innovative astigmatic particle tracking scheme. Additionally, we aim to pave the way for 2D pressure field mapping in a 2D porous micromodel by a laying out a workable plan.

1.3 Thesis Outline

The rest of this thesis is organized as follow. Chapter 2 presents a detailed review of state of the art. Chapter 3 details the pressure sensor design, fabrication method, image acquisition, calibration and image analysis. Chapter 4 presents the stability and sensitivity evaluation of the pressure sensor as well as applications of the designed sensor to measure pressure drops in single-phase and multiphase flows. Finally, conclusions and recommendations for future work are presented in Chapter 5.

CHAPTER 2

LITREATURE REVIEW

Given its close relevance to the current work, this literature review will focus on the membrane-based pressure sensors. The basic principle of such a design is to measure optically or electrically the mechanical deformation of a membrane subject to an external pressure. The applied pressure can then be quantified by applying a pre-defined relation between pressure and membrane deflection that is determined beforehand either theoretically or empirically (*i.e.*, calibration). Below we will review a few representative designs of the sensing membrane, and representative approaches for membrane deflection quantification.

2.1 Membrane design

The sensing membrane has been designed and fabricated using various materials, with silicon [23] and PDMS [17 - 20] among the most common ones for their low cost and ease of fabrication. As mentioned previously, a typical sensor design with PDMS consists of three layers: a bottom layer with pressure taps called sensing chambers made of a PDMS slab, a sensing PDMS membrane with a thickness ranging from a few to tens of micrometers, and a top layer with the designed microchannel again made of a PDMS whose thickness can range from a few hundred micrometers to a few millimeters depending on the specific purpose of the microchannel. The three layers are then bonded by the plasma bonding method. Some designs incorporate circular side ports that are connected to the flow channel [18], while others put circular sensing chambers directly on either top or bottom of the flow channel to detect the deflection [17,19,20]. Figure 2.1 shows the schematic diagram of such a design as an example [19].

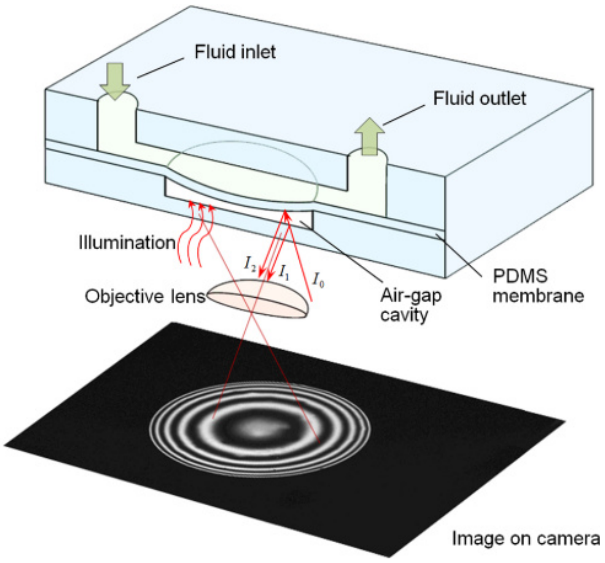

Figure 2.1. Schematic illustrating a typical three-layer design of a membrane-based pressure sensor by Song et al. [19]. In this specific design the membrane deflection is characterized using interferometry as illustrated by the light rings at the bottom of the schematic.

It is worth noting that although the sensing chambers are closed in most designs, a venting hole can be created to connect the sensing chamber to the atmosphere as shown in Figure 2.2, so that the pressure inside the sensing chamber remains constant all the time, which has been shown to increase the measurement sensitivity [19]. Another feature that is typically incorporated into the design are auxiliary channels for readout, as illustrated in Figure 2.3. These auxiliary or branch channels effectively move the pressure taps from directly above or below the microchannel to a relatively remote location, which helps to facilitate the characterization of the membrane deflection. However, a drawback of this design is that, extra dead volume is introduced due to the addition of the auxiliary channels, which may interfere with the processes occurring in the target channel. Additionally, the auxiliary channels separate pressure tap apart from the point of interest, which can reduce the responsiveness of the sensor.

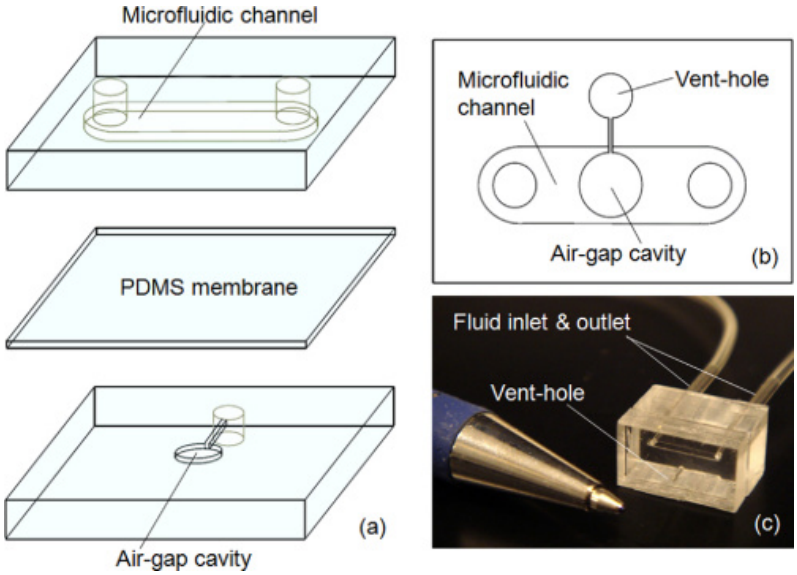

Figure 2.2. a) A pressure sensor design with a venting hole incorporated to increase measurement sensitivity, (b) top view of the sensor design, and (c) a photo of a real optofluidic chip fabricated in PDMS [19].

.

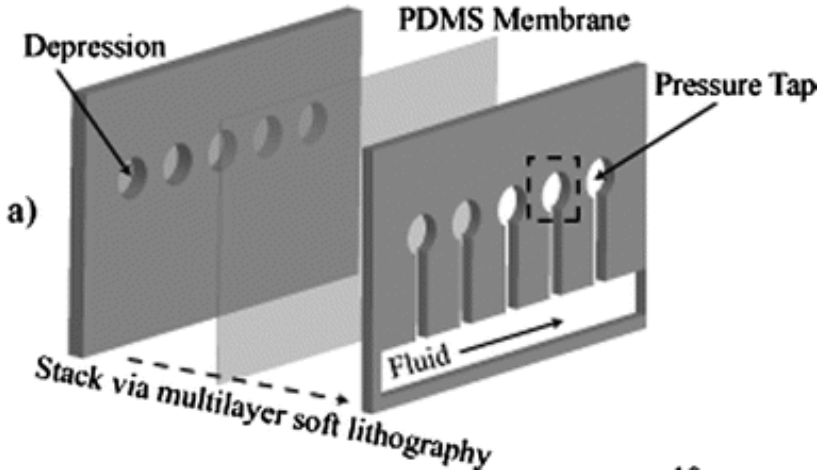

Figure 2.3. Schematic of a multilayer PDMS sensor with auxiliary channels connecting pressure taps and the main flow channel [18].

To our knowledge, a majority of previous designs only perform pressure measurement at one single point, or several scattered points, with a notable exception of the study by Orth et al

[18], who presented a 2D multiplex pressure sensor design within a Hele-Shaw cell fabricated from PDMS as shown in Figure 2.4. The design was created by placing the pressure taps that contains membrane sensor in a shape that looks like a slightly disoriented array of horseshoe as shown in Figure 2.4a. We note that although several other studies also reported designs for single-point pressure measurement, the basic ideas and principles are very similar to what has been reviewed and discussed previously.

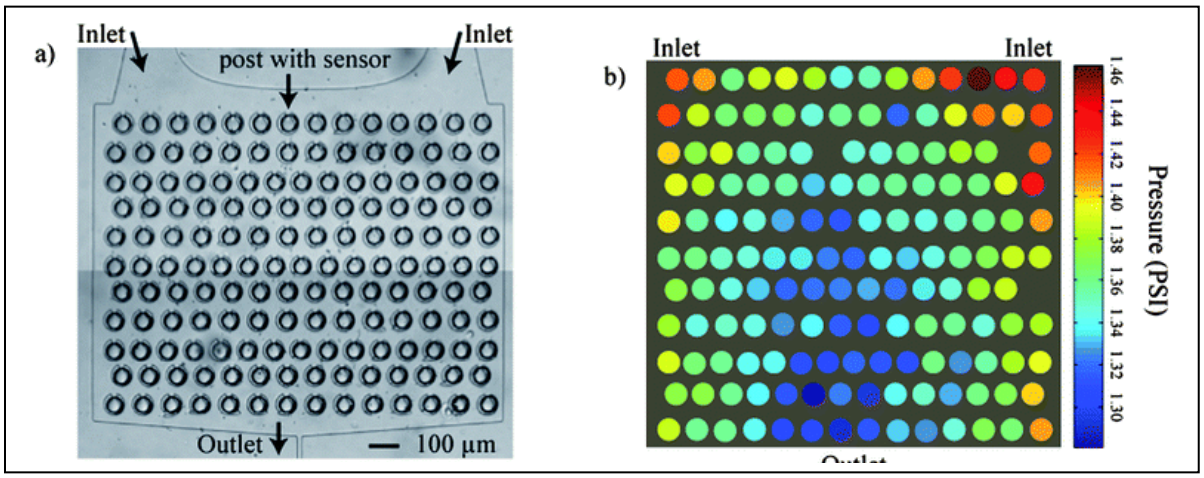

Figure 2.4. a) A 2-D multiplex design for fluid pressure measurement by Orth et al. b) Pressure map of a steady state fluid flow with red and blue colors indication high and pressure, respectively [18].

2.2 Quantification of membrane deflection

Methods for the quantification of membrane deflection can be in general classified into two categories: optical-based ones [14 - 15, 17 - 19] and electrical-based ones [20 - 22, 26 - 28]. Pressure sensors with electrical readouts analyze the change of voltage, current or resistivity caused by the deformed membrane, while pressure sensors with optical readout directly image the membranes to determine their deflections. For instance, methods based on principles of piezoelectricity, piezoresistivity, capacitance, and resonant frequency all fall in the electrical

readout category, whereas methods based on image intensity, fluorescent particles and interferometry all fall in the optical readout category.

Quantifying the membrane deflections with optical readout scheme often involves using a microscope and a camera to quantitatively measure the deflection of the PDMS membrane. Although they may require some sophisticated optics and image processing [24], they do not however require any supply of power or integration of complex circuits, and they are free of electromagnetic radiation, which sometimes could be a serious issue for many electrical devices [25]. In this category, the Mach-Zehnder (MZ) interferometer is a widely used approach where the pressure change led to a change in refractive index of the medium which resulted in phase change. The output from MZ interferometer is obtained by comparing the phase change between the optical mode in the measurement arm and the phase of the mode in the reference arm by an equally split optical beam. If the two modes are in phase, constructive interference occurs yielding a bright spot at the end of the waveguide as the intensity goes down the output waveguide. If, however, the two modes are out of phase by 180°, then it forms the destructive interference, leading zero intensity going away from the guide. An advantage of using MZ interferometer is that it can be made small as the overall size is determined by the measurement/reference arm which has the optical mode with few micrometers of diameter. Although the MZ interferometer-based sensor is easy to read out; determining the absolute value of maxima (or minima) is challenging [23].

Chung et al. quantified membrane deflection as a function of applied pressure by using fluorescent tracer particles and an image-based algorithm [20]. Again, the micromodel is made up of three PDMS layers: flow layer containing the flow channel, the sensing layer containing the detection channel which is filled with a fluorescent particles suspension and the membrane in

between the flow and sensing layer. When pressure is applied, the membrane deflects upwards and the fluorescence particles at the center of the sensing chamber become out of focus, creating an effectively particle-free region therein, as shown in Figure 2.5. A MATLAB algorithm was developed to identify the region with in-focus particles and the volume of membrane displacement was calculated, which was then correlated with the applied pressure. Major advantages of this method include high precision of pressure measurement in both direct and remote detection modes, easy integration into microdevices, the potential to achieve multiplex pressure measurements and the flexibility to finely tune the measurement range. Measurement ranges of 0 – 11.032 kPa and 11.032 – 68.948 kPa were achieved using a thin membrane and a relatively thick membrane, respectively.

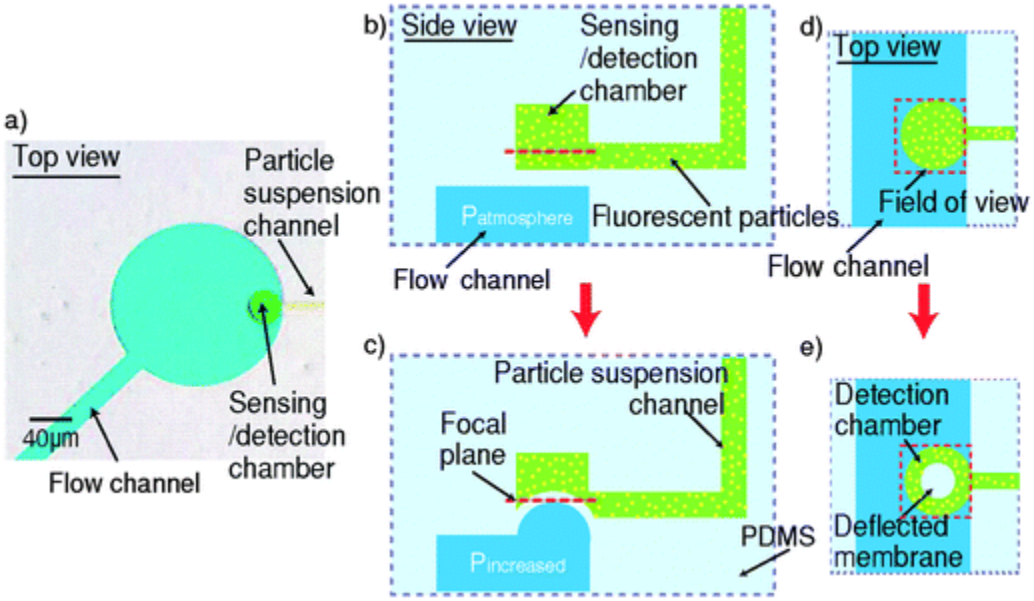

Figure 2.5. Illustration of the design by Chung et al.: a) top view of the microdevice with flow channel, sensing channel and particle suspension channel. b) and c) illustrate the behavior of sensing chamber when the pressure is at atmospheric pressure and increased respectively. d) and e) are the top views of the sensing chamber deflection from its initial position [20].

Song et al. used a monochromatic light source to get an interference pattern, which was then fed into a pattern recognizing algorithm to find the optical image contrast [19]. Again, a standard three-layer design was implemented and fabricated using PDMS. To quantify the membrane deflection, a monochromatic light is passed through the microdevice, which is reflected from the top and bottom boundaries of an air layer trapped in the sensing chamber. As shown in Figure 2.1, depending on the thickness of the air gap, the interference can be constructive or destructive, producing rings of light, which was used to infer the shape of the deflected membrane, and then correlated with the applied pressure. The working range of the device is from 0- 151.685 kPa with the sensitivity of 0.064 μm/kPa and the overall accuracy of ±1.4 % of full scale.

Another approach by Orth et al. [18] is based on the observation that the deflected membrane "operates as pneumatically-tunable microlenses whose focal length vary with pressure" as shown in Figure 2.3. To take the measurements, first the main microchannel was filled with water and connected to air on both inlet and outlet with a common air pressure source. As the pressure increases, the membrane is deflected into the corresponding sensing chambers, which serve as microlenses, and focus the light emitted from the white LED source. Then the images of transmitted light are processed in MATLAB to identify the positions of the focal spots which can be used to calculate the intensity. With this method, the average intensity *vs*. pressure relationship was determined. This device was then used in the study of pressure drop in chicken's RBC (Red Blood Cells) flow through a constriction. The device sensitivity decreased with increase in pressure with an accuracy of < 0.5% of full-scale value of 27.717 kPa. The stability of the pressure measurement with this device was found to be ± 0.138 kPa over a period of 20 minutes [18].

Alternatively, Chaudhury et al. [17] successfully quantified membrane deflection based on the contrast of an image. The three-layer design was again employed. In particular, the sensing membrane, which is a 10 µm thick semi-transparent PDMS layer, was dyed with food color for enhanced optical contrast and a 500 µm thick borosilicate glass substrate served as sealing and mechanical support for the sensor as shown in Figure 2.6a. The membrane deflection is measured using a z-scanning module as shown in Figure 2.6b. As the refractive index is significantly different from glass to air and air to PDMS, both the interfaces have higher image sharpness when focusing through the z-scanning module. Then the MATLAB algorithm was used to analyze the grayscale values to quantify the image contrast. The pressure obtained from the experiment, deviated with a maximum relative standard error of ~7% throughout its dynamic range of 0- 10 kPa when compared with a pressure transducer measurement. It is also worth noting that the membrane deflection is nonlinear when the applied pressure is below 0.2 kPa, and linear with decreasing sensitivity of ~ 60 µm/kPa when the pressure is above 0.2 kPa.

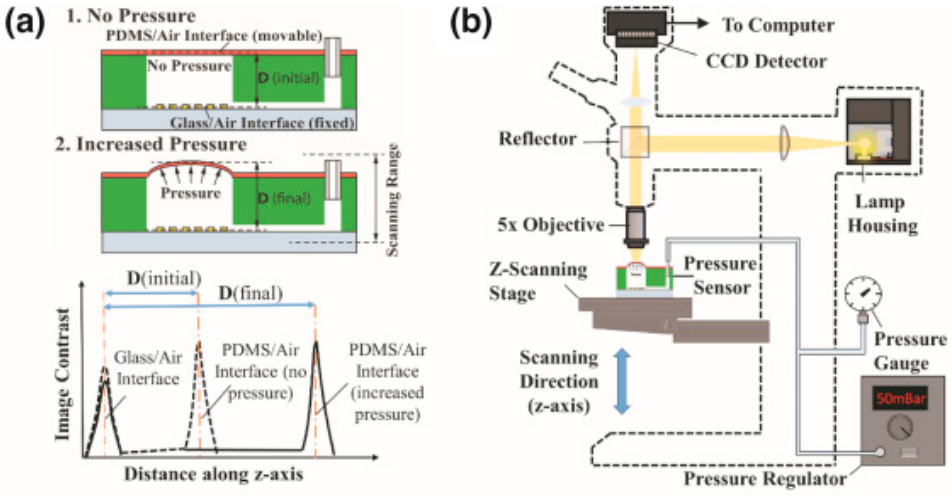

Figure 2.6. a) Working principle of the image contrast-based pressure sensor. b) The Z-scanning setup for measuring the distance between the glass-air and air-PDMS interfaces [17].

On the electrical readout side, one sensing principle relies on resonant sensors to convert the change of mechanical stress of a membrane into a change of resonance frequency of a vibrating system [26]. Here the frequency of the membrane is directly proportional to its deflection. Resonant sensors have excellent stability and can directly convert the output signal into digital signal. However, their complicated structures require complex fabrication procedures, and the need of vacuum sealing and mechanical coupling between the membrane and the resonator both contribute to their high costs.

Capacitive sensing converts applied pressure into an electrical signal with simple and low-power method. A capacitor is made up of a dielectric medium like air, sandwiched between two parallel conductor plates. In capacitive pressure sensors, the applied pressure deflects the membrane which leads to a change in the distance between the plates, which yields a correlation between the applied pressure and the capacitance change [22, 27]. Capacitive sensors usually have air as dielectric medium, silicon as one plate and a metal layer as the other plate. However, success has also been reported to use a ceramic slab as the dielectric medium, which is kept in between two mercury drops to form a capacitor [27]. On the one hand, the main advantages of capacitive sensing include high accuracy, low power consumption and small temperature dependence. On the other hand, designing and fabrication of such capacitors can be highly complex too.

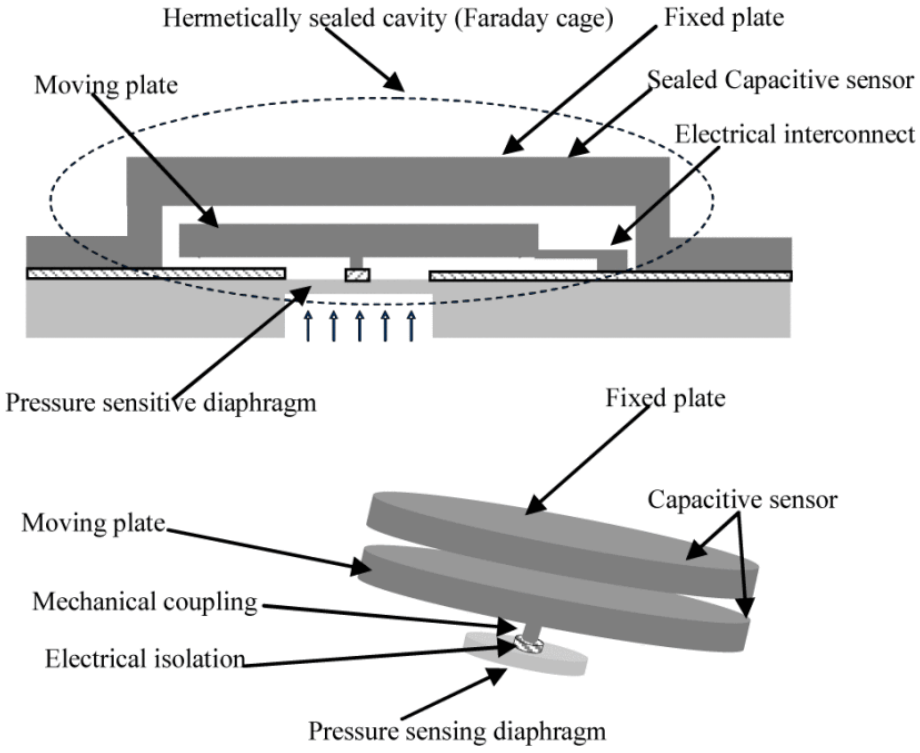

Figure 2.7. Schematic of an ultra-thin high sensitive capacitive pressure sensor which mechanically coupled with a pressure sensing diaphragm [28]

Compared with capacitive sensors, piezoresistive sensors are relatively easier to design and fabricate and are thus more widely used. Resistors are used as sensing elements here, which can be diffused in the membrane or deposited on top of the membrane with an isolation layer of SiO_2. Piezoresistors work by changing the resistance of the sensing layer when its physical dimension is changed by the applied pressure (stress) [21, 24, 27]. For thin diaphragms subject to small deflections, a linear relation can even be assumed between the resistance and the applied pressure [24]. Although the piezoresistive sensors are high linearity, easier to fabricate, and cost effective, they suffer from high temperature sensitivity which renders them not suitable for low pressure measurements.

For all of the above-mentioned electrical pressure sensors, basic principles are based on a diaphragm which deflects under applied pressure. It is worth noting that there is another electrical pressure sensor which employs a resistive liquid metal such as Galinstan as the sensing element [29]. Galinstan is a eutectic liquid alloy mixture of gallium, indium and tin that exists in liquid phase at room temperature. When the applied pressure is varied, the shape or dimension of the liquid metal changes accordingly, which in turn induces a change in its resistivity. This approach offers high linearity, long term stability and good reversibility.

2.3 Other Alternative Designs

In optical pressure sensors, low pressure sensitivity is a common problem. To overcome this problem, fiber Fabry-Perot sensors and Fiber Bragg grating sensors are introduced. Fiber Fabry-Perot sensors are structures that have flexible diaphragm attached to Fiber-Perot cavity which are connected to an optical fiber as shown in Figure 2.8. The applied pressure led to variation in length of the Fiber-Perot cavity, thus measured by Fiber-Perot white light interferometry [39].

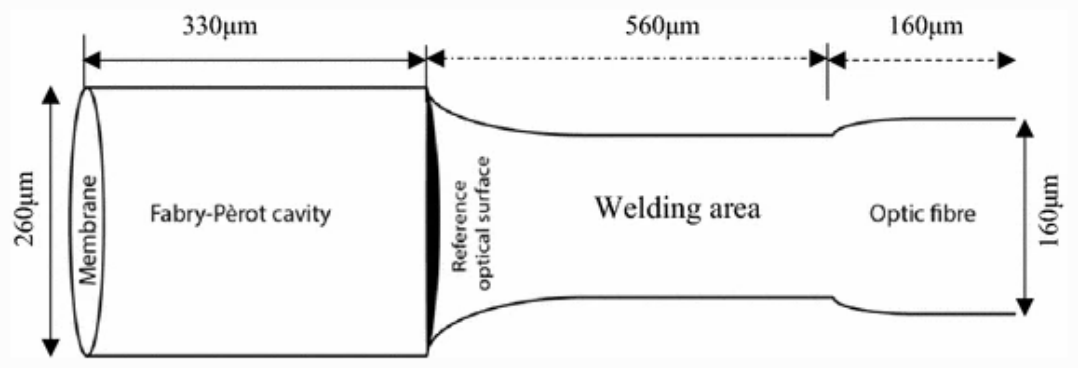

Figure 2.8. Schematic of Fiber-Perot sensor by Zariko et al. [39]

Fiber Bragg gratings are structures with a periodically varying refractive index that uses ultraviolet radiation to photo-write into the core of photosensitive optical fibers. The incident light,

of wavelength equal to the Bragg wavelength that satisfies the Bragg resonance condition, reflects the broadband light source, which illuminates the Fiber Bragg grating [30]. Effective refractive index and periodic spacing changes as the mechanical stress is applied. This working principle of Fiber Bragg grating is schematically illustrated in Figure 2.9.

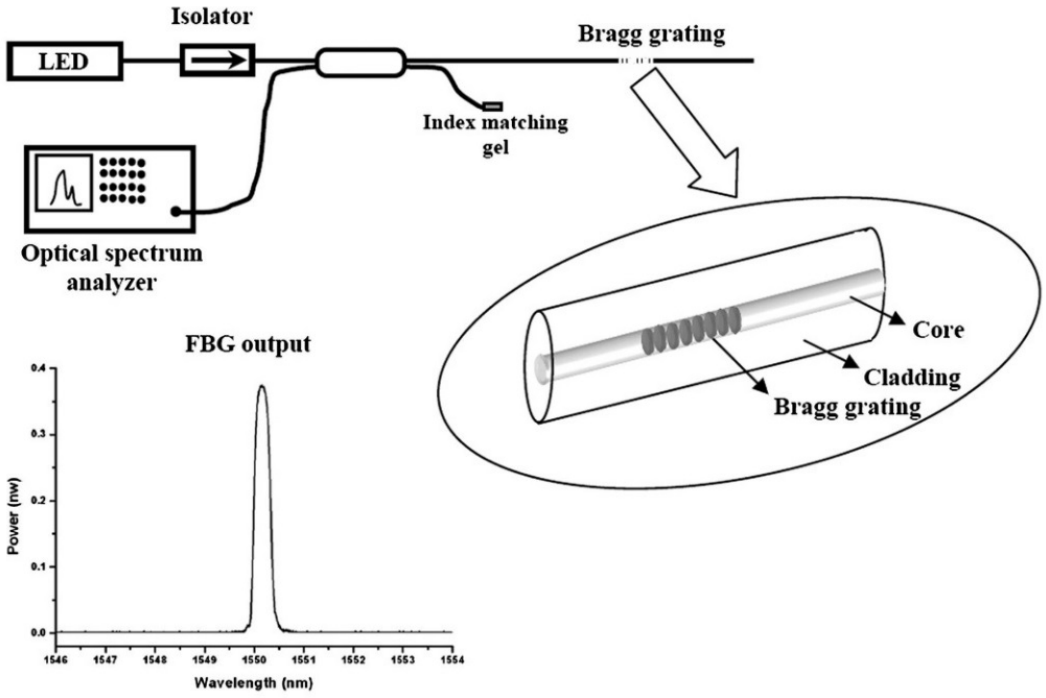

Figure 2.9. Principle of Fiber Bragg Grating sensor and output of Fiber Bragg Grating [30].

The working principle of the extrinsic fiber Fabry-Perot interferometer (EFPI) is based on the multi-beam interference between two partial mirrors as shown in Figure 2.10. Two beams of light are reflected with one from Single Mode Fiber 1 (SMF1) and the other one transmitted through the air gap between SMF1 and SMF2, reflected from SMF2, and recoupled with SMF1 after passing through the air gap. By varying the air gap size, the relative phase between two reflected beams is changed, which leads to various interference patterns. The pressure applied on the mechanical transducer which incorporates the EFPI can be simply obtained by monitoring the

interference patterns. Weak temperature dependence and simple readout are among the advantages of this sensor. However, its disadvantages include complicated fabrication processes and optical alignment procedures [30]. It is worth noting however, that it is usually hard to integrate the aforementioned Fabry-Perot sensors and EFPIs directly into microfluidic devices because of their relatively large sizes and the multistep fabrication processes required to fabricate a microfluidic device.

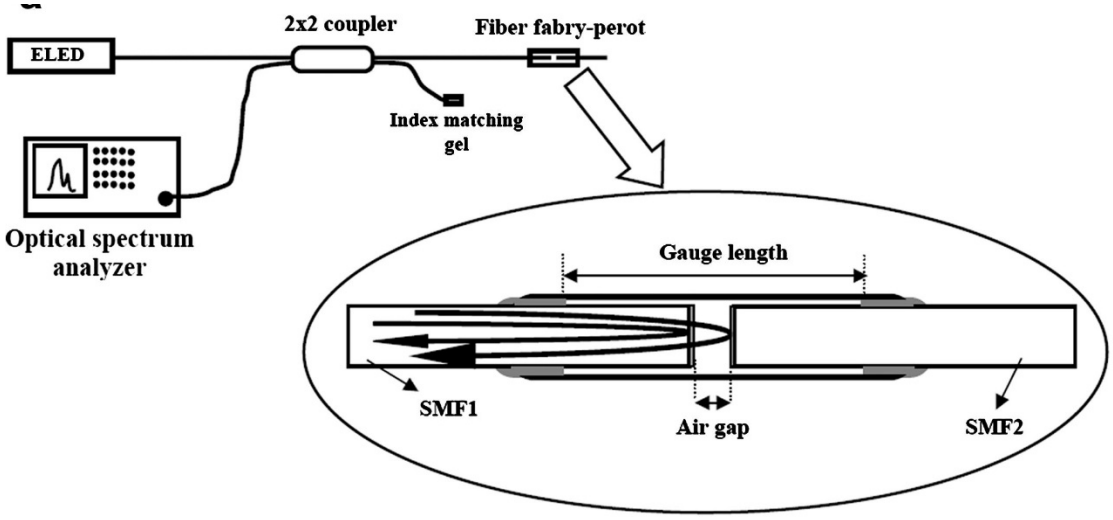

Figure 2.10. Working principle of EFPI [30]

Taken together, despite the extensive development of various pressure sensors, our literature review indicates that: 1) a majority of designs essentially only perform single-point measurements as opposed to a pressure field measurement; 2) many previous multiplex designs mostly have a low number of measurement locations and thus low spatial resolution; 3) most previous designs require auxiliary channels for signal readout, which can reduce the device responsiveness as well as complicate the fabrication process. Therefore, new designs are needed not only to address our specific need, but also to satisfy the needs in a much broader range of

applications by offering simpler fabrication, easier implementation, better versatility, and higher accuracy.

CHAPTER 3

EXPERIMENTAL DESCRIPTION

3.1 Pressure Sensor Design

3.1.1 The Three-layer Design

Like many previous designs for membrane-based pressure sensors, our design also consists of three layers: a microchannel layer, a thin membrane layer, and a supporting layer with microchambers called pressure taps as shown in Figure 3.1. The microchannel is the measurement target of the sensor, and essentially where the flow of interest occurs. It has an inlet and an outlet connected to a test section with specifically designed structures (*e.g.*, a microchannel or porous structures), through which fluid flows. The thin membrane layer, typically a few micrometers thick sandwiched between the microchannel layer and the supporting layer, serves as the sensing element of the device. The supporting layer containing pressure taps at desired locations provides structural support to the thin membrane so that the membrane is suspended only at locations where there are pressure taps below it. As demonstrated in Sec. 3.2.3, the supporting layer not only provides structural support to the membrane, but also allows us to finely tune the sensitivity of the sensor by simply varying the size of the pressure taps. These pressure taps are connected to each other and opened to atmosphere through a narrow channel allowing them to stay constantly at atmospheric pressure during experiments [18].

Notably, what is novel to this design is that fluorescent particles of 1 μm in diameter are embedded into the sensing membrane. As the pressure in the target channel changes, the membrane deflects accordingly, carrying the embedded particles to a different z location, which can then be

accurately measured employing the Astigmatic Particle Tracking technique as described in Sec. 3.1.3. This design offers a few benefits: (*i*) it is possible to probe the pressure at virtually any location of the target channel by carefully patterning the pressure taps, and even 2D pressure fields can be achieved by incorporating a matrix of pressure taps; (*ii*) through the implementation of particle-embedded membrane, pressure measurement is transformed to the quantification of particle locations, which is much easier to achieve experimentally; (*iii*) the sensor sensitivity and measurement range can be finely tuned by varying the pressure tap size or membrane thickness.

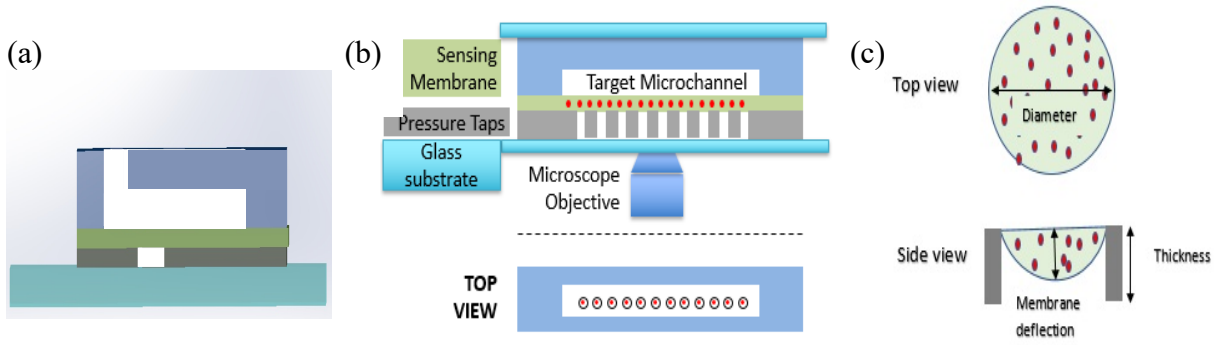

Figure 3.1: (a) A schematic diagram illustrating the three-layer design of our pressure sensor with pressure taps within the supporting layer, the thin membrane and the microchannel layer shown from left to right; (b) the side view and top view of the three layer design and (c) the top view and side view of a pressure tap with a deformed membrane.

3.1.2 Mechanics of Thin PDMS Membrane

As mentioned previously, the sensing of pressure change relies on the deflection of the thin membrane suspending above the circular pressure tap as shown in Figure 3.1c. Theoretically, the deflection of the membrane for a clamped circular thin plate with a radius of *a* subject to a uniform pressure *P* is given by the following equation:

$$w(r) = \frac{Pa^4}{64D}\left[1 - \left(\frac{r}{a}\right)^2\right]^2 \qquad (1)$$

where r is the radial coordinate and D is the flexural rigidity, which in turn is defined as,

$$D = \frac{Et^3}{12(1-v^2)} \tag{2}$$

Here, t is the thickness of the membrane, and E and v are the Young's modulus and the Poisson ratio of the membrane, respectively [24]. Equation (1) suggests that the center deflection of a circular shape membrane is proportional to the 4th power of its radius and inversely proportional to the 3rd power of its thickness.

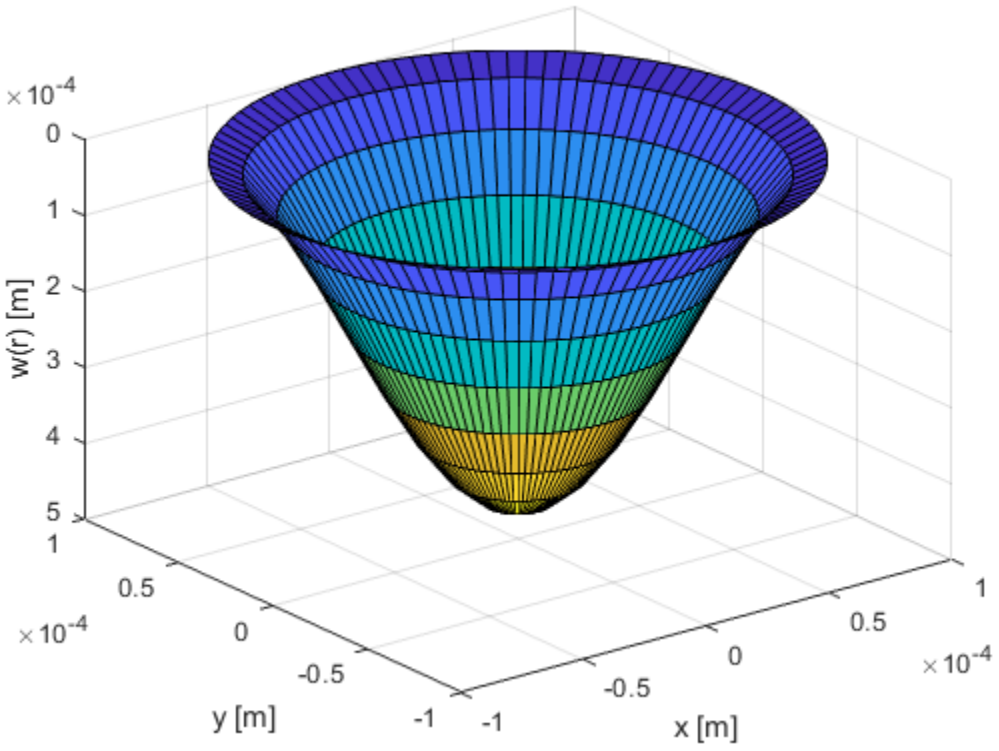

Figure 3.2. Example of a 3-D plot of the clamped circular membrane deflection ($w(r)$) for an applied pressure (P) of 1 kPa, with 100 µm membrane radius (a) and 5 µm membrane thickness (t) in cartesian plane.

3.1.3 Astigmatic Particle Tracking

In our experiments, the membrane deflection is measured using the Astigmatic Particle Tracking technique. This technique is built upon standard microscopy with a modification such that a cylindrical lens is placed between the microscope objective and the camera. With this cylindrical lens, particles at different depths (*i.e.*, *z* locations) display different shapes varying from vertical elongation to horizontal elongation, so that the *z* location of a particle can be simply inferred from its shape in the *x*-*y* plane. When the particle is far away from the objective (*i.e.*, higher z location) particles are vertically elongated as illustrated by particle A shown in Figure 3.4. Similarly, when a particle moves towards the objective, it shape gradually changes towards a horizontal elongation as illustrated by particle B shown in Figure 3.4.

As shown in Figure 3.3 the cylindrical lens is attached to the microscope adaptor that is right in front of the camera using double-sided tapes. The aligned cylindrical lens provides no curvature in *x*-direction and maximum curvature in *y*-direction. Rays passing through *x*-*z* plane will have the same focal plane and magnification *M* while the rays passing through *y*-*z* plane will have a different focal plane and magnification M_y. Particles will be seen as elongated in either *x*- or *y*-direction depending on the relative location to the original focal plane [31]. When this technique is applied to image a particle embedded in the membrane, the *z* location of the particle is measured based on the shape of its image, which in turn provides a quantification of the membrane deflection, given that there is no relative movement between the particle and the membrane.

Figure 3.3. The cylindrical lens attached to the microscope adaptor.

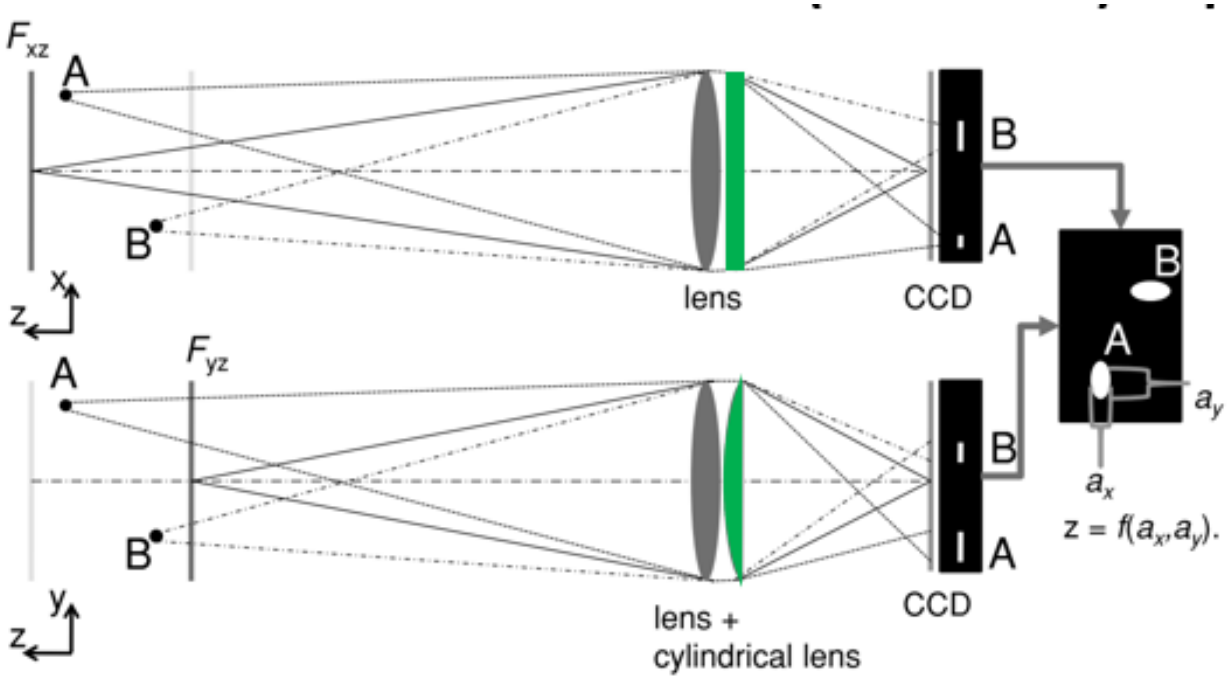

Figure 3.4. The schematic representation of image astigmatism [32].

3.2 Fabrication

3.2.1 Microchannel Fabrication

The microchannel fabrication is conducted employing standard soft lithography, which consists of three major steps: (*i*) photo mask design, (*ii*) master fabrication and (*iii*) Polydimethylsiloxane (PDMS) molding. Below each step is described in detail.

(*i*) Photo mask design

The photo mask of the microchannel layer was designed in Adobe Illustrator. Each mask consists of four individual microchannels, of which three are 300 μm wide, one is 500 μm wide with all have 100 μm narrow channel in the middle as illustrated in Figure 3.5 Each microchannel consists of an inlet, an outlet and a 100 μm test section with length of 1.96 cm in the middle as shown in Figure 3.6 to study the pressure difference between upstream and downstream of the flow.

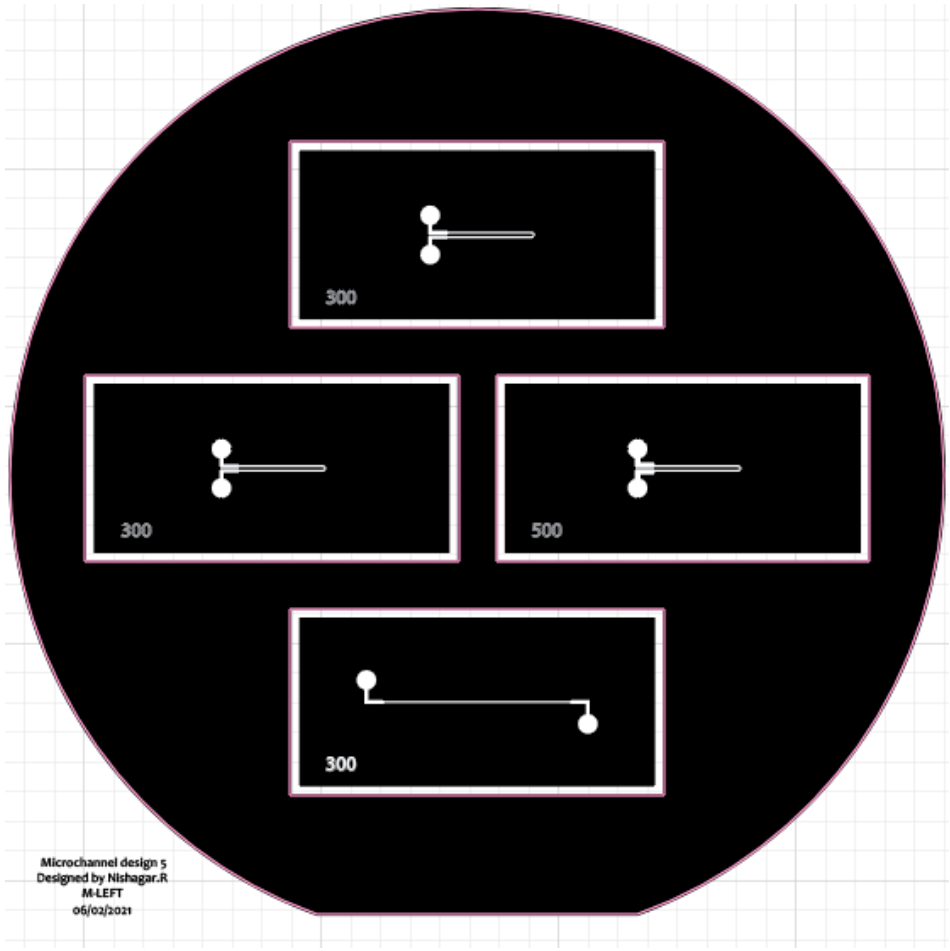

Figure 3.5 The microchannel photomask consisting of four individual microchannels, of which three are 300 μm wide, one is 500 μm wide each with a 100 μm wide microchannel in the middle.

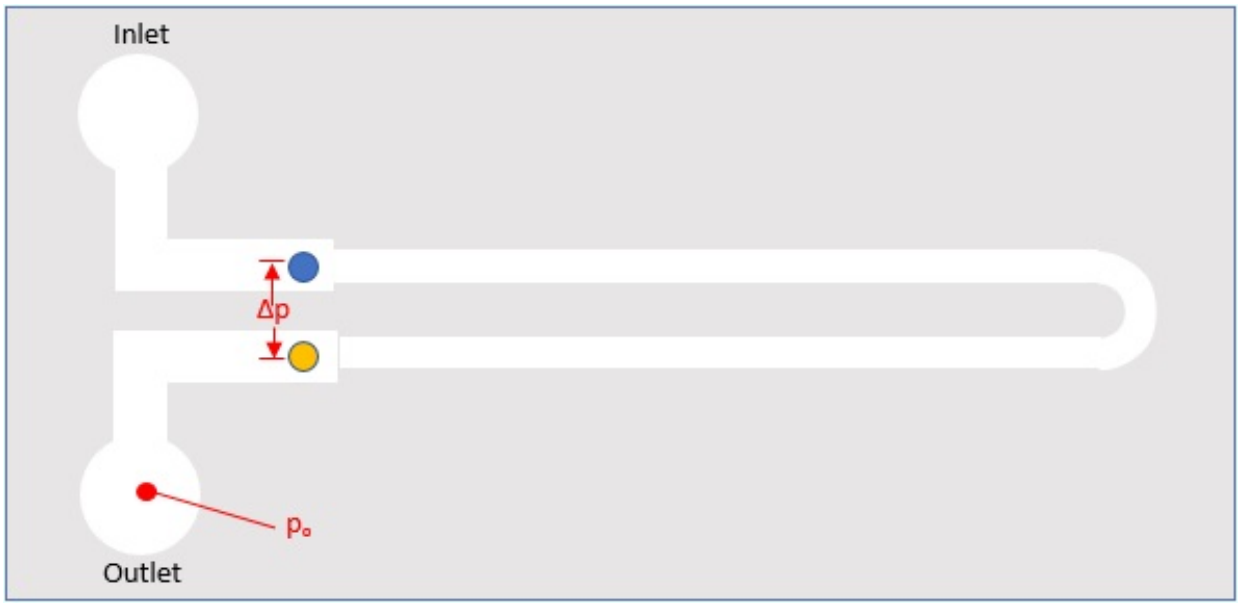

Figure 3.6. Schematic diagram of a micromodel with microchannel and pressure taps (in colored circles) overlaid in the same plane for illustrative purpose. The narrow microchannel (L = 1.96 cm, h =122.7 µm, w =119.5 µm), within which the viscous pressure drop was measured to test the feasibility and sensitivity of the pressure sensors.

(*ii*) Master Fabrication

The master fabrication was performed in the Montana Micro Fabrication Facility at Montana State University-Bozeman. As illustrated in Figure 3.7, to start the process, a new clean single-side polished (SSP) silicon wafer was placed on the hot plate (Electronic Micro System 1000-1) at 95°C for 5 minutes to dehydrate. The silicon wafer was then centered on a spin coater (Laurell WS-650MZ-23NPPB) and locked by applying partial vacuum underneath it. About 20 ml SU-8 3050 (Kayaku SU-8 3050) photoresist was poured on top of the silicon wafer so that roughly three quarters of the wafer surface was covered. The Laurell spin coater was set to spin at 500 rpm for 10 seconds and at 1000 rpm for 30 seconds as instructed by the manufacturer in order to achieve a nominal final film thickness of 100 µm. After spin coating, the wafer was soft baked for 45 minutes on the hot plate at 95°C. The soft baked silicon wafer was then placed on a contact aligner

stage (ABM-USA, Inc ABM/6/350/NUV/DCCD/M) to be exposed under the G-line UV light for 20 seconds at an intensity of 15 mW/cm^2.

It is worth noting that the photo masks used in the fabrication are made of plastic films, which are susceptible to bending and deformation. Extra care was therefore used to ensure successful exposure using the AB-M contact aligner as shown in Figure 3.8. First a flat glass plate of 4 × 4 inches was placed on the AB-M Contact aligner stage and locked in place with vacuum, on top of which the silicon wafer is placed. The photo mask was then placed on top of the silicon wafer and manually aligned by using the edges of the photo mask and the silicon wafer as references. To ensure proper contact between the SU-8 photoresist coated on the silicon wafer and the photo mask, another glass plate was placed over the mask to serve as an additional weight. Following UV exposure, the silicon wafer was taken to the hot plate to post-bake for 5 minutes at 95°C and then set on a flat surface for about 1 minute to allow it to cool down. Then the silicon wafer was transferred into a crystallizing dish containing SU-8 developer of 0.5 inch in depth. The crystallizing dish was kept on the orbital shaker which ran at a speed of 40 rpm for 30 minutes to develop the pattern. After development, the silicon wafer was rinsed with isopropanol, SU-8 developer and isopropanol, sequentially to remove residuals of the photoresist. Finally, the wafer was inspected under the microscope to ensure proper development of the SU-8 patterns. When necessary, the wafer would be further developed by repeating the last two steps until good patterns were achieved.

Figure 3.7. Steps to fabricate the master using SU-8 on a silicon wafer.

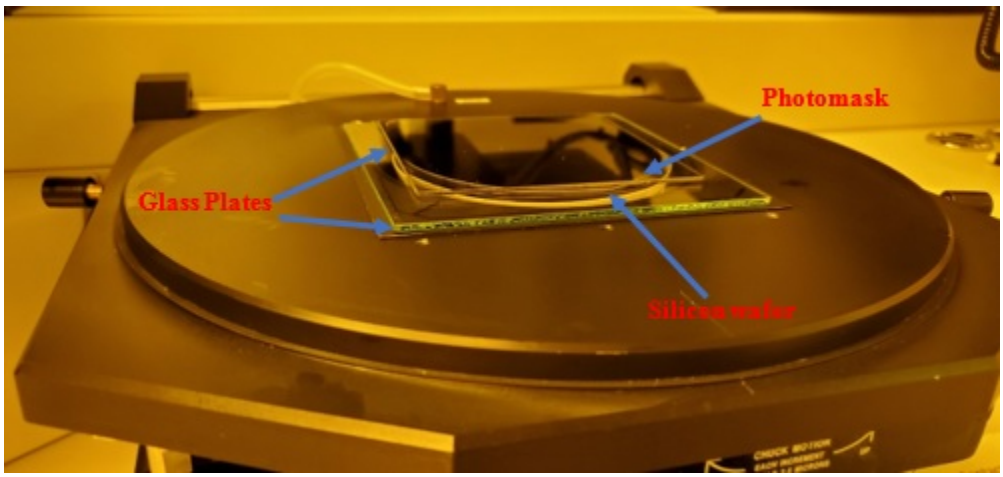

Figure 3.8. Setup for the UV exposure step with a coated wafer sitting in the middle of the stage.

(*iii*) PDMS molding

The Polydimethylsiloxane (PDMS) molding was done in the Microfluidics Lab for Energy and Fluid Transport (M-LEFT) at Montana State University- Bozeman. The molding process started with a silanization step, where a vapor layer of Trichlorosilane (Sigma-Aldrich 1H,1H,2H,2H-perfluorooctyl) was applied on top of the silicon wafer with microchannel design to facilitate the peeling off process of the PDMS layer from the silicon wafer in a later step.

To perform the silanization process, a container that is made of a PVC pipe segment was first prepared as shown in Figure 3.9. A piece of plastic film tape is securely mounted to the pipe segment to serve as the bottom of the container. Once the container is ready, the silicon wafer (|*i.e.,* the master) was placed to the center of the PVC container, with the back of the wafer sticking to

the plastic film tape. The sealing between the bottom of the silicon wafer and the film tape was to ensure that the PDMS solution, which would be added into the container during the following step, would spread evenly across the top of the silicon wafer without going underneath it. The whole assembly was then transferred into the vacuum desiccator to be ready to get silanized. A glass petri dish was then placed to the side of the silicon wafer assembly within the same vacuum desiccator and about 20 µl of Trichlorosilane was transferred into the glass petri dish using a pipette (Biohit m20). Finally, the desiccator was vacuumed for 10 minutes using a vacuum pump (Rocker 410), following which the vacuum pump was turned off and the desiccator was allowed to sit under vacuum for 30 minutes.

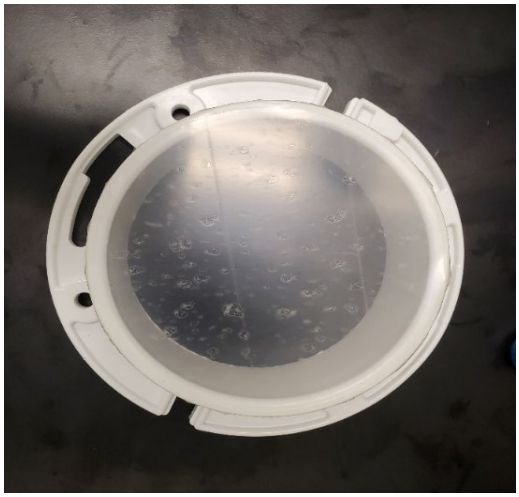

Figure 3.9. Cylindrical PVC container covered with plastic film tape.

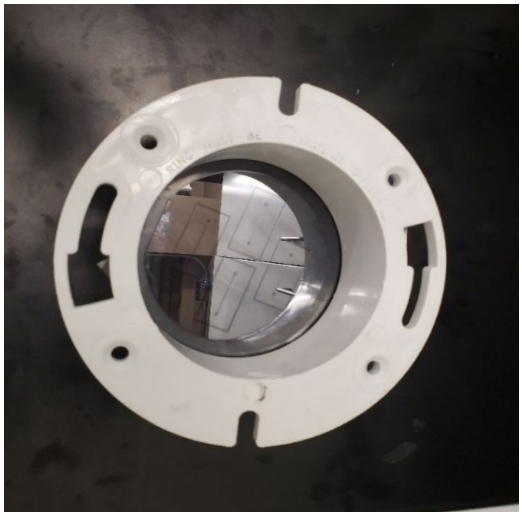

Figure 3.10. Silicon wafer placed in the center of the cylindrical PVC container.

In the meantime, PDMS solution was prepared from the two-part Sylgard 184 PDMS polymer kit. 100g of part A (pre-polymer) and 10g of part B (cross-linker) (*i.e.*, a weight ratio of 10:1) are weighed using a scientific balance (Denver Instrument 0000753786) and mixed well in a plastic cup. The mixed PDMS solution was then degassed to remove the air bubbles that are trapped in the polymer mixture when the PDMS solution was vigorously mixed in the previous step. This was done by placing the plastic cup containing PDMS solution to another vacuum desiccator that was connected to the same vacuum pump until all visible air bubbles came out resulting in a clear PDMS solution.

The clear PDMS solution was then carefully poured onto the silanized silicon wafer within the cylindrical PVC container. Air bubbles typically formed again in the poured PDMS solution due to the height difference between silicon wafer and the pouring cup. As such, the whole assembly was put back under vacuum for 15 min to further remove the air.

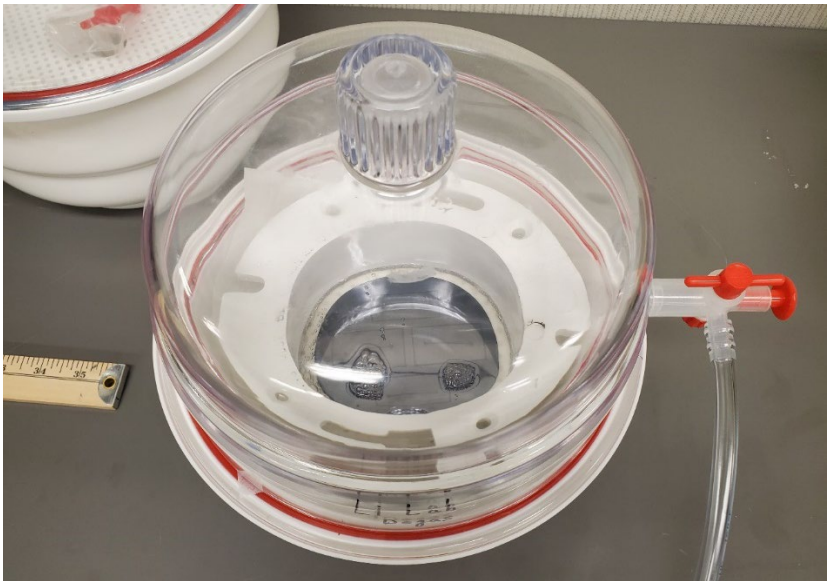

Figure 3.11. The PVC container being degassed in the vacuum desiccator to remove the air bubbles in the PDMS solution.

Following the degassing step, the cylindrical PVC container with the silicon wafer and PDMS solution was placed into an oven (Gravity Convection Oven, 414005-108) at 65°C and baked for 2 hours until the PDMS polymer fully cured. Once the PDMS fully cured, the plastic tape securing the bottom of the cylindrical PVC container was carefully removed by pulling the edge of it in a tangential direction. The cured PDMS slab was cut along the edge of the cylindrical PVC container and separated together with the silicon wafer from the container. Then the PDMS slab was carefully peeled off from the silicon wafer and cut into individual micromodels using a craft knife along defined lines on a clean cutting mat as shown in Figure 3.12 below.

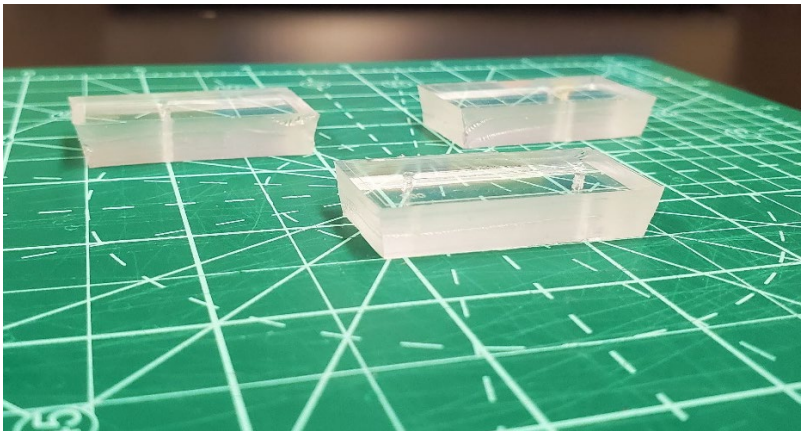

Figure 3.12. Individual microchannels cut out from the cured PDMS slab.

As the final step of the microchannel fabrication, two 2 mm holes were punched in each microchannel device using a coring tool (Miltex Biopsy Punch with Plunger, 2.0 mm) to serve as the inlet and outlet. The complete microchannels were then stored in a clean petri dish and ready for future use. It is worth noting that a good rule of thumb for creating straight holes in PDMS is to keep the PDMS microchannel at eye level and rotate the biopsy punch, and at any moment the punch should stay straight freely. The whole process is illustrated as a flow diagram in the Figure 3.13 below.

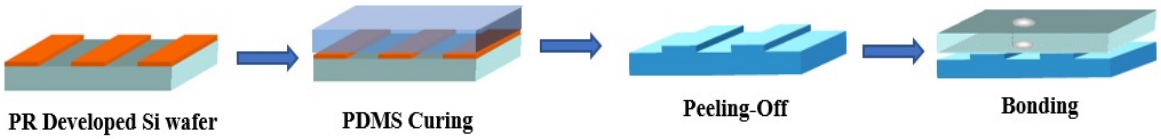

Figure 3.13. Steps for PDMS molding based on the SU-8 maser.

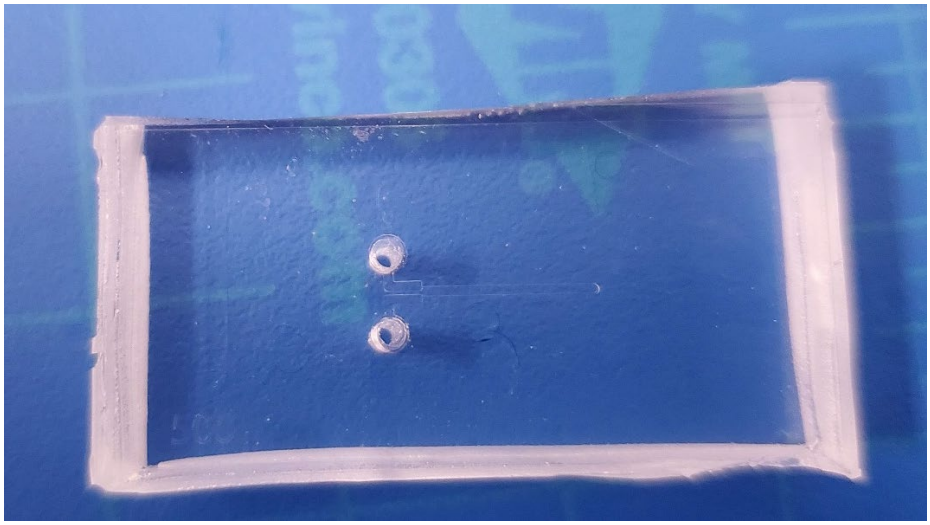

Figure 3.14. A complete microchannel fabricated from PDMS with inlet and outlet ports punched.

3.2.2 Particle Embedded Membrane Fabrication

The membrane fabrication was performed again in the M-LEFT at Montana State University- Bozeman, employing the spin-coating technique as shown in Figure 3.15. As mentioned previously, the goal herein is to create a flexible PDMS membrane of approximately 5 μm in thickness with 1 μm fluorescent particle embedded.

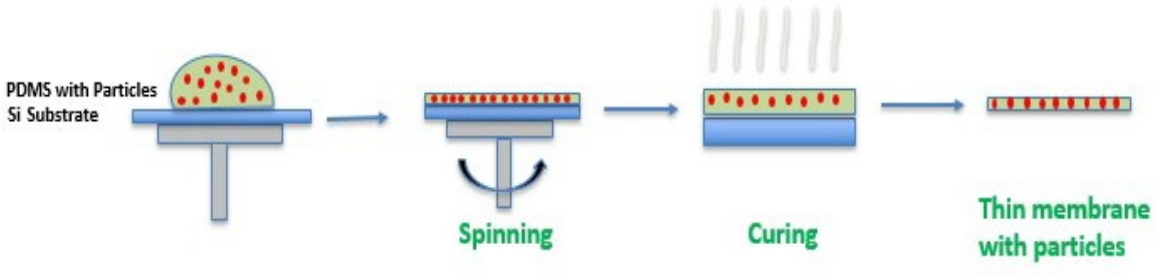

Figure 3.15. Flow diagram illustrating the spin coating procedure.

To start the process, a clean silicon wafer was first silanized in a similar way to that discussed previously. The only difference is that the wafer was directly placed into the vacuum

desiccator without using the PVC container. Following the silanization process, a diluted version of the PDMS solution is prepared. Instead of 30 minutes, silanization was done for 60 minutes for the membrane attachment to the silicon wafer. The two parts of Sylgard 184 PDMS polymer kit was mixed at a ratio of 12g of part A and 1.2g of part B (*i.e.*, 10:1 ratio of pre-polymer to cross-linker by weight) in a plastic cup and degassed in the degassing desiccator for 15 min. The degassed mixture was then diluted by tert-Butyl alcohol (TBA) at a ratio of 1:3 by weight. TBA is a tertiary alcohol with a formula of $(CH_3)_3COH$ and can be used to reduce the viscosity of the PDMS mixture without causing swelling to the final cured product, which is critical to create thin PDMS films as needed here [33]. It is worth noting that TBA is in solid state at room temperature due to its relatively high melting point (T_m = 25°C), so it was first melted by placing the bottle in a hot water bath (~28C) for 30 min. After TBA was added, the PDMS solution was well mixed, and 8 ml of the diluted solution is transferred into a vial using a pipette. Then 20 µl carboxylate-modified fluorescent particles of 1 µm in diameter (FluroSpheres, F8819) is added into the 8 ml solution again using a pipette. Afterwards the bottle was sealed with parafilm and placed in the ultrasonic bath for 6 minutes in order to distribute the fluorescent particles evenly throughout the PDMS solution.

The silanized wafer was then mounted onto the center of spin coater (Chemat Technology KW-4A) and locked by applying partial vacuum underneath it. Then the PDMS solution seeded with fluorescent particles was poured on top of the silicon wafer ensuring even and full coverage of the wafer. The spin coater was set to spin at 1000 rpm for 15 seconds and 2000 rpm for 5 minutes to achieve a final coating thickness of ~5 µm thickness according to the literature data [33].

Figure 3.16. The Chemat Technology spin coater used to spin coat the PDMS membrane

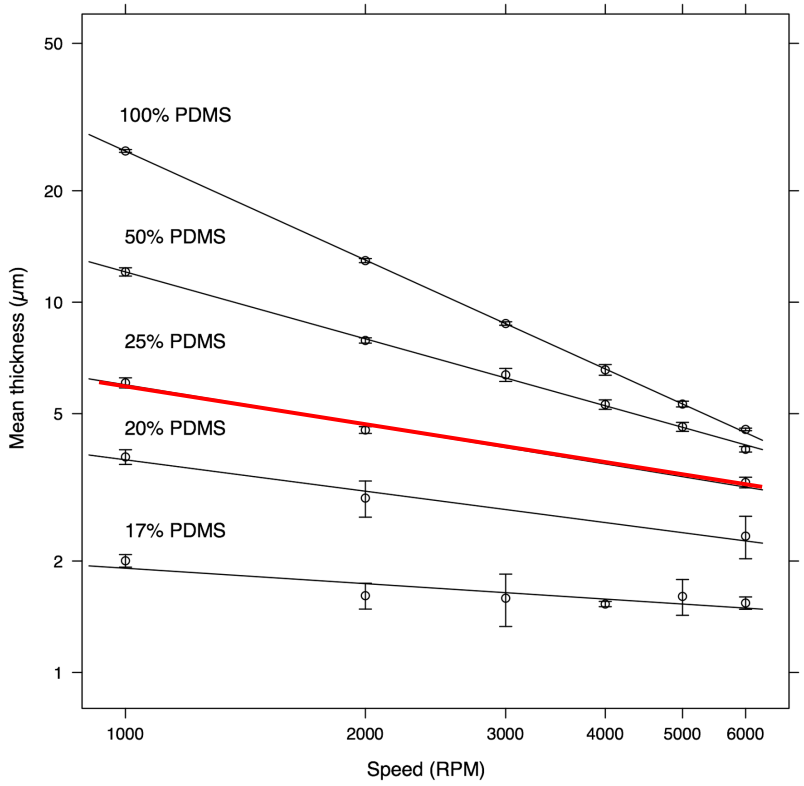

Figure 3.17. Coating thickness (μm) as a function of spinning speed (RPM) (reproduced based on the data by Koschwanez et al. [33]). The red line is the closest approximation to our membrane mixture.

As the final step, the coated membrane was semi-cured by baking it in the oven for 8 minutes at 65 °C. The semi-cure process was to ensure that the PDMS membrane was partially cured yet still sticky enough to enable good bonding between it and the microchannel. Then the microchannels that were fabricated previously were bonded to the membrane by slowly and steadily placing them onto the membrane. The membrane together with the attached microchannels was fully cured in the oven for another 2 hours at 65 °C.

3.2.3 Pressure Taps Fabrication

The pressure tap layer was fabricated in a very similar way as the microchannel layer, so only the difference in the procedures is emphasized here. This particular fabrication process again consists of the three steps as discussed previously (photomask design, master fabrication, and PDMS molding) and an extra step of optical glue molding.

The photomask design of the pressure taps is shown below in Figure 3.18. This mask also has four individual designs, with three containing pressure taps of 200 μm, and one containing 300 μm in diameter. Each of the pressure taps is connected to each other and opens to the atmosphere through another narrow channel in both directions as illustrated in Figure 3.18c. With this photomask, the masters of the pressure taps were fabricated again using the soft lithography process to achieve a thickness of 50 μm. The spin speed was set to 500 rpm for 10 seconds and 3000 rpm for 30 seconds using the spin coater. The silicon wafer with the 50 μm SU-8 master was soft baked for 15 minutes and exposed for 20 seconds at 15 mW/cm^2. Then the wafer was post baked for 5 minutes at 95 ºC and then developed with the developing time set to 15 minutes, as instructed by the manufacturer. Again, following the development step, the silicon wafers were rinsed with isopropanol, SU-8 developer and isopropanol sequentially to remove residuals of the

photoresist. Finally, the wafer was inspected under the microscope to ensure proper development of the SU-8 patterns. When necessary, the wafer would be further developed by repeating the last two steps until good patterns are achieved.

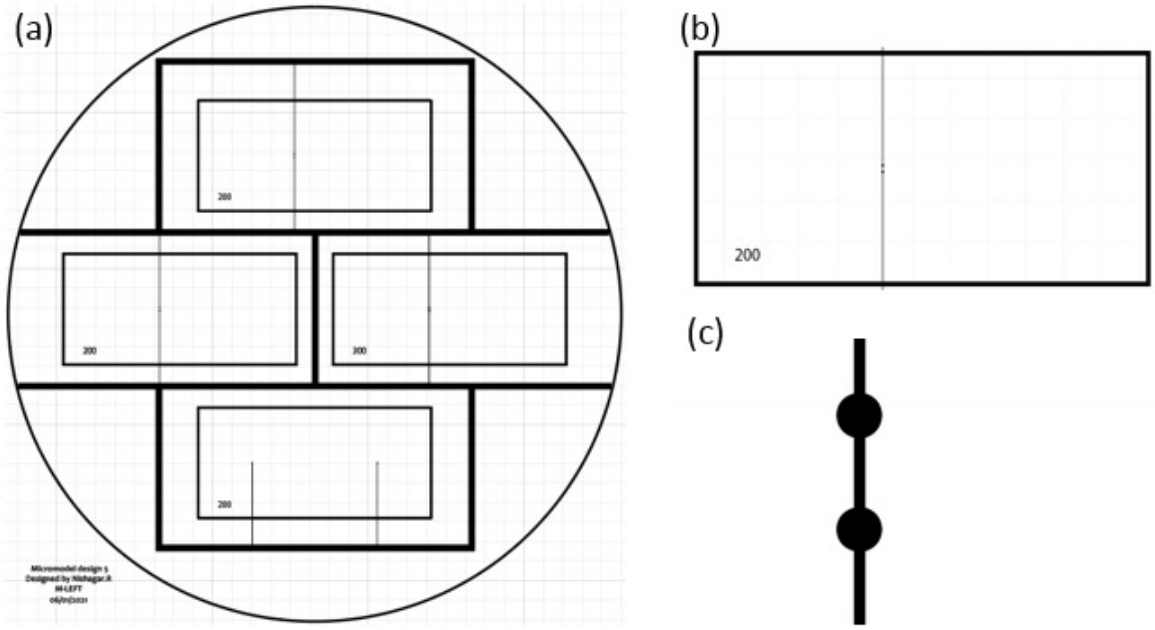

Figure 3.18. (a) The photomask design of pressure taps for four devices. Three of the four devices have pressure taps of 200 µm in diameter and one has pressure taps of 300 µm in diameter. (b) design of one tile with pressure taps of 200 µm in diameter and (c) a zoomed-in view of the 200 µm diameter pressure taps.

Based on the SU-8 masters fabricated in the previous step, a PDMS mold was created following exactly the steps as describe in the PDMS molding part in Sec. 3.2.1. As an extra step for the pressure tap fabrication, an optical glue molding was carried out based on the PDMS mold. For this fabrication, the PDMS mold was placed on a flat surface with the patterned side facing up and two drops of optical glue (Norland Optical Adhesive 81) are dripped onto the PDMS surface. Then a clean microscope slide (Fisher Scientific 75X25mm 144/GR) was placed on top of the

optical glue and gently pressed to ensure the glue evenly spreads between the PDMS mold and the microscope slide. The whole assembly was then exposed under UV light (Thorlabs M385LP1) for 10 minutes as illustrated in Figure 3.19. Once the glue was cured, the PDMS mold was peeled off carefully to produce pressure taps made of cured optical glue.

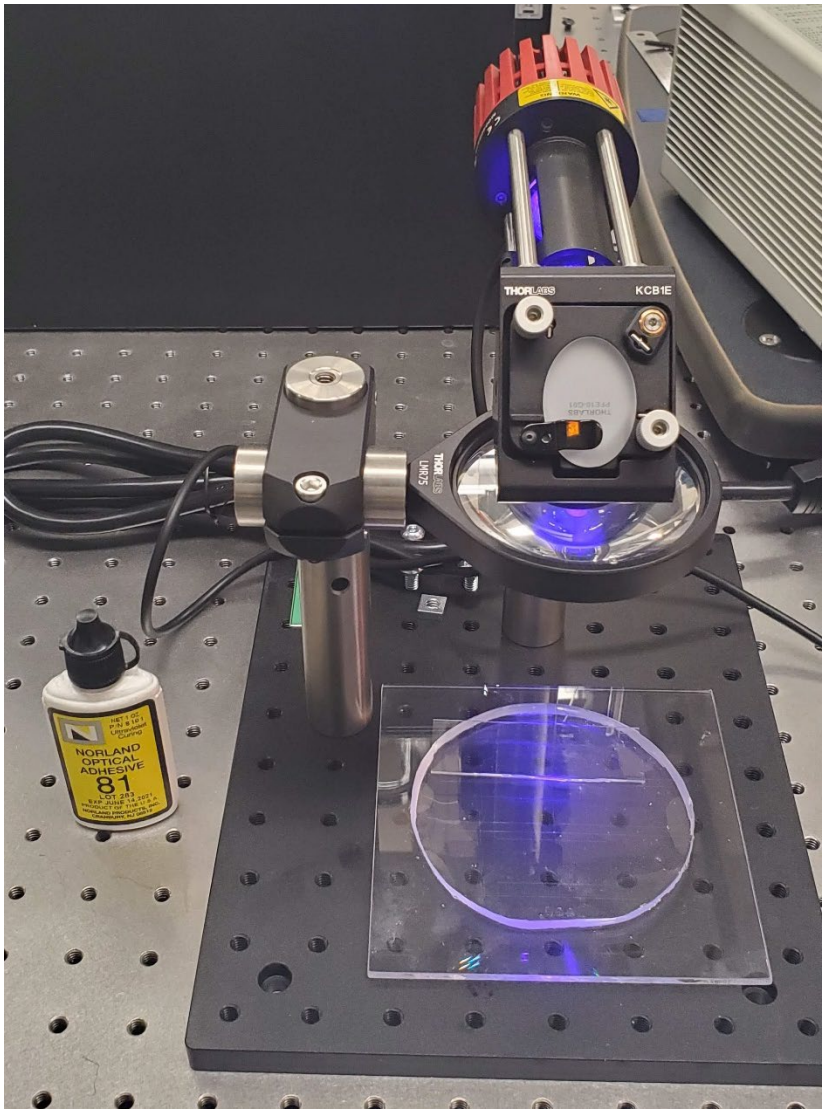

Figure 3.19. Setup for the fabrication of pressure taps using Norland Optical Adhesive 81.

3.2.4 Assembling the micromodel

Finally, the microchannels with the PDMS membrane were aligned carefully with the optical glue pressure taps using a customized aligning system as illustrated in Figure 3.20. After alignment, the microchannel with the PDMS membrane was simply pressed against the microscope glass slide with the pressure taps. The bonded micromodel was then ready to attach the nanoports to the inlet and outlet of the microchannel.

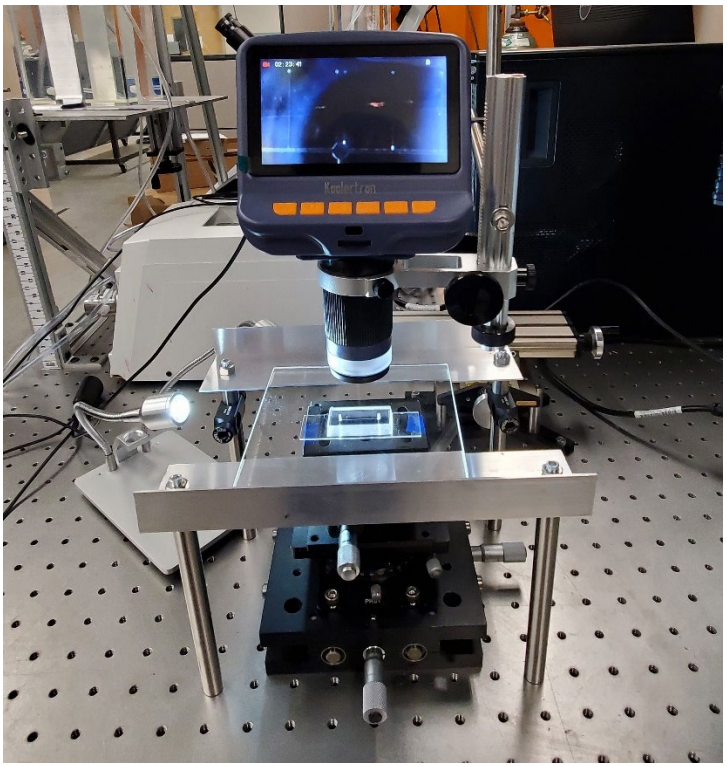

Figure 3.20. Three-axis aligning system used to bond the microchannel with membrane to the glass substrate with pressure taps. The three-axis stage on the bottom is used to finely adjust the relative position of the pressure tap and microchannel layers, and the USB optical microscope on the top is used to guide this alignment process.

A clean microscope slide (Fisher Scientific 75X25mm 144/GR) was used with two 1.5 mm holes drilled with a milling machine (Proxxon, MF 70) at same locations as the inlet and outlet of

the microchannel. Then two nanoports were carefully glued on top of the holes with epoxy glue and ~ 4cm of tubing (1/8 in diameter) was connected to the nanoports. Then the microscope slide was attached to the PDMS micromodel. This extra step was developed to avoid damage of the membrane or deformation off the PDMS structures when the nanoports were directly inserted into the punched holes. The final complete micromodel is shown in Figure 3.21 below.

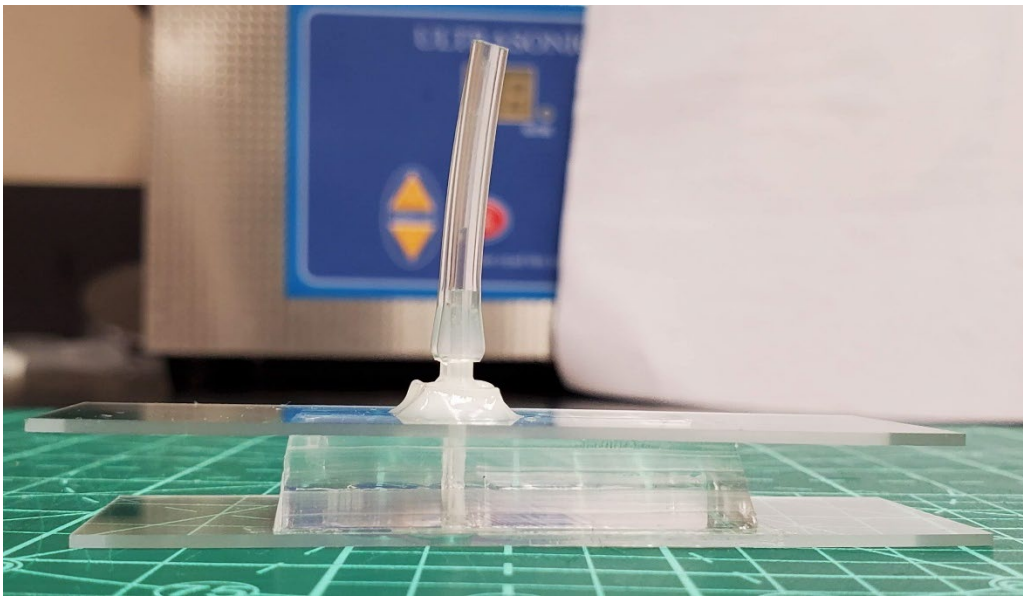

Figure 3.21. Final assembled micromodel. The inlet and outlet delivery ports were first attached to a clean microscope slide, on which two through hole were drilled and the microscope slides with attached delivery port were then bonded to the micromodel.

3.3 Image Acquisition and Analysis

3.3.1 Optical Setup

The particle images are captured employing the epi-fluorescence technique relying on an inverted microscope (Olympus IX-71), a scientific CMOS camera (Phantom VEO 440), and a green LED (Thorlabs SOLIS-525C M00569931), as illustrated in Figure 3.22. A 1.2x coupler is used to mount the camera to the microscope. Most importantly, a cylindrical lens of 150 mm in

focal length is added in the camera coupler between the camera and microscope to introduce astigmatism into the optics. The green LED light passing an excitation filter of $\lambda = 528 \pm 19$ nm is used to excite the fluorescent particles embedded in the PDMS membrane. The fluorescence emitted from the fluorescent particles is passed through a $\lambda = 617 \pm 36.5$ nm bandpass filter, focused by the microscope equipped with an objective lens with 20x magnification and 0.4 numerical aperture (NA) (Olympus UIC 2), then passed through the cylindrical lens and finally arrives at the detector of the camera.

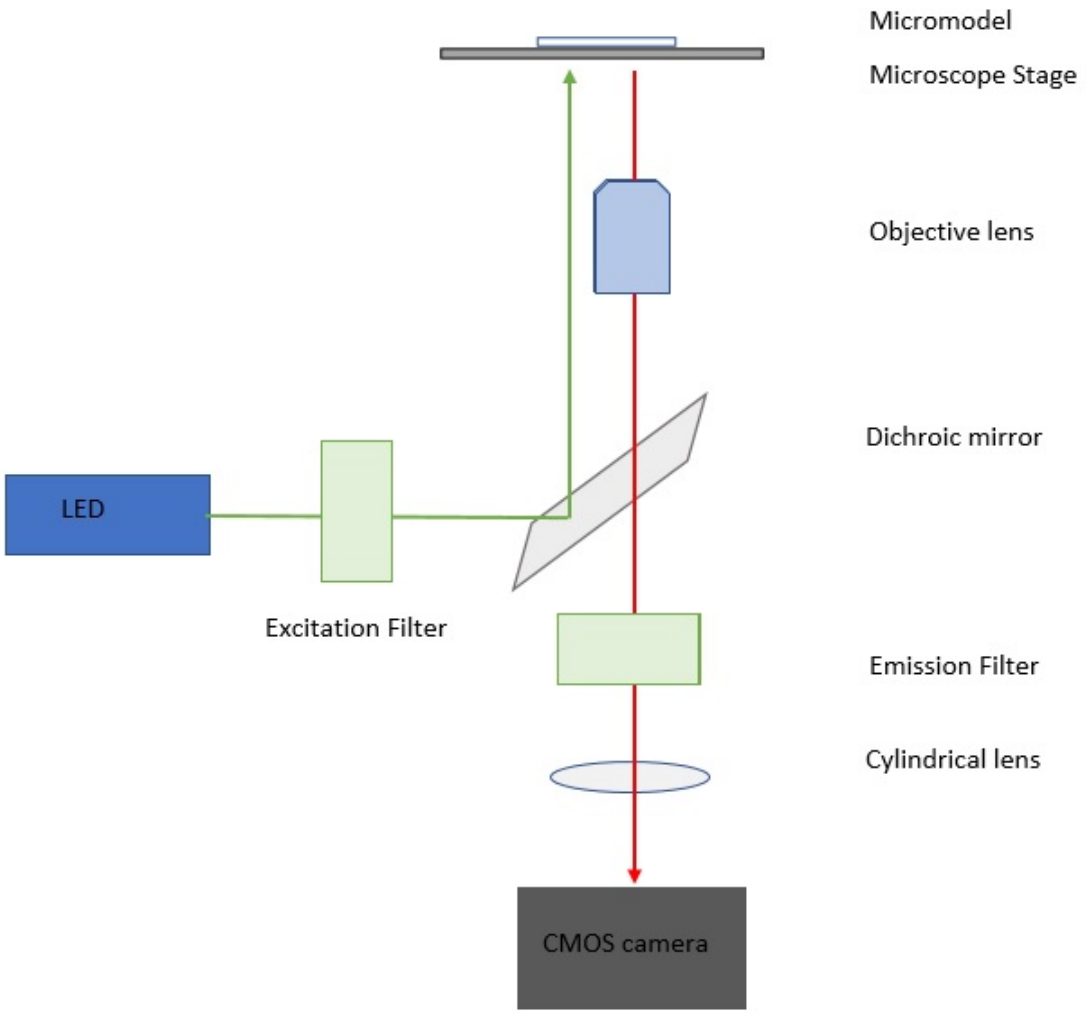

Figure 3.22. Schematic of the optical setup of the experiment. The green lines indicate the path of excitation light from the LED and the red lines indicate the path of fluorescence emitted by the particles.

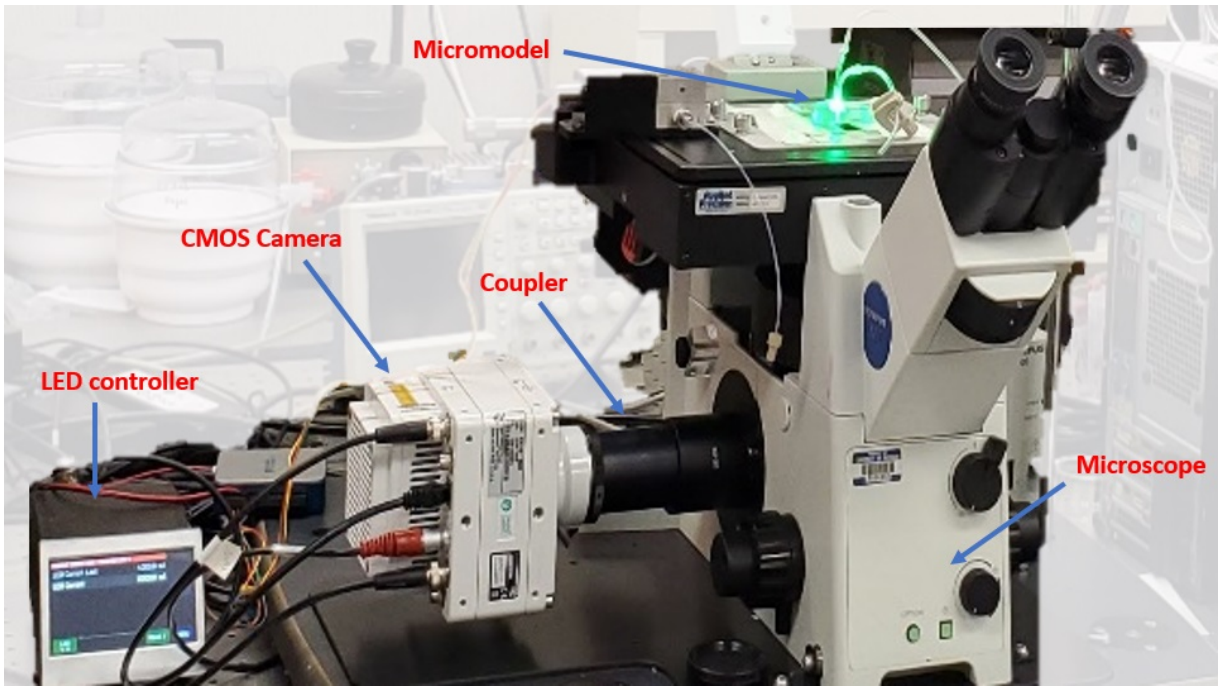

Figure 3.23. Experimental setup showing the micromodel, the microscope, the camera and the LED controller.

With the current configuration, the effective magnification is M = 24x, combining the magnifying power of both the objective and the camera coupler. The camera sensor is made up of a matrix of 2560 × 1600 pixels with each pixel being a 10 × 10 μm^2 square, resulting in a physical size of 25.6 × 1.6 mm^2., which corresponds to a final field of view (FOV) of 1.06 × 0.66 mm^2. This FOV allowed to image two pressure taps simultaneously when they are close by, but only one pressure tap at a time when they are far apart. A sample image is shown in Figure 3.24.

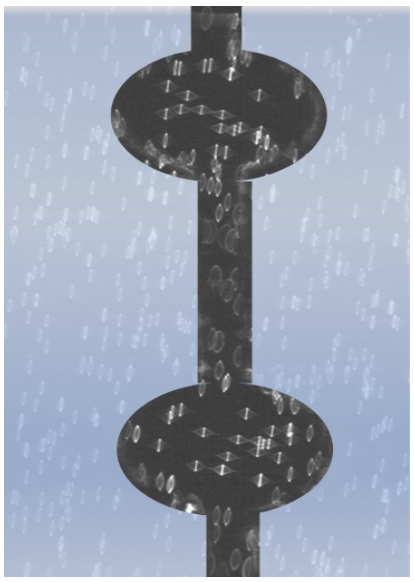

Figure 3.24. An example image capture using the aforementioned optical setup. The image is cropped to show the region of interest (ROI) better. The two ovals indicate the locations of the pressure taps and the rectangular channels are the venting channels connected to the atmosphere. The bright spots are images of fluorescent particles, which display different shapes depending on their distance from the microscope objective lens.

3.3.2 Image Acquisition

The Phantom camera was controlled by the Phantom Camera Control (PCC) software to capture static particle images. To optimize the image quality and thus maximize the signal-to-noise ratio (SNR), the imaging parameters of the cameras were set to: Brightness = 7.0, Gain = 6.000, Gamma = 1.000, Toe = 1.000, Filter = None and Sensitivity = 3.000. In all the experiments, a sequence of 100 8-bit images were acquired at a frame rate of 25 fps using the continuous mode of image capturing. The exposure time was set to 10 ms with exposure index of 6400. After the images were captured, they were exported and saved as Cine files ready to be processed using MATLAB.

3.4 Calibration

To develop the relationship between the applied pressure in the microchannel and the membrane deflection, two different calibrations are performed, namely, the *Z*-position calibration and the pressure calibration. The *Z*-position calibration aims to get the particle images at a series of prescribed z positions, whereas the pressure calibration aims to get the particle images at a series of prescribed pressures. The calibrations were done with the outlet of the sensor closed to avoid a pressure difference created by atmospheric pressure and applied pressure. By properly correlating the two sets of particle images, a relation between the applied pressure and membrane deflection can be achieved, which will be crucial to inferring pressure measurement based on particle images in further experiments.

3.4.1 *Z* position Calibration

For the Z-position calibration, the shapes of the fluorescent particles which are embedded into the PDMS membrane were captured at different heights. The initial position of the objective was set such that the particles were vertically elongated as shown in the in Figure 3.25a and this image was used as the reference image at 0 μm. Then the objective was moved gradually towards the micromodel at an increment of 1 μm and static images corresponding to each *Z*-position were captured. With the change in the height difference between the objective and the micromodel, the shape of the particle changed from vertical elongation to horizontal elongation. This procedure was continued until the particles became elongated horizontally as shown in Figure 3.25c, which occurs after the objective travel a distance of 50 μm from its original position. By this procedure a set of images containing information of particle shapes at various distances from the objective

was obtained, which were used later as reference images to determine the distance between the membrane and the microscope objective based on the particle shapes acquired in real experiments.

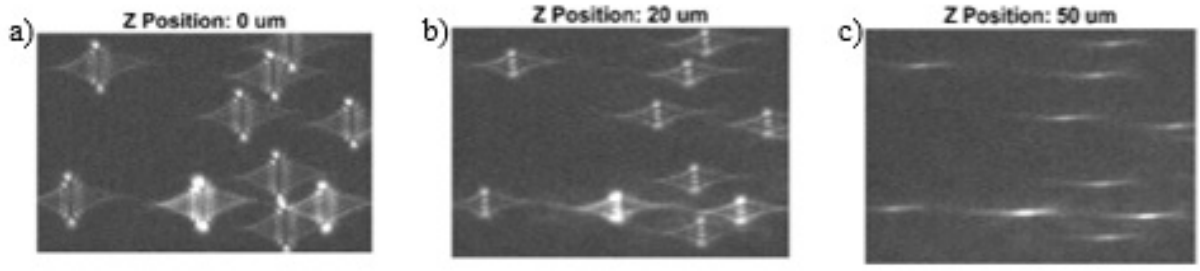

Figure 3.25. Representative particle images captured at different z locations: a) the initial position (0 µm); b) 20 µm away from the initial position, c) 50 µm away from the initial position. The shapes of the fluorescent particles change from vertical elongation to horizontal elongation as the objective is moved closer.

3.4.2 Pressure Calibration

The pressure calibration is intended to capture the shapes of fluorescent particles at various prescribe pressures, controlled by varying the height of a water tank which sustains hydrostatic pressure as shown in Figure 3.26. By raising or lowering the height of the water tank, the pressure can be changed according to the hydrostatic pressure equation of,

$$P = \rho g(H - h) \qquad (3)$$

Where P is the hydrostatic pressure, ρ is the density of the fluid, g is the gravitational acceleration, H is the height of the water in the tank relative to the optical table and h is the height of the water in the glass bottle again relative to the optical table. The water tank and the glass bottle on the right were both filled with water and the level difference between them creates the net hydrostatic pressure. A second glass bottle was used as a buffer chamber to separate the micromodel from the driving fluid which can be contaminated after repeated use. For this calibration, the second glass

bottle and the downstream plumbing lines were all filled with static air, so that there was negligible pressure change between the second glass bottle and the inside of the micromodel.

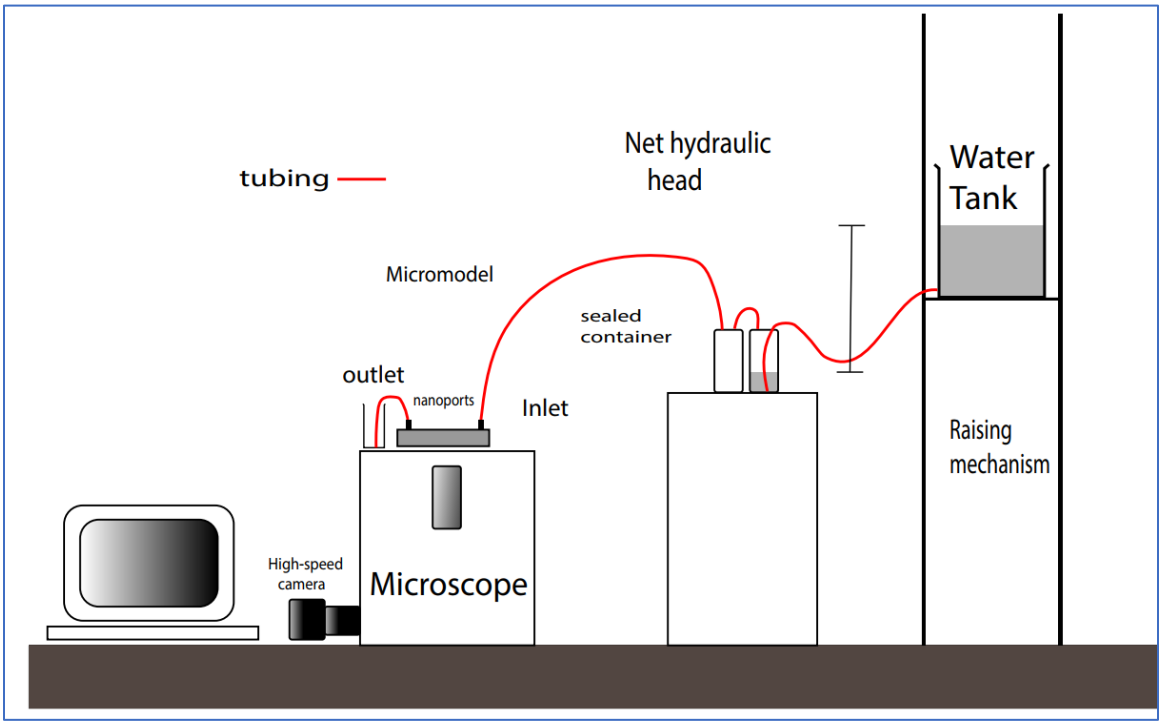

Figure 3.26. A schematic diagram of the setup used for pressure calibration.

The pressure calibration was carried out by lowering the tank to its minimum height level, and the first glass bottle with driving fluid was opened to atmosphere to reach equilibrium condition. After it reached equilibrium, the glass bottle was sealed tightly, and the valve was opened to connect the second glass bottle to the micromodel. The shape of the fluorescent particles was then captured at that instance as the reference image corresponding to a pressure difference of 0 Pa (Figure 3.27a), when the height of the liquid in the tank and the height of the liquid in the glass bottle are at same level. After recording the image, the valve was closed, and the height of the tank was raised by 1 cm. Then, the height of the water tank (H), and any change in the height

of driving liquid in the glass bottle (h) was recorded. The valve was opened back up and the shape of the fluorescent particles was imaged again after a waiting period of 2 min when the systems reached a new equilibrium state. This procedure was repeated until the particles elongated horizontally similar to that in the Z position calibration (Figure 3.27b).

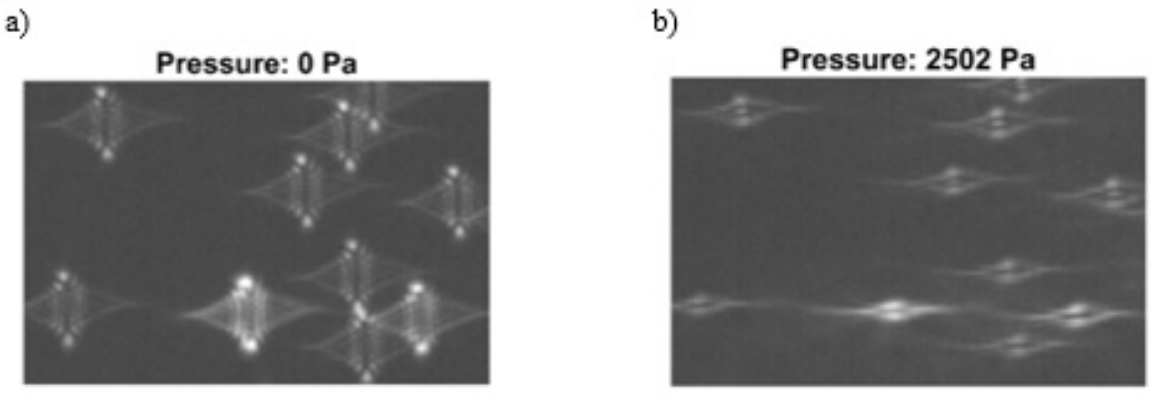

Figure 3.27. Two representative images captured at reference pressure of 0 Pa (a), and a pressure of 2502 Pa (b), respectively. The change in shape of the fluorescent particles from vertical elongation to horizontal elongation can be observed.

3.5 Image Analysis

The acquired particle images were processed using MATLAB R2019a software to obtain a relationship between applied pressure and membrane deflection. To do that, a region of approximately 50 by 60 pixels in the center of the pressure tap was selected as the ROI in the pressure calibration images with the help of the ImageJ software, as shown in Figure 3.28. The region corresponding to same particles were also selected in the *Z*-position calibration images. It is worth noting that when defining the ROI for the *Z*-position calibration images, the window was purposefully expanded by 5 pixels in all four direction to ensure proper calculation of cross-correlations in the following steps.

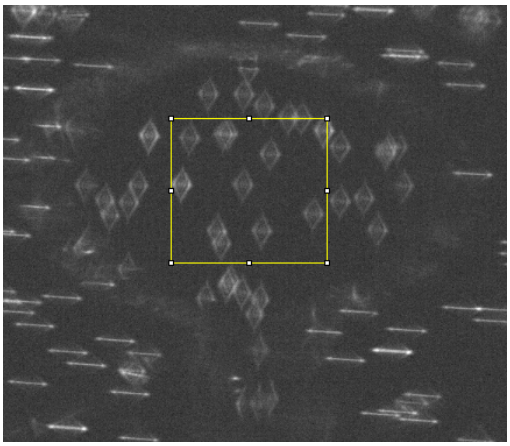

Figure 3.28. The ROI selected for image analysis as indicted by the yellow box.

Next, for each pressure calibration image corresponding to a known pressure, the cross-correlation coefficients were calculated between it and all *Z*-position calibration images at various positions. A higher cross-correlation coefficient indicates a better similarity between two images, whereas a lower value indicates the opposition. Once all coefficients were calculated, a curve could be plotted as shown in Figure 3.29 and the peak location was identified by fitting a polynomial to the plot using the built-in "polyfit" function in MATLAB. Using this approach, each pressure calibration image was matched with a *Z*-position calibration image, essentially producing a relationship between the applied pressure and the membrane deflection.

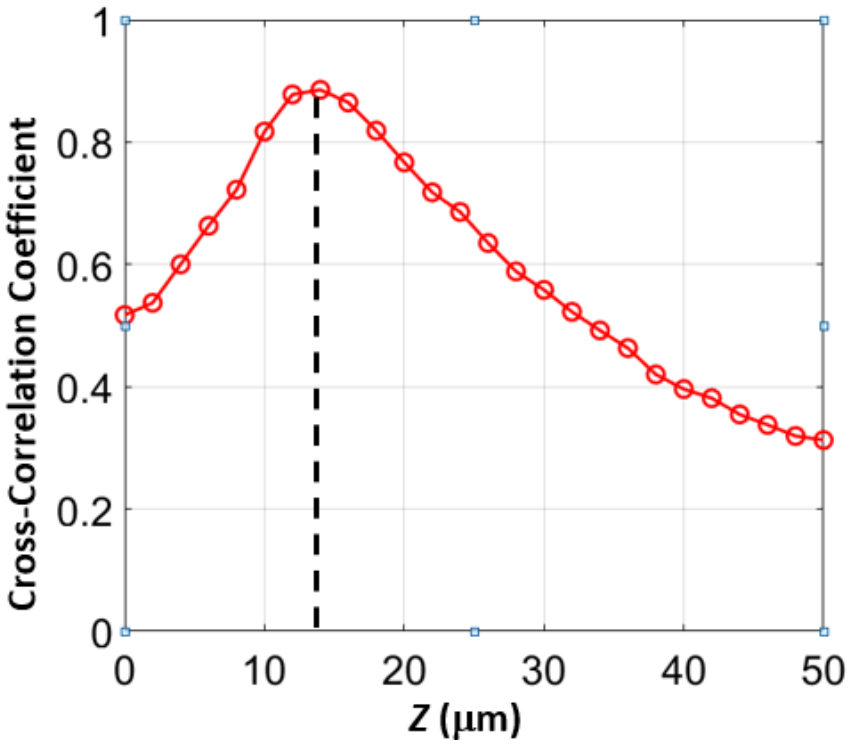

Figure 3.29. Cross-correlation coefficients between on pressure calibration image and all Z position calibration images. The location of the peak value represents the corresponding Z-position of the membrane under the applied pressure.

CHAPTER 4

RESULTS AND DISCUSSION

In this chapter, we present and discuss the results of the calibration experiments, the pressure drop measurement in single-phase flow and the capillary pressure measurement in a simple multiphase flow experiment. Additionally, the sensitivity and stability of the pressure sensors will be discussed.

4.1 Pressure –Deflection Relation

The pressure – deflection relation obtained from the calibration experiment is plotted in Figure 4.1 and fitted into a second order polynomial curve. The least-square fit for the curve shows that the membrane has good linearity in the lower pressure range of 0 – 1 kPa with a sensitivity of ~ 0.066 kPa/μm and in the high pressure range of 1.8 – 2.92 kPa, the sensitivity is 0.155 kPa/μm. The root mean square deviation of static pressure measurement is less than 0.04 kPa over the entire pressure range which corresponds to < 1.22% of full-scale value of 2.92 kPa. With the pressure tap depth of 43.85 μm, it is ensured that the membrane is completely tested in its linear region, as the maximum pressure that fully deform the membrane is calculated as 5.73 kPa. Although based on Equation 1, the deflection at the center of the membrane (r = 0) should be proportional to pressure variation, our calibration curve herein is not a perfect linear relationship. This can be attributed to fact that in the higher-pressure range, the deflection can be so large (compared to its diameter) that it is not precisely described by Equation 1. The 2nd order polynomial is an acceptable

function of the membrane used in a sensor. Therefore, this pressure – deflection relation is used in continuing studies of single-phase flow, and multiphase flow in Sec. 4.2 and 4.3.

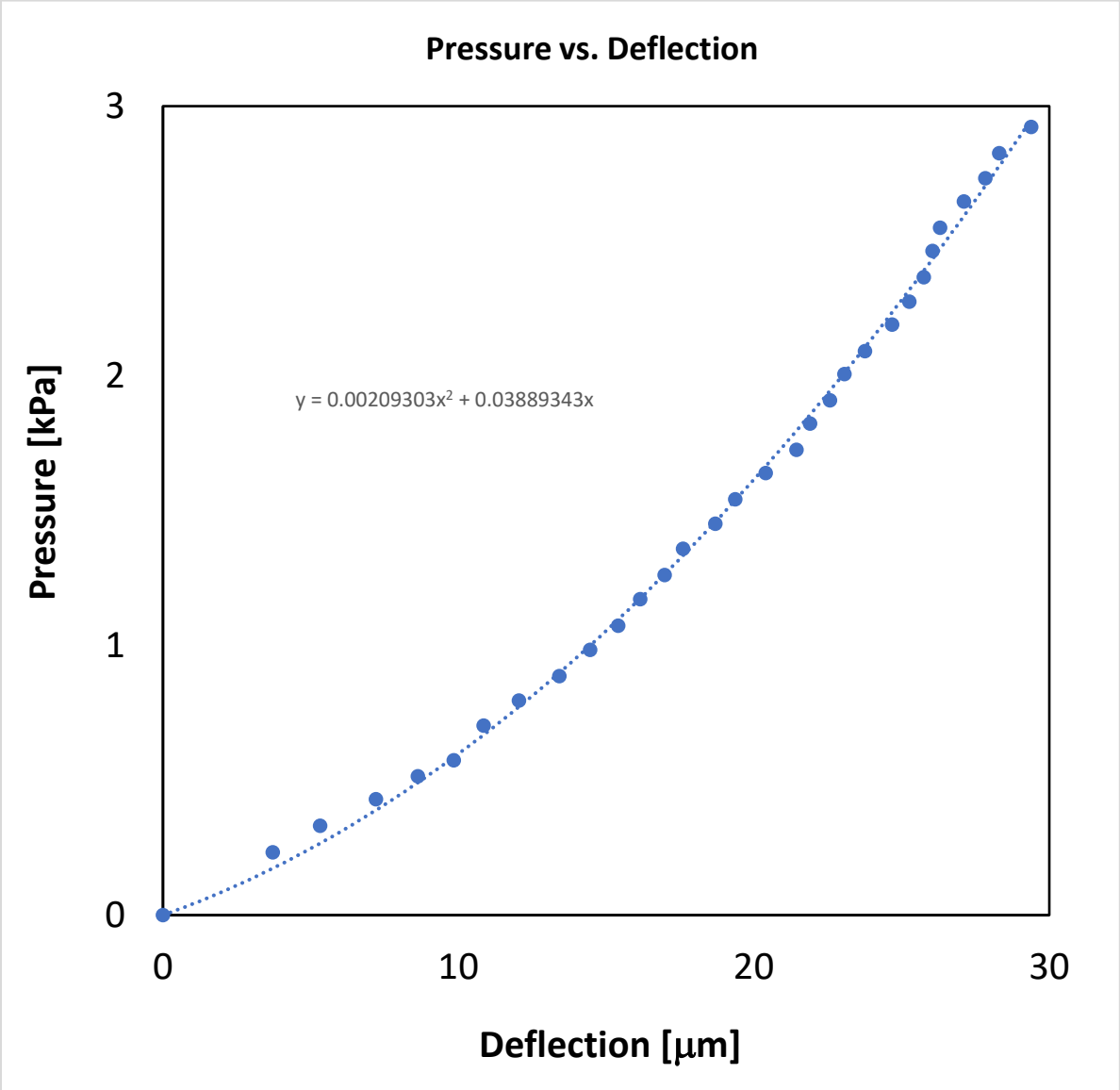

Figure 4.1. Calibrated relationship between pressure (kPa) and membrane deflection (µm) obtained for the 200 µm downstream pressure tap.

4.2 Single-Phase flow

To validate the functionality of our pressure sensor, viscous pressure drop was measured in a microchannel using both air and deionized (DI) water as the working fluids, at constant flowrates with a setup shown in Figure 4.2. The flow was controlled by a high-precision syringe pump (Harvard Apparatus, PHD 22/2000). The inlet and outlet were also connected to a pressure transducer (Validyne, P55E) as a benchmark reference, whose reading was continuously logged using a NI DAQ (National Instrument Data Acquisition system, USB-6001) and LabView software.

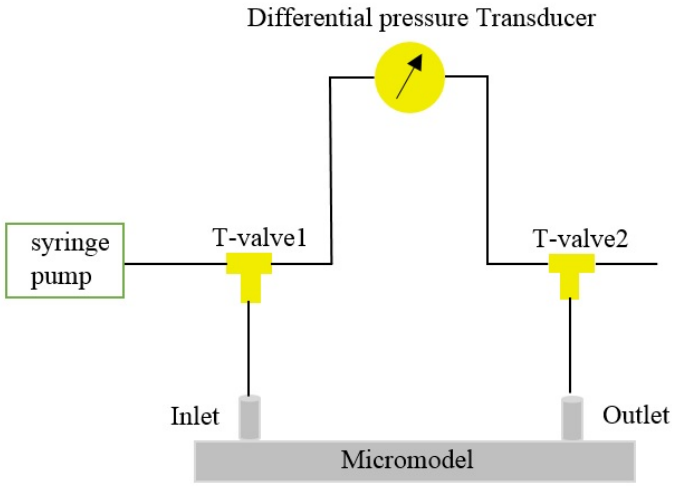

Figure 4.2. Schematic of the viscous drop pressure measurement setup. The flowrate is controlled by the syringe pump connected to the inlet of the microchannel. The outlet is opened to atmosphere. The pressure drop across the microchannel is also measured with a differential pressure transducer.

For the air flow experiment, the flowrate was incrementally increased from 0 to 1.2 ml/min with a step of 0.1 ml/min and then decreased from 1.2 back to 0 ml/min with a step of 0.2 ml/min. The Reynolds number at the maximum flow rate of 1.2 ml/min was calculated to be 10.8,

suggesting the occurrence of laminar flows in the microchannel. A wait of 2 min before each measurement at a certain flow condition was used to ensure a steady-state flow during image acquisition. The same MATLAB image analysis algorithm discussed in Sec 3.5 was used to calculate the membrane deflection for each applied flow rate by correlating the flow measurement images and the *Z*-position calibration images. Once the membrane deflection was determined, it was substituted into the pressure-deflection relation shape as determined earlier (*e.g.*, Figure 4.1), to determine the pressure exerted at each of the pressure sensors at upstream and downstream locations. The difference between the pressures yields the viscous pressure drop within the microchannel.

Figure 4.3 shows the variation of pressure drop within the microchannel as a function of flow rate. As expected for laminar flow, the pressure drop is proportional to the flow rate, resulting in a linear relationship. The error bars represent the combined error propagated from uncertainties in the calibration relationship and uncertainness in the membrane deflection calculation. The sensor has a sensitivity of ~0.93 kPa/(ml/min) over the dynamic range of 0 – 1.12 kPa for air. To validate the experimental data, it is compared with the data obtained from the externally connected pressure transducer as well as the theoretical values for pressure drop in rectangular microchannels. It can be seen that our pressure sensor measurement agrees very well with the commercial pressure transducer measurement with a root mean square deviation (RMSD) of 0.03 kPa and a maximum deviation of 0.06 kPa.

The theoretical pressure drop for a rectangular channel at a given flow rate was calculated based on Equation 4 [34],

$$\bar{\omega} = \frac{\Delta p c^2}{\mu L}\left[\frac{1}{3} - \frac{64c}{\pi^5 b}\, tanh\left(\frac{\pi b}{2c}\right)\right] \tag{4}$$

where $\bar{\omega}$ is the average velocity through the microchannel, and μ is the dynamic viscosity of the working fluid. L, b and c are length, half-width and half-height of the rectangular channel, respectively. The volumetric flowrate Q is related to the average velocity $\bar{\omega}$ by Equation 5. Substituting Equation 5 into Equation 4, an analytical solution of pressure drop as a function of flow rate in a rectangular microchannel is obtained as shown in Equation 6.

$$Q = (w \times h)\,\bar{\omega} \tag{5}$$

$$\Delta P = \frac{4\mu L}{wh^3\left[\frac{1}{3} - \frac{64}{\pi^5}\frac{h}{w}\tanh\left(\frac{\pi w}{2h}\right)\right]}\,Q \tag{6}$$

Employing Equation 6, the theoretical values were calculated based on the prescribed flow rates and microchannel dimension measured using a 3D profilometer (FILMETRICS, The Profilm 3D-200). As shown in Figure 4.2, the theoretical values are in reasonable agreement with the experimentally measured values using our sensors, with a RMSD of 0.12 kPa and maximum deviation of 0.17 kPa. We believe the relatively large deviation between the experimental measurements (both from the pressure sensor and the pressure transducers) and theoretical predation is due to inaccurate determination of the microchannel dimensions. Moreover, it is well known that PDMS microchannels fabricated using soft lithography do not have perfectly rectangular cross-sections, which can potentially contribute to the deviation observed.

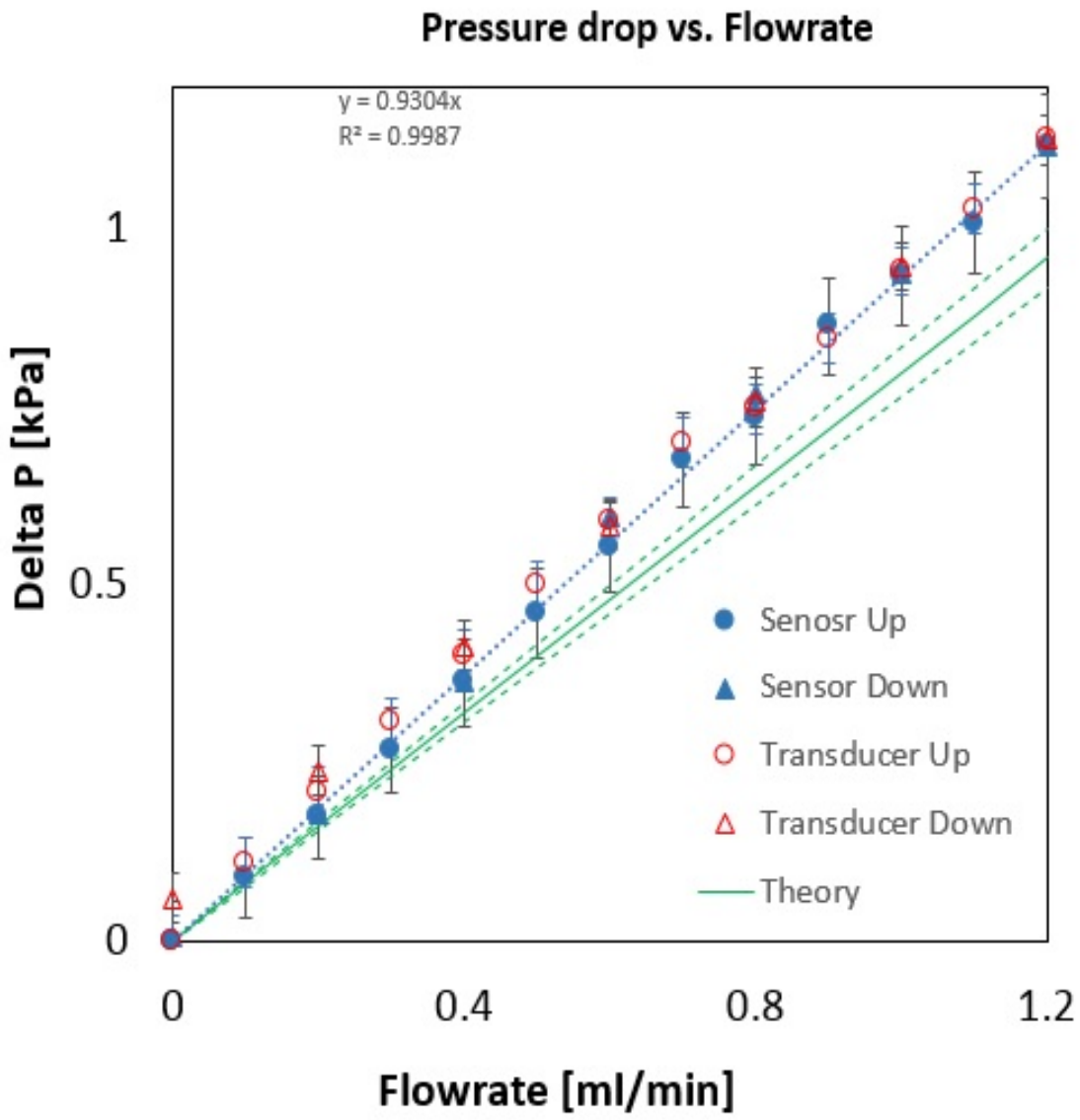

Figure 4.3. Pressure drops at various flow rates obtained using our sensor (blue symbols), the pressure transducer (green symbols) and theoretical prediction (red lines) for the single-phase air flow in the microchannel at various flowrates. The "Up" and "Down" plots correspond to increasing and decreasing flowrate measurements, respectively, and the dashed lines are the upper and lower bounds of the theoretical predictions based on propagated errors, which is approximately 4.4% of the predicted values.

Next the same experiment was performed using DI water as the working fluid at different flowrates. Due to the much higher dynamic viscosity of water compared with air, the flow rate was

reduced by two orders of magnitude, so that the pressure drop falls within the measurement range of the sensors. The new increasing flowrate were set from 0 to 0.012 ml/min with an increment of 0.001 ml/min and a decreasing flowrate from 0.012 to 0 ml/min with a decrement of 0.002 ml/min. The Reynolds number corresponding to the highest flowrate is 1.6, again confirming the laminar flows in the microchannel. Figure 4.4 shows the variation of pressure drop within the microchannel as a function of flow rate again but using DI water as the working fluid. A linear curve fit to the pressure sensor data gives a square of the correlation coefficient $R^2 = 0.9905$ demonstrating a linear relationship between pressure drop and flow rate, as expected for a laminar flow. Again, to validate the experiment, the pressure transducer and theoretical values were plotted on the same figure. It can be seen that the pressure sensor and the pressure transducer are in good agreement in the flow rate range of 0 to 0.006 ml/min. However, beyond 0.006 ml/min, the two measurements start to deviate. We believe, with good reason that this deviation was due a temporary malfunction of the pressure transducer by observing that the pressure was dropping when increasing the flowrate in the Labview data for the pressure transducer. The theoretical pressure drop was calculated again using Equation 6. Again, the theory underpredicts the pressure sensor measurement with a RMSD of 0.09 kPa and maximum deviation of 0.21 kPa. The imperfect cross-sectional shape of the PDMS microchannel presumably led to the difference between the theoretical and experimental values. The sensitivity of the sensor is 58.59 kPa/(ml/min) for the dynamic range of 0.72 kPa.

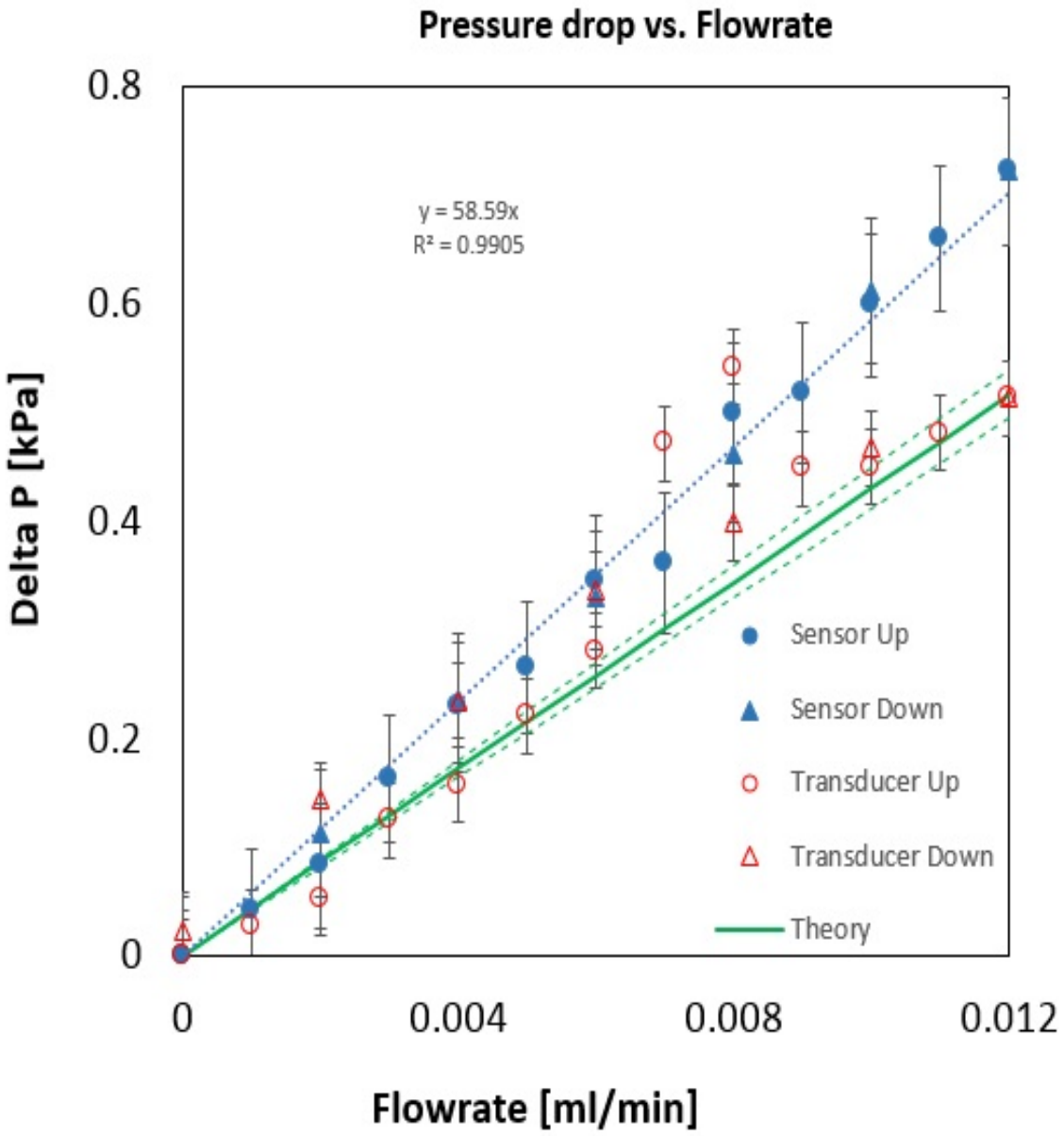

Figure 4.4. Similar to Figure 4.3 but using water as the working fluid. Again, the dashed lines are the upper and lower bounds of the theoretical predictions based on propagated errors, which is approximately 4.4% of the predicted values.

4.3 Multi-Phase flow

The multi-phase flow experiment for capillary pressure measurement was conducted with a mixture of air and DI water as the two phase fluid in a similar setup as used for the single-phase flow. To initiate the experiments, the microchannel was first presaturated with DI water using the syringe pump at a flowrate of 0.005 ml/min. Extra care was taken during this step to prevent any air bubbles from getting into the microchannel. Then the syringe pump was stopped for a wait time of 5 minutes to let the flow subside before take particle images at zero flow rate, which were then used as the reference position (zero membrane deflection) in the subsequent image processing. Next air was slowly injected into the microchannel at the same flowrate of 0.005 ml/min. As the air enters the microchannel, an air-water interface is created, which generates a temperature jump (capillary pressure) across the interface due to surface tension and interfacial curvature. It is worth noting that PDMS is in general hydrophobic. In fact, our measurement shows that the static contact angle of water on PDMS surface is ~110^{o} (Figure 4.5a). However, as water is being displaced out of the microchannel, the receding contact angle is more relevant. Our measurement indicates a receding contact angle of ~ 60^{o} for water receding on PDMS surface. The entire process of air displacing water was recorded and again processed in MATLAB as discussed earlier.

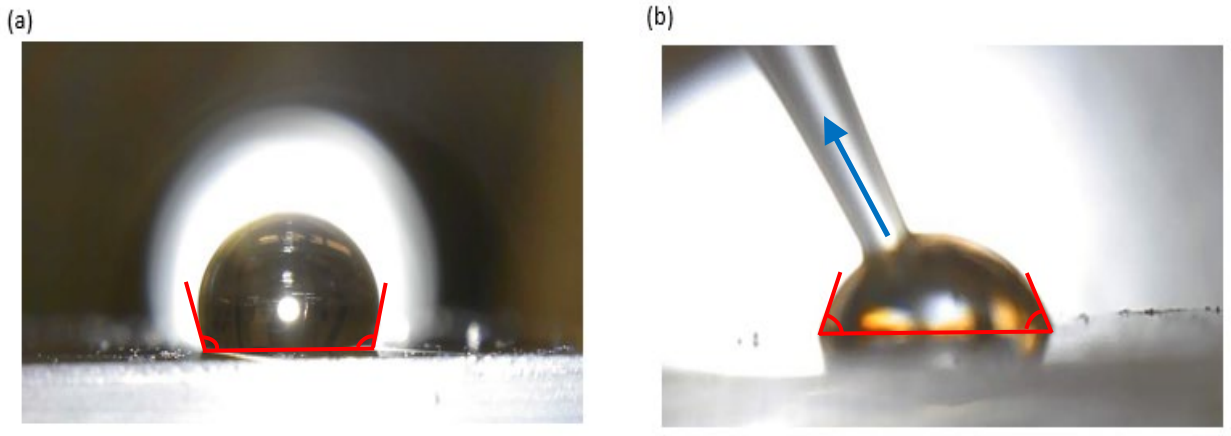

Figure 4.5. (a) To measure the static contact angle, 20 µL of DI water is dispensed onto the surface of a PDMS slab to form a sessile droplet and images of the droplet shape were captured using a USB microscope (Koolertron, AS-SMXW33) viewing from the side. The contact angle was measured in ImageJ using the "Drop Analysis" plugin. (b) To measure the receding contact angle, the same setup was used. The only difference is that the droplet shape was imaged as water was being withdrawn from the droplet using a pipette, which led to a shrinking droplet, generating the receding contact angle at the droplet edge. The static and receding contact angles are 110° and 60°, respectively.

As shown in Figure 4.6, when the air-water interface is between the two pressure sensors (Figure 4.6a), a high pressure is exerted on the upstream pressure sensor, leading to a larger deformation therein (Figure 4.6c). Due to the low dynamic viscosity of air and the low flow rate, the contribution to pressure drop due a to viscous effect is negligible. Therefore, the pressure difference measured between the upstream sensor and the downstream sensor is indeed due to capillary pressure generated across the interface. However, when the air-water interface passes the downstream sensor (Figure 4.6b), both sensors are on the air side with little pressure difference detected (Figure 4.6d). Using the pressure sensors, the capillary pressure across the air-water interface was calculated to 1.54 kPa.

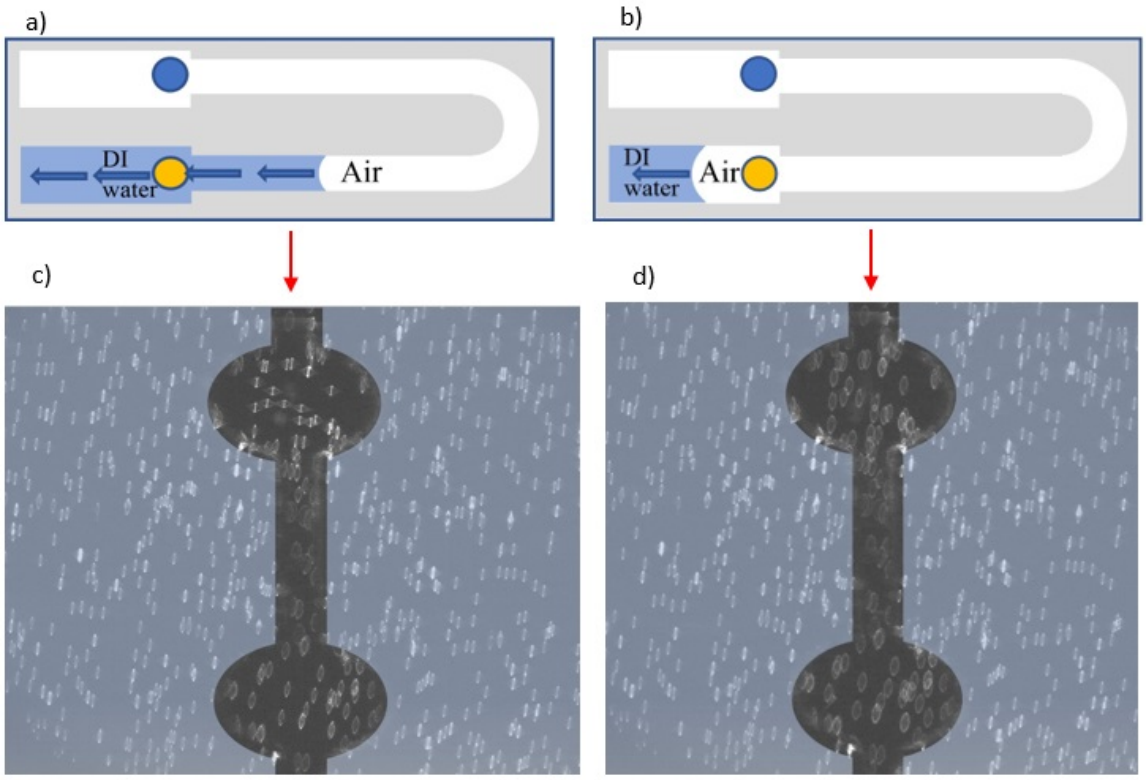

Figure 4.6. a) when the air – DI water interface is in the 100 µm narrow channel. b) when the air-DI water interface is exiting the 100 µm narrow channel, c) and d) are the acquired particle shape images corresponding to each of the interface locations. The arrows indicate the flow direction.

According to the Young-Laplace equation, a theoretical value of capillary pressure can be calculated based on the microchannel dimensions, the water surface tension and the receding contact angle as shown below

$$p^c = 2\sigma\left(\frac{1}{w} + \frac{1}{d}\right) cos\theta \tag{7}$$

where p^c is the capillary pressure, σ is the surface tension of water, w and d are the width and depth of the microchannel, respectively, and θ is the contact angle of the wetting phase. Using Equation 7, the theoretical capillary pressure was calculated as 1.21 kPa, which deviates from the measured value by 21.43%. We note that although a more than 20% difference seems to be large, it still

represents a big improvement compared with previous capillary pressure measurement based on interfacial curvature [35].

4.4 Sensor Stability Test

Properties of PDMS are known to change over time. For instance, the PDMS material gets stiffer with an increasing Young's modulus over time. To ensure that our pressure calibration curves are not significantly impacted by this effect, we performed a stability test to determine the change of the calibration curve over time. Figure 4.7 shows the results of two pressure-deflection relations obtained with a time difference of 24 hours. As expected, the membrane gets more rigid over time, leading to a slightly higher pressure on the 2nd day for the same amount of membrane deflection. The RMSD between the two curves is found to be 34.51 Pa, which is ~3% of the dynamic range of 2.50 kPa within the tested period. It is worth noting that for all the experiments presented in the thesis, a new calibration was performed before each data collection, and the actual flow and capillary pressure measurement were performed within 10 hours of the calibration, eliminating any potential issues of sensor stability over time.

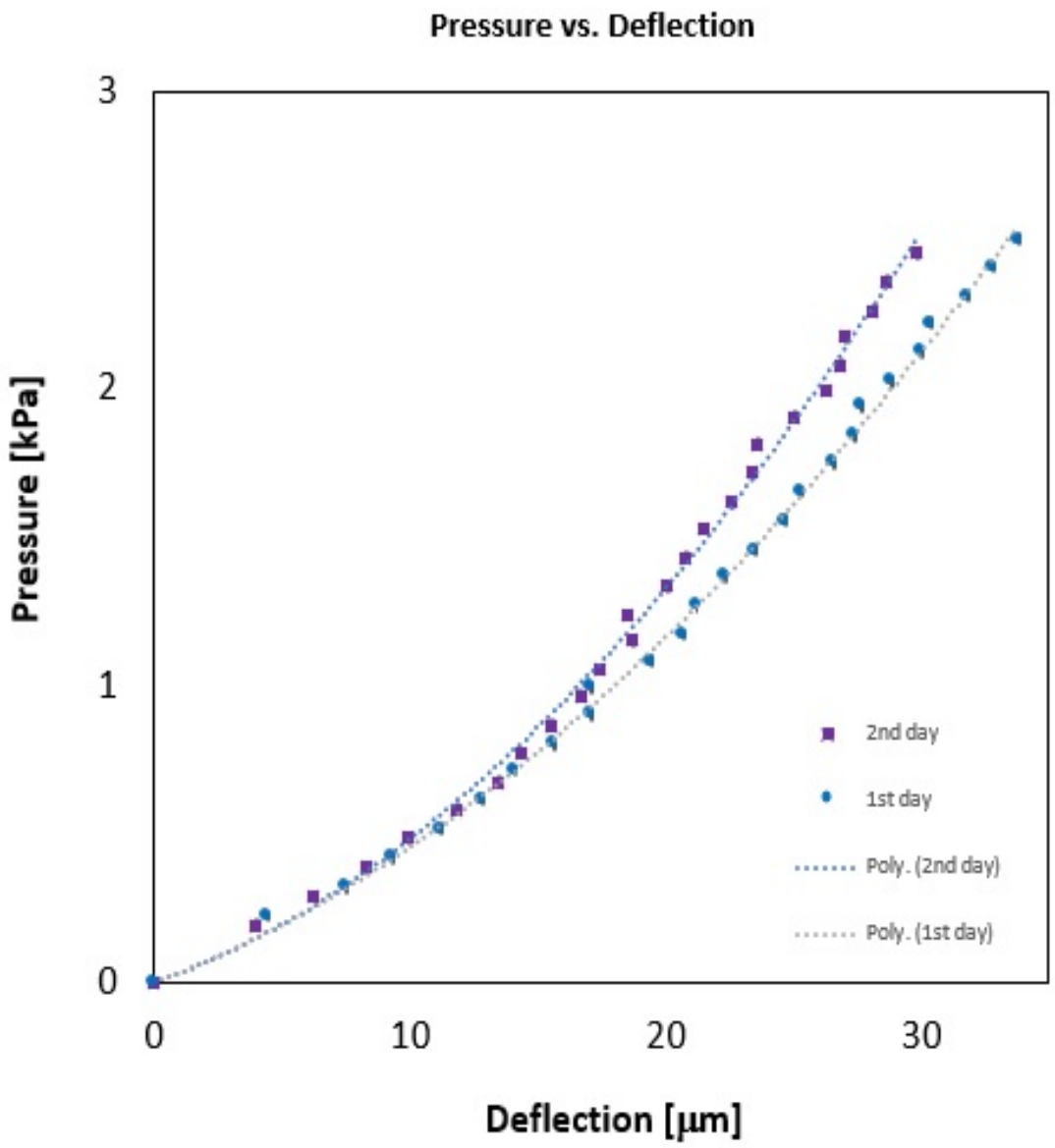

Figure 4.7. The Pressure - deflection calibration curves obtained for the same device on two consecutive days.

CHAPTER 5

CONCLUSION AND FUTURE WORKS

This chapter summarizes the conclusions of the thesis work and recommendations for future research directions.

5.1 Conclusion

As per the objectives of this thesis, a membrane-based microfluidic pressure sensor has been successfully designed and fabricated using simple soft lithography. By embedding 1 μm fluorescent particles into the thin membrane, and using Astigmatic Particle Tracking scheme, the membrane deflection is detected based on the shape of the particles. The simple optical readout method and image processing algorithm have led to fast and precise pressure measurements under single and multiphase flow conditions in the microchannel.

The current sensor has a measurement range of 2.92 kPa with an accuracy of ~ 60 Pa. The sensor has been successfully applied to measure the pressure drop within a microchannel for single-phase flow of air and DI water. Good agreement has been achieved between the pressure sensor, a commercial pressure transducer and theoretical prediction. Similarly, for the multiphase flow of air and water, the sensor successfully measured the capillary pressure with a 20% deviation from the theoretical deviation. As for the stability, a change of 3% was estimated for a period of 24 hours. The capability demonstrated by the pressure sensor is promising and this work opens the door to a renewed understanding of pore-scale physics of multiphase flow in porous media.

5.2 Recommendations for future work

This current work only demonstrated pressure sensors consisting of two pressure taps. However, with a simple change of the photomask design, a 2D array of pressure taps can be fabricated without extra design or fabrication steps, which will enable a true 2D pressure field mapping. This represents an important direction for future work.

Second, the sensitivity and measurement range of the pressure sensor can be finely tuned by adjusting parameters such as the pressure sensor size, PDMS membrane thickness, and even the Young's modulus of the PDMS material, which has not been explored in the current work. A parametric study of the system will be useful to gain a better understanding of the device performance, and help to accommodate more challenging measurements, such as 2D pressure mapping of multiphase flow in porous medium.

Finally, as mentioned previously, the surface properties of PDMS such as the wettability is not stable, and PDMS itself is incompatible with many solvents and oils, which may limit its application in many multiphase flow scenarios. To partially alleviate this issue, coatings could be tested and applied to the PDMS microchannels and membranes to expand its compatibility.

REFERENCES CITED

1. Matsunaga, T., Hosokawa, M., Arakaki, A., Taguchi, T., Mori, T., Tanaka, T., & Takeyama, H. (2008). High-efficiency single-cell entrapment and fluorescence in situ hybridization analysis using a poly (dimethylsiloxane) microfluidic device integrated with a black poly (ethylene terephthalate) micromesh. *Analytical chemistry*, *80*(13), 5139-5145.
2. Crane, M. M., Chung, K., Stirman, J., & Lu, H. (2010). Microfluidics-enabled phenotyping, imaging, and screening of multicellular organisms. *Lab on a Chip*, *10*(12), 1509-1517.
3. Crane, M. M., Chung, K., & Lu, H. (2009). Computer-enhanced high-throughput genetic screens of C. elegans in a microfluidic system. *Lab on a Chip*, *9*(1), 38-40.
4. Shackman, J. G., Dahlgren, G. M., Peters, J. L., & Kennedy, R. T. (2005). Perfusion and chemical monitoring of living cells on a microfluidic chip. *Lab on a Chip*, *5*(1), 56-63.
5. Lee, P. J., Gaige, T. A., & Hung, P. J. (2009). Dynamic cell culture: a microfluidic function generator for live cell microscopy. *Lab on a Chip*, *9*(1), 164-166.
6. Armstrong, R. T., McClure, J. E., Berrill, M. A., Rücker, M., Schlüter, S., & Berg, S. (2016). Beyond Darcy's law: The role of phase topology and ganglion dynamics for two-fluid flow. *Physical Review E*, *94*(4), 043113.
7. Godinez-Brizuela, O. E., Karadimitriou, N. K., Joekar-Niasar, V., Shore, C. A., & Oostrom, M. (2017). Role of corner interfacial area in uniqueness of capillary pressure-saturation-interfacial area relation under transient conditions. *Advances in Water Resources*, *107*, 10-21.
8. Gray, W. G., Bruning, K., & Miller, C. T. (2019). Non-hysteretic functional form of capillary pressure in porous media. *Journal of Hydraulic Research*, *57*(6), 747-759.
9. Karadimitriou, N. K., Musterd, M., Kleingeld, P. J., Kreutzer, M. T., Hassanizadeh, S. M., & Joekar-Niasar, V. (2013). On the fabrication of PDMS micromodels by rapid prototyping, and their use in two-phase flow studies. *Water Resources Research*, *49*(4), 2056-2067.
10. Karadimitriou, N. K., Hassanizadeh, S. M., Joekar-Niasar, V., & Kleingeld, P. J. (2014). Micromodel study of two-phase flow under transient conditions: Quantifying effects of specific interfacial area. *Water Resources Research*, *50*(10), 8125-8140.
11. Liu, Y., Nolte, D. D., & Pyrak-Nolte, L. J. (2011). Hysteresis and interfacial energies in smooth-walled microfluidic channels. *Water Resources Research*, *47*(1).
12. McClure, J. E., Armstrong, R. T., Berrill, M. A., Schlüter, S., Berg, S., Gray, W. G., & Miller, C. T. (2018). Geometric state function for two-fluid flow in porous media. *Physical Review Fluids*, *3*(8), 084306.
13. Miller, C. T., Bruning, K., Talbot, C. L., McClure, J. E., & Gray, W. G. (2019). Nonhysteretic Capillary Pressure in Two-Fluid Porous Medium Systems: Definition, Evaluation, Validation, and Dynamics. *Water Resources Research*, *55*(8), 6825-6849.
14. Abkarian, M., Faivre, M., & Stone, H. A. (2006). High-speed microfluidic differential manometer for cellular-scale hydrodynamics. *Proceedings of the National Academy of Sciences*, *103*(3), 538-542.

15. Zhu, Y., Antao, D. S., Chu, K. H., Chen, S., Hendricks, T. J., Zhang, T., & Wang, E. N. (2016). Surface structure enhanced microchannel flow boiling. *Journal of Heat Transfer*, *138*(9).
16. Shen, F., Ai, M., Ma, J., Li, Z., & Xue, S. (2020). An easy method for pressure measurement in microchannels using trapped air compression in a one-end-sealed capillary. *Micromachines*, *11*(10), 914.
17. Chaudhury, A. R., Pantazis, A. K., & Chronis, N. (2016). An image contrast-based pressure sensor. *Sensors and Actuators A: Physical*, *245*, 63-67.
18. Orth, A., Schonbrun, E., & Crozier, K. B. (2011). Multiplexed pressure sensing with elastomer membranes. *Lab on a Chip*, *11*(22), 3810-3815.
19. Song, W., & Psaltis, D. (2010). Optofluidic pressure sensor based on interferometric imaging. *Optics letters*, *35*(21), 3604-3606.
20. Chung, K., Lee, H., & Lu, H. (2009). Multiplex pressure measurement in microsystems using volume displacement of particle suspensions. *Lab on a Chip*, *9*(23), 3345-3353.
21. Wang, L., Zhang, M., Yang, M., Zhu, W., Wu, J., Gong, X., & Wen, W. (2009). Polydimethylsiloxane-integratable micropressure sensor for microfluidic chips. *Biomicrofluidics*, *3*(3), 034105.
22. Chen, P. J., Rodger, D. C., Saati, S., Humayun, M. S., & Tai, Y. C. (2008). Microfabricated implantable parylene-based wireless passive intraocular pressure sensors. *Journal of Microelectromechanical Systems*, *17*(6), 1342-1351.
23. Wagner, D., Frankenberger, J., & Deimel, P. P. (1994). Optical pressure sensor using two Mach-Zehnder interferometers for the TE and TM polarization. *Journal of Micromechanics and Microengineering*, *4*(1), 35
24. Eaton, William P., Fernando Bitsie, James H. Smith, and David W. Plummer. "A new analytical solution for diaphragm deflection and its application to a surface-micromachined pressure sensor." In *International Conference on Modeling and Simulation, MSM*. 1999.
25. Roriz, P., Carvalho, L., Frazão, O., Santos, J. L., & Simões, J. A. (2014). From conventional sensors to fibre optic sensors for strain and force measurements in biomechanics applications: A review. *Journal of biomechanics*, *47*(6), 1251-1261.
26. Elwenspoek, M., Wiegerink, R., & Wiegerink, R. J. (2001). *Mechanical microsensors*. Springer Science & Business Media.
27. Bakhoum, E. G., & Cheng, M. H. (2009). Capacitive pressure sensor with very large dynamic range. *IEEE Transactions on Components and Packaging Technologies*, *33*(1), 79-83.
28. Zhang, Y., Howver, R., Gogoi, B., & Yazdi, N. (2011, June). A high-sensitive ultra-thin MEMS capacitive pressure sensor. In *2011 16th International Solid-State Sensors, Actuators and Microsystems Conference* (pp. 112-115). IEEE.
29. Jung, T., & Yang, S. (2015). Highly stable liquid metal-based pressure sensor integrated with a microfluidic channel. *Sensors*, *15*(5), 11823-11835.
30. Aref, S. H., Latifi, H., Zibaii, M. I., & Afshari, M. (2007). Fiber optic Fabry–Perot pressure sensor with low sensitivity to temperature changes for downhole application. *Optics communications*, *269*(2), 322-330.

31. Rossi, Massimiliano, and Christian J. Kähler. "Optimization of astigmatic particle tracking velocimeters." *Experiments in fluids* 55, no. 9 (2014): 1-13.
32. Cierpka, C., Rossi, M., Segura, R., & Kähler, C. J. (2010). On the calibration of astigmatism particle tracking velocimetry for microflows. *Measurement Science and Technology*, *22*(1), 015401.
33. Koschwanez, John H., Robert H. Carlson, and Deirdre R. Meldrum. "Thin PDMS films using long spin times or tert-butyl alcohol as a solvent." *PLoS one* 4, no. 2 (2009): e4572.
34. Bahrami, M., Yovanovich, M. M., & Culham, J. R. (2005, January). Pressure drop of fully-developed, laminar flow in microchannels of arbitrary cross-section. In *International Conference on Nanochannels, Microchannels, and Minichannels* (Vol. 41855, pp. 269-280).
35. Karadimitriou, N. K., Hassanizadeh, S. M., Joekar-Niasar, V., & Kleingeld, P. J. (2014). Micromodel study of two-phase flow under transient conditions: Quantifying effects of specific interfacial area. *Water Resources Research*, *50*(10), 8125-8140.
36. Roriz, P., Frazão, O., Lobo-Ribeiro, A. B., Santos, J. L., & Simões, J. A. (2013). Review of fiber-optic pressure sensors for biomedical and biomechanical applications. *Journal of biomedical optics*, *18*(5), 050903.
37. Urban, F., Kadlec, J., Vlach, R., & Kuchta, R. (2010). Design of a pressure sensor based on optical fiber Bragg grating lateral deformation. *Sensors*, *10*(12), 11212-11225.
38. Liu, Y., Jing, Z., Li, R., Zhang, Y., Liu, Q., Li, A., ... & Peng, W. (2020). Miniature fiber-optic tip pressure sensor assembled by hydroxide catalysis bonding technology. *Optics express*, *28*(2), 948-958.
39. Zarikos, I. M., Hassanizadeh, S. M., van Oosterhout, L. M., & van Oordt, W. (2018). Manufacturing a micro-model with integrated fibre optic pressure sensors. *Transport in porous media*, *122*(1), 221-234.

APPENDICES

APPENDIX A

PROFILOMETER IMAGES FOR THE CHANNEL DIMENSIONS

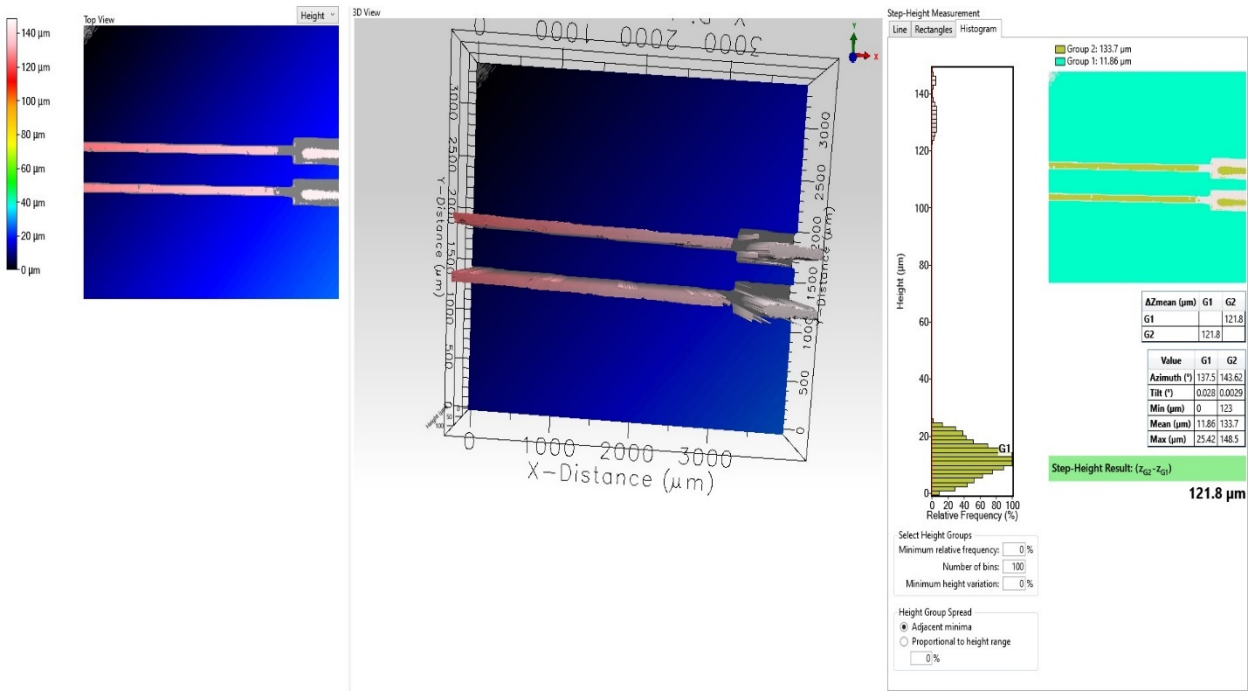

Figure A.1. Profilometer measurement for height of the microchannel, which was 121.8 µm

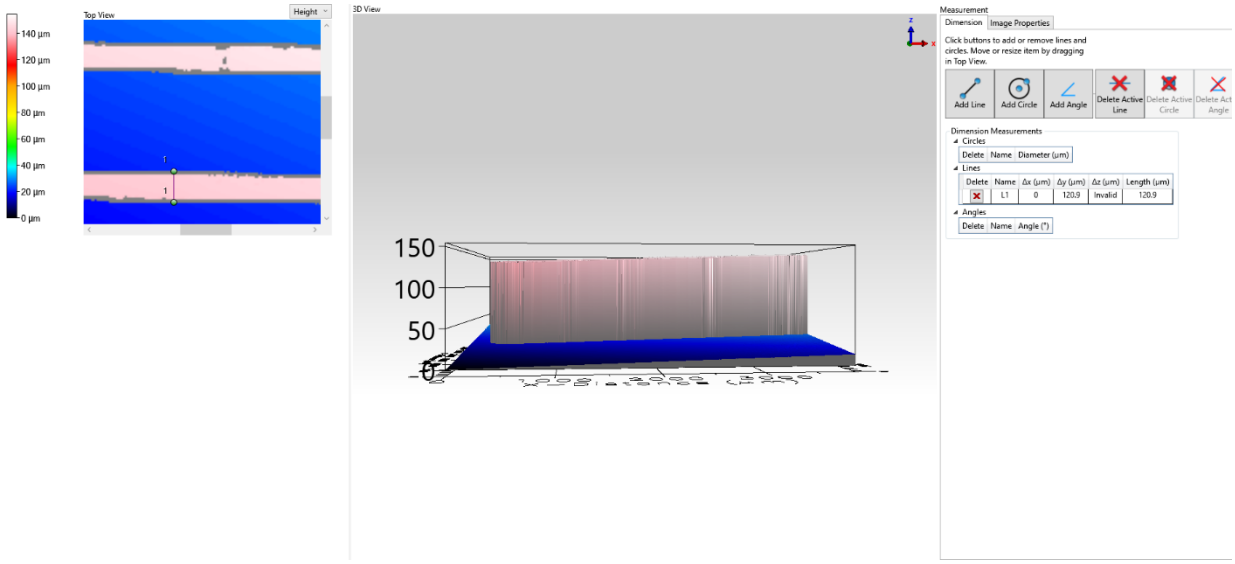

Figure A.2. Profilometer measurement for width of the microchannel, which was 120.9 µm

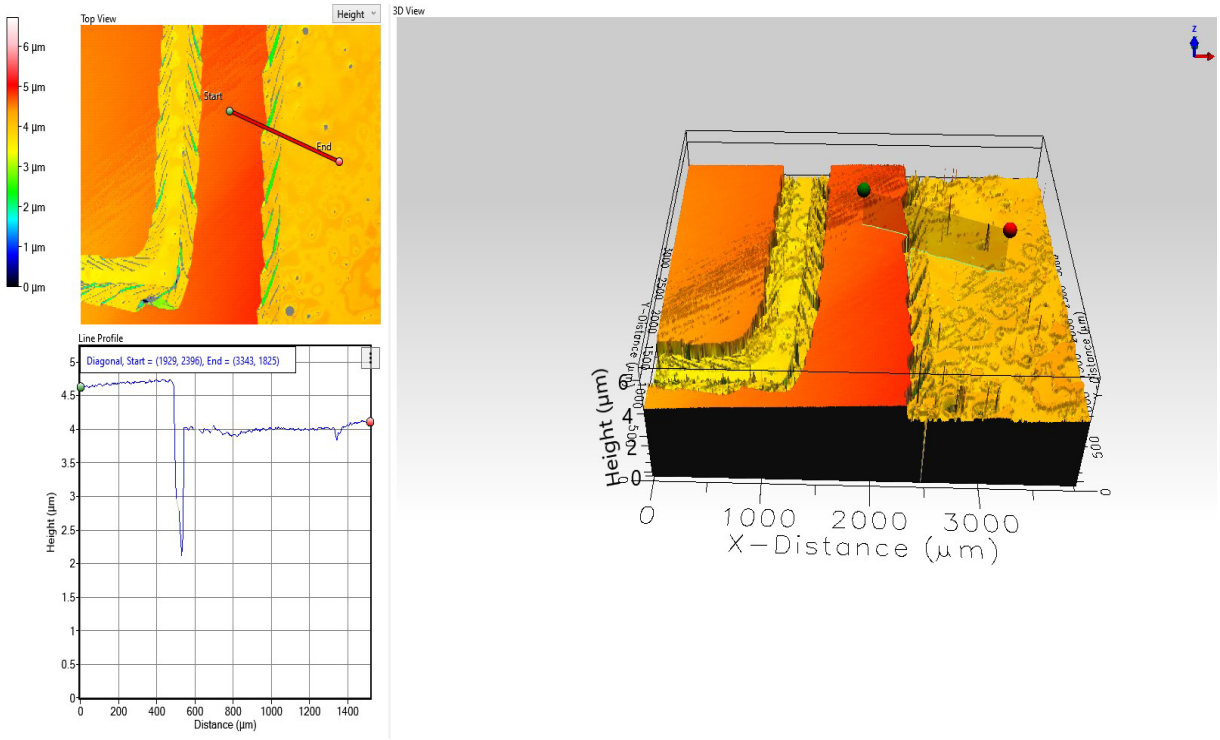

Figure A.3. Profilometer measurement for thickness of the membrane, which turns out to have a uniform thickness of 4.76 µm

APPENDIX B

MATLAB IMAGE COMPARISON CODE USED FOR CALIBRATION

```
%This program is to process astigmatism PIV. By performing
%cross-correlation between the calibrated Postion data and calibrated
%pressure data, find the relation between Deflection and pressure. Simply,
%for each preset pressure, find the corresponding deflection.

% clc
% clear all
%%%%%%%%%%%%%%%%%%%%%%%%%%%%%%%%%%%%%%%%%%%%%%%%%%%%%%%%%%%%%%%%%%%%%%%%%%%
%File Information
%%%%%%%%%%%%%%%%%%%%%%%%%%%%%%%%%%%%%%%%%%%%%%%%%%%%%%%%%%%%%%%%%%%%%%%%%%%

Rin='F:\Experiments\Nishagar\200 um PT - Design 5\06172021\Calibration';

[s1]=mkdir([Rin,'\Output Results']);

ROI = readtable([Rin,'\MatlabInput.xlsx']);

Show=1; %set to 1 to turn on plots

%Find the same particle in the position calibration images and the pressure

%calibration image

Port='Upper'; %specify the port

switch Port

    case 'Upper'

        %Location of Particle 1
        % %Postion calibration images, make it slight bigger than the
Pressure calibration image in order to do normalized cross correlation.


        %Location of Particle

        Position=ROI{:,1};
        Pressure=ROI{:,2};

    case 'Lower'
        %Location of Particle

        Position=ROI{:,3};
        Pressure=ROI{:,4};

end
```

```
[Height,Text1]=xlsread([Rin,'\Raw Data Pressure
Calibration\PressureCali.xlsx']);
PressureHead=Height(:,4);

[PositionCali,Text2]=xlsread([Rin,'\Raw Data Position
Calibration\PositionCali.xlsx']);

No_Pressure=length(PressureHead);
No_Position=size(PositionCali,1);

MemPosition=zeros(1,No_Pressure);

for i=1:1:No_Pressure
    %Read in image
    CineNamePressure=['Exp',num2str(i-1)];
    CineFilePressure=[Rin,'\Raw Data Pressure
Calibration\',CineNamePressure,'.cine'];
    fid1 = fopen(CineFilePressure, 'r');

    disp('-------------------------------------------------');
    disp(['Pressure Images: Exp', num2str(i-1)]);
    [CurrIm]=double(ReadCineImage(fid1, 1)); %only use the first image for
now
ImPPre=CurrIm(Pressure(2)+1:Pressure(2)+Pressure(4),Pressure(1)+1:Pressure(1)
+Pressure(3));

    if Show==1
        figure(1);
        imshow(uint8(ImPPre));
        title(['Pressure Images: ', CineNamePressure]);

    end

    PositionValues=0:1:No_Position-1;
    PeakValues=zeros(1,No_Position);

    for j=1:1:No_Position %read in the position calibration image
        CineNamePos=[num2str(j-1)];
        CineFilePos=[Rin,'\Raw Data Position
Calibration\',CineNamePos,'.cine'];
        fid2 = fopen(CineFilePos, 'r');
        %         disp('-------------------------------------------------
');
        %         disp(['Position Images: ', num2str(j-1)]);
        [CurrIm]=double(ReadCineImage(fid2, 1)); %only use the first image
for now


ImPosition=CurrIm(Position(2)+1:Position(2)+Position(4),Position(1)+1:Positio
n(1)+Position(3));

        if Show==1
```

```
            figure(2);
            imshow(uint8(ImPosition));
            title(['Position Images: ', CineNamePos]);

        end

        C=normxcorr2(ImPPre,ImPosition);
        CPeak=max(C(:));
        PeakValues(j)=CPeak;



        fclose(fid2);

    end
    figure(3), plot(PositionValues, PeakValues, 'ro-');
    ylim([0,1]);
    [BestMatchIndex] = find(PeakValues==max(PeakValues));
    if BestMatchIndex==1||BestMatchIndex==length(PeakValues)
        MemPosition(i)=PositionValues(BestMatchIndex);
    else
        p = polyfit(PositionValues(BestMatchIndex-
1:BestMatchIndex+1),PeakValues(BestMatchIndex-1:BestMatchIndex+1),2);
        MemPosition(i)=-p(2)/(2*p(1));
    end

    fclose(fid1);

end

P=PressureHead*1000*9.8/100;
xlswrite([Rin,'\Output Results\Pressure-Deflection_',Port,
'.xlsx'],[{'Deflection(um)','Head(cm)','P(Pa)'}; num2cell([MemPosition',
PressureHead, P])])
xlswrite([Rin,'\Output Results\Pressure-Deflection_',Port,
'ROI.xlsx'],[{'Position','Pressure'}; num2cell([Position, Pressure])])
```

APPENDIX C

MATLAB IMAGE COMPARISON CODE USED FOR FLOWRATE

```
%This program is to process astigmatism PIV. By performing
%cross-correlation between the calibrated Postion data and calibrated
%pressure data, find the relation between Deflection and pressure. Simply,
%for each preset pressure, find the corresponding deflection.

% clc
% clear all
%%%%%%%%%%%%%%%%%%%%%%%%%%%%%%%%%%%%%%%%%%%%%%%%%%%%%%%%%%%%%%%%%%%%%%%%
%File Information
%%%%%%%%%%%%%%%%%%%%%%%%%%%%%%%%%%%%%%%%%%%%%%%%%%%%%%%%%%%%%%%%%%%%%%%%

rin1='F:\Experiments\Nishagar\200 um PT - Design 5\06182021\2nd model
Calibration';
rin2='F:\Experiments\Nishagar\200 um PT - Design 5\06182021\Single-Phase
flow';

[s1]=mkdir([rin2,'\Output Results-Air with PT']);

ROI = readtable([rin2,'\MatlabInput.xlsx']);

Show=1; %set to 1 to turn on plots

NStart=1;
NEnd=100;

%Find the same particle in the position calibration images and the pressure
%calibration image

Port='Lower'; %specify the port

switch Port
    case 'Upper'
        %Location of Particle 1
        % %Postion calibration images, make it slight bigger than the
Pressure calibration image in order to do normalized calibration.

        %Location of Particle

        Position=ROI{:,7};
        Flow=ROI{:,8};                    %flow image upstream

    case 'Lower'
        %Location of Particle
        Position=ROI{:,9};
        Flow=ROI{:,10};                    %flow image downstream
end

[Flowsize,Text1]=xlsread([rin2,'\Air Pressure\FlowData.xlsx']);
Flowrate=Flowsize(:,2);
```

```
[PositionCali,Text2]=xlsread([rin1,'\Raw Data Position
Calibration\PositionCali.xlsx']);

No_Flowrate= length(Flowrate);
FlowImageName=zeros(1,No_Flowrate);

No_Position=size(PositionCali,1);

MemPosition=zeros(1,No_Flowrate);
Count=0;

for i=1:1:No_Flowrate
    Count=Count+1;
    %Read in image
    CineNameFlow=['Exp',num2str(i-1)];
    CineFileFlow=[rin2,'\Air Pressure\',CineNameFlow,'.cine'];
    fid1 = fopen(CineFileFlow, 'r');

    disp('-------------------------------------------------');
    disp(['Flowrate Images: Exp', num2str(i-1)]);
    [CurrIm]=double(ReadCineImage(fid1, 1)); %only use the first image for
now
    ImPRFlow=CurrIm(Flow(2)+1:Flow(2)+Flow(4),Flow(1)+1:Flow(1)+Flow(3));
    if Show==1
        figure(1);
        imshow(uint8(ImPRFlow));
        title(['Particle: ', CineNameFlow]);
    end


    PositionValues=0:1:No_Position-1;
    PeakValues=zeros(1,No_Position);

    for j=1:1:No_Position         %read in the position calibration image
        CineNamePos=[num2str(j-1)];
        CineFilePos=[rin1,'\Raw Data Position
Calibration\',CineNamePos,'.cine'];
        fid2 = fopen(CineFilePos, 'r');

        %         disp('-------------------------------------------------
');
        %         disp(['Position Images: ', num2str(j-1)]);
        [CurrIm]=double(ReadCineImage(fid2, 1)); %only use the first image
for now

ImPRPos=CurrIm(Position(2)+1:Position(2)+Position(4),Position(1)+1:Position(1
)+Position(3));

        if Show==1
            figure(2);
            imshow(uint8(ImPRPos));
            title(['Particle: ', CineNamePos]);
```

```
        end
        C=normxcorr2(ImPRFlow,ImPRPos);
        CPeak=max(C(:));
        PeakValues(j)=CPeak;

        fclose(fid2);

    end
    figure(3), plot(PositionValues, PeakValues, 'ro-');
    title(['Particle 2: ', CineNameFlow]);

    ylim([0,1]);
    [BestMatchIndex] = find(PeakValues==max(PeakValues));
    if BestMatchIndex==1||BestMatchIndex==length(PeakValues)
        MemPosition(Count)=PositionValues(BestMatchIndex);
    else
        p = polyfit(PositionValues(BestMatchIndex-
1:BestMatchIndex+1),PeakValues(BestMatchIndex-1:BestMatchIndex+1),2);
        MemPosition(Count)=-p(2)/(2*p(1));
    end

    FlowImageName(Count)=i;
    fclose(fid1);
end

% P=PressureHead*1000*9.8/100;
xlswrite([rin2,'\Output Results-Air with PT\Flowrate-Deflection_',Port,
'.xlsx'],[{'FlowImageName','MemPosition(um)','Flowrate'};num2cell([FlowImageN
ame',MemPosition',Flowrate])])
xlswrite([rin2,'\Output Results-Air with PT\Flowrate-Deflection_',Port,
'ROI.xlsx'],[{'Position','Flowrate'}; num2cell([Position, Flow])])
```

APPENDIX D

UNCERTAINITY ANALYSIS FOR SINGLE PHASE FLOW- AIR

	A	B	C	D	E	F	G	H
1	Deflectic	Head(cn	P(Pa)	Corrected Deflectic	P (kPa)	P_fitted	Error	
2	3.5903	0	0	0	0	0	0	
3	9.7281	2.38	233.24	3.712844121	0.2332	0.1733	0.0035978	
4	11.334	3.38	331.24	5.318277154	0.3312	0.266	0.0042503	
5	13.222	4.38	429.24	7.206929429	0.4292	0.389	0.0016181	
6	14.644	5.2506	514.56	8.628920642	0.5146	0.4915	0.0005341	
7	15.854	5.8556	573.85	9.83907232	0.5739	0.5853	0.000131	
8	16.864	7.1712	702.78	10.84822221	0.7028	0.6682	0.0011931	
9	18.059	8.1213	795.88	12.04418831	0.7959	0.7721	0.0005675	
10	19.428	9.0419	886.1	13.41314764	0.8861	0.8982	0.0001474	
11	20.474	10.042	984.1	14.45909494	0.9841	0.9999	0.0002509	
12	21.425	10.952	1073.3	15.40952768	1.0733	1.0963	0.0005296	
13	22.169	11.952	1171.3	16.15334743	1.1713	1.1744	9.489E-06	
14	22.99	12.863	1260.5	16.97475275	1.2605	1.2633	7.682E-06	
15	23.617	13.863	1358.5	17.60201133	1.3585	1.3331	0.0006471	
16	24.71	14.813	1451.6	18.69444979	1.4516	1.4586	4.821E-05	
17	25.385	15.733	1541.8	19.3698537	1.5418	1.5386	1.024E-05	
18	26.418	16.733	1639.8	20.4025264	1.6398	1.6648	0.0006215	
19	27.454	17.604	1725.2	21.43859836	1.7252	1.7958	0.0049897	
20	27.91	18.604	1823.2	21.89498174	1.8232	1.8549	0.0010101	
21	28.587	19.474	1908.5	22.57198249	1.9085	1.9443	0.0012816	
22	29.074	20.474	2006.5	23.05888882	2.0065	2.0097	1.05E-05	
23	29.777	21.345	2091.8	23.7619604	2.0918	2.106	0.0002006	
24	30.695	22.345	2189.8	24.67970903	2.1898	2.2347	0.0020167	
25	31.275	23.216	2275.1	25.25994289	2.2751	2.3179	0.0018321	
26	31.765	24.136	2365.4	25.75002461	2.3654	2.3893	0.0005744	
27	32.056	25.136	2463.4	26.04109781	2.4634	2.4322	0.000971	
28	32.317	26.007	2548.7	26.30184425	2.5487	2.4709	0.0060488	
29	33.127	27.007	2646.7	27.11180807	2.6467	2.593	0.0028859	
30	33.851	27.878	2732	27.8361648	2.732	2.7044	0.0007597	
31	34.321	28.828	2825.1	28.30594346	2.8251	2.7779	0.0022268	
32	35.404	29.828	2923.1	29.38915557	2.9231	2.9508	0.0007699	
33								
34						RMSE=	0.0358049	kPa

Figure D.1. Error analysis of Pressure vs. deflection curve for downstream pressure tap

	A	B	C	D	E	F	G	H
1	Deflectic	Head(cn	P(Pa)	Correcte	P (kPa)	P_fitted		
2	3.771	0	0	0	0	0	0	
3	10.6	2.38	233.24	3.6665	0.2332	0.1755	0.0033	
4	12.535	3.38	331.24	5.6013	0.3312	0.2896	0.0017	
5	13.984	4.38	429.24	7.05	0.4292	0.3848	0.002	
6	15.358	5.2506	514.56	8.4238	0.5146	0.4827	0.001	
7	17.035	5.8556	573.85	10.101	0.5739	0.6125	0.0015	
8	18.135	7.1712	702.78	11.201	0.7028	0.7036	6E-07	
9	19.481	8.1213	795.88	12.548	0.7959	0.8217	0.0007	
10	20.494	9.0419	886.1	13.561	0.8861	0.9153	0.0008	
11	21.822	10.042	984.1	14.888	0.9841	1.0441	0.0036	
12	22.584	10.952	1073.3	15.651	1.0733	1.1212	0.0023	
13	23.016	11.952	1171.3	16.082	1.1713	1.1659	3E-05	
14	23.399	12.863	1260.5	16.465	1.2605	1.2061	0.003	
15	24.766	13.863	1358.5	17.832	1.3585	1.3546	2E-05	
16	25.399	14.813	1451.6	18.465	1.4516	1.4258	0.0007	
17	26.568	15.733	1541.8	19.634	1.5418	1.5617	0.0004	
18	27.408	16.733	1639.8	20.474	1.6398	1.6626	0.0005	
19	28.013	17.604	1725.2	21.079	1.7252	1.737	0.0001	
20	28.574	18.604	1823.2	21.64	1.8232	1.8073	0.0003	
21	29.107	19.474	1908.5	22.173	1.9085	1.8752	0.0011	
22	30.076	20.474	2006.5	23.142	2.0065	2.0017	2E-05	
23	30.788	21.345	2091.8	23.854	2.0918	2.097	3E-05	
24	31.311	22.345	2189.8	24.377	2.1898	2.1683	0.0005	
25	31.991	23.216	2275.1	25.057	2.2751	2.2625	0.0002	
26	32.709	24.136	2365.4	25.775	2.3654	2.364	2E-06	
27	33.448	25.136	2463.4	26.514	2.4634	2.4707	5E-05	
28	34.193	26.007	2548.7	27.259	2.5487	2.5803	0.001	
29	34.46	27.007	2646.7	27.527	2.6467	2.6203	0.0007	
30	35.407	27.878	2732	28.474	2.732	2.7639	0.001	
31	35.784	28.828	2825.1	28.851	2.8251	2.8221	9E-06	
32	36.317	29.828	2923.1	29.384	2.9231	2.9053	0.0003	
33								
34						RSME	0.0294	kPa

Figure D.2. Error analysis of Pressure vs. deflection curve for upstream pressure tap

	A	B	C	D	E	F	G	H	I	J	K
1							Error Propagation				
2	FlowImag	MemPosit	Flowrate	Corrected Deflection	P (kPa)		Deflection	P (kPa)	P difference	Combined Error (Pa)	
3	1	2.330149	0	0	0		0.5	0.01997	0.019969973	0.040997	
4	2	1.884057	0.1	-0.446091949	-0.01693		0.053908051	0.002103	0.019036289	0.040551	
5	3	2.012428	0.2	-0.317721209	-0.01215		0.182278791	0.007159	0.019304972	0.040678	
6	4	2.093347	0.3	-0.236802176	-0.00909		0.263197824	0.010382	0.019474338	0.040758	
7	5	2.143448	0.4	-0.186701555	-0.00719		0.313298445	0.012391	0.019579201	0.040809	
8	6	2.219752	0.5	-0.110397385	-0.00427		0.389602615	0.015471	0.019738907	0.040885	
9	7	2.222996	0.6	-0.107152832	-0.00414		0.392847168	0.015602	0.019745698	0.040889	
10	8	2.32271	0.7	-0.00743964	-0.00029		0.49256036	0.019665	0.019954401	0.04099	
11	9	2.442718	0.8	0.112568611	0.004405		0.612568611	0.02461	0.020205582	0.041113	
12	10	2.618367	0.9	0.288217604	0.011384		0.788217604	0.031957	0.020573221	0.041295	
13	11	2.617796	1	0.287646466	0.011361		0.787646466	0.031933	0.020572025	0.041294	
14	12	2.617796	1.1	0.287646466	0.011361		0.787646466	0.031933	0.020572025	0.041294	
15	13	2.712149	1.2	0.381999978	0.015163		0.881999978	0.035932	0.02076951	0.041393	
16	14	2.760163	1	0.430013196	0.017112		0.930013196	0.037982	0.020870003	0.041443	
17	15	2.80752	0.8	0.477370201	0.019044		0.977370201	0.040013	0.020969123	0.041493	
18	16	2.710609	0.6	0.380459568	0.0151		0.880459568	0.035867	0.020766286	0.041391	
19	17	2.719845	0.4	0.389695646	0.015474		0.889695646	0.03626	0.020785617	0.041401	
20	18	2.723342	0.2	0.393192788	0.015616		0.893192788	0.036409	0.020792937	0.041405	
21	19	2.708427	0	0.37827769	0.015012		0.87827769	0.035774	0.020761719	0.041389	
22											

Figure D.3. Error analysis of Pressure drop vs. flowrate for downstream pressure tap

	A	B	C	D	E	F	G	H	I	J	K
1							Error Propagation				
2	FlowImag	MemPosit	Flowrate	Corrected Deflection	P (kPa)_Upper		Deflectior	P (kPa)	P difference	Combined Error (Pa)	
3	1	3.052381	0	0	0		0.5	0.020795	0.020794688	0.036011	
4	2	4.685955	0.1	1.63357481	0.071612045		2.133575	0.095647	0.024034605	0.037974	
5	3	6.453034	0.2	3.400653386	0.160994848		3.900653	0.188534	0.027539305	0.040284	
6	4	8.127493	0.3	5.075112222	0.257122097		5.575112	0.287982	0.03086031	0.042623	
7	5	9.656398	0.4	6.604017879	0.354607077		7.104018	0.3885	0.033892634	0.044867	
8	6	11.10378	0.5	8.051401934	0.455437993		8.551402	0.492201	0.036763274	0.047073	
9	7	12.34804	0.6	9.295656915	0.548760417		9.795657	0.587991	0.039231043	0.049025	
10	8	13.91371	0.7	10.86132704	0.674915322		11.36133	0.717252	0.042336283	0.051543	
11	9	14.68325	0.8	11.6308698	0.740485874		12.13087	0.784348	0.043862541	0.052804	
12	10	16.17132	0.9	13.11894291	0.873943348		13.61894	0.920757	0.046813881	0.05528	
13	11	16.918	1	13.86561541	0.944217919		14.36562	0.992513	0.048294779	0.05654	
14	12	17.688	1.1	14.63561541	1.019004212		15.13562	1.068826	0.049821943	0.05785	
15	13	18.79615	1.2	15.74377185	1.130761856		16.24377	1.182782	0.052019783	0.059753	
16	14	17.00632	1	13.95394197	0.952677225		14.45394	1.001147	0.048469959	0.05669	
17	15	15.2233	0.8	12.17092143	0.787904846		12.67092	0.832838	0.044933641	0.053697	
18	16	13.1249	0.6	10.07252334	0.610141568		10.57252	0.650913	0.040771825	0.050266	
19	17	9.992232	0.4	6.939851915	0.377262332		7.439852	0.411821	0.034558704	0.045373	
20	18	7.062946	0.2	4.010565018	0.194720888		4.510565	0.22347	0.028748961	0.04112	
21	19	3.536039	0	0.483658413	0.020099375		0.983658	0.041853	0.021753942	0.036573	
22											

Figure D.4. Error analysis of Pressure drop vs. flowrate for upstream pressure tap

	A	B	C	D	E	F	G	H	I	J	K	L	M	N
1				L [m]	w [m]	h [m]	Dh [m]	mu [Pa-s]						
2				0.0196	0.00012	1.23E-04	1.21E-04	0.0000186						
3														
4	Flowrate (ml/min)	Flowrate (m^3/s)	Theoretical P (kPa)	Flowrate error	U_P_Flow	h error	U_P_h	w error	U_P_w	L error	U_P_L	Combined error		% error
5	0	0	0.000000	0	0.000000	1.24E-04	0.000000	0.0001201	0.000000	0.0197	0.000000	0		0
6	0.1	1.66667E-09	0.079875	1.73333E-09	0.003195		-0.001099		-0.000796		0.000399	0.00349		4.37458
7	0.2	3.33333E-09	0.159749	3.46667E-09	0.006390		-0.002198		-0.001592		0.000799	0.00699		4.37458
8	0.3	0.000000005	0.239624	5.2E-09	0.009585		-0.003298		-0.002388		0.001198	0.01048		4.37458
9	0.4	6.66667E-09	0.319498	6.93333E-09	0.012780		-0.004397		-0.003184		0.001597	0.01398		4.37458
10	0.5	8.33333E-09	0.399373	8.66667E-09	0.015975		-0.005496		-0.003980		0.001997	0.01747		4.37458
11	0.6	0.00000001	0.479247	1.04E-08	0.019170		-0.006595		-0.004776		0.002396	0.02097		4.37458
12	0.7	1.16667E-08	0.559122	1.21333E-08	0.022365		-0.007695		-0.005572		0.002796	0.02446		4.37458
13	0.8	1.33333E-08	0.638997	1.38667E-08	0.025560		-0.008794		-0.006368		0.003195	0.02795		4.37458
14	0.9	0.000000015	0.718871	1.56E-08	0.028755		-0.009893		-0.007164		0.003594	0.03145		4.37458
15	1	1.66667E-08	0.798746	1.73333E-08	0.031950		-0.010992		-0.007960		0.003994	0.03494		4.37458
16	1.1	1.83333E-08	0.878620	1.90667E-08	0.035145		-0.012091		-0.008756		0.004393	0.03844		4.37458
17	1.2	0.00000002	0.958495	2.08E-08	0.038340		-0.013191		-0.009552		0.004792	0.04193		4.37458
18	1	1.66667E-08	0.798746	1.73333E-08	0.031950		-0.010992		-0.007960		0.003994	0.03494		4.37458
19	0.8	1.33333E-08	0.638997	1.38667E-08	0.025560		-0.008794		-0.006368		0.003195	0.02795		4.37458
20	0.6	0.00000001	0.479247	1.04E-08	0.019170		-0.006595		-0.004776		0.002396	0.02097		4.37458
21	0.4	6.66667E-09	0.319498	6.93333E-09	0.012780		-0.004397		-0.003184		0.001597	0.01398		4.37458
22	0.2	3.33333E-09	0.159749	3.46667E-09	0.006390		-0.002198		-0.001592		0.000799	0.00699		4.37458
23	0	0	0.000000	0	0.000000		0.000000		0.000000		0.000000	0		0

Figure D.5. Error propagation from theoretical calculation of rectangular channel

A	B	C	D	E	F	G	H	I	J	K	L	M	N	O	P	Q	R	S	T	U	V
Flowrate	Flowrate (ml/min)		P (kPa)_Uppe	Error (kPa)		P (kPa)_Lowe	Error (kPa)		Delta P (kPa	Error (kPa)		Theoretical P (kPa)	Error	Theoretical P - Error	Theoretical P +Error		PT (kPa)	Error	PT correction (kPa)		
0	0		0	0.036		0	0.041		0	0.0546		0.000000	0.000000	0.000000	0.000000		0	0.0345	0	0.000000	
2E-09	0.1		0.07161204	0.038		-0.0169335	0.0406		0.0885456	0.0556		0.079875	0.003494	0.076380	0.083369		0.0925	0.0345	0.109	0.000418	
3E-09	0.2		0.16099485	0.0403		-0.012146	0.0407		0.1731408	0.0572		0.159749	0.006988	0.152761	0.166738		0.1771	0.0345	0.2086	0.001259	
5E-09	0.3		0.2571221	0.0426		-0.0090927	0.0408		0.2662148	0.059		0.239624	0.010483	0.229141	0.250106		0.2604	0.0345	0.3069	0.001654	
7E-09	0.4		0.35460708	0.0449		-0.0071885	0.0408		0.3617956	0.0606		0.319498	0.013977	0.305522	0.333475		0.3398	0.0345	0.4004	0.001491	
8E-09	0.5		0.45543799	0.0471		-0.0042682	0.0409		0.4597062	0.0624		0.399373	0.017471	0.381902	0.416844		0.4225	0.0345	0.4978	0.001453	
1E-08	0.6		0.54876042	0.049		-0.0041435	0.0409		0.5529039	0.0638		0.479247	0.020965	0.458282	0.500213		0.499	0.0345	0.5879	0.001228	
1E-08	0.7		0.67491532	0.0515		-0.0002892	0.041		0.6752046	0.0659		0.559122	0.024459	0.534663	0.583581		0.5929	0.0345	0.6986	0.000548	
1E-08	0.8		0.74048587	0.0528		0.0044047	0.0411		0.7360812	0.0669		0.638997	0.027953	0.611043	0.666950		0.6333	0.0345	0.7462	0.000102	
2E-08	0.9		0.87394335	0.0553		0.01138364	0.0413		0.8625597	0.069		0.718871	0.031448	0.687424	0.750319		0.7169	0.0345	0.8447	0.000320	
2E-08	1		0.94421792	0.0565		0.01136074	0.0413		0.9328572	0.07		0.798746	0.034942	0.763804	0.833688		0.7979	0.0345	0.9402	0.000053	
2E-08	1.1		1.01900421	0.0578		0.01136074	0.0413		1.0076435	0.0711		0.878620	0.038436	0.840184	0.917056		0.8713	0.0345	1.0267	0.000361	
2E-08	1.2		1.13076186	0.0598		0.01516271	0.0414		1.1155391	0.0727		0.958495	0.041930	0.916565	1.000425		0.9543	0.0345	1.1245	0.000079	
2E-08	1		0.95267723	0.0567		0.01711171	0.0414		0.9355655	0.0702							0.8036	0.0345	0.9469	0.000123	
1E-08	0.8		0.78790485	0.0537		0.01904353	0.0415		0.7688613	0.0679							0.6427	0.0345	0.7573	0.000134	
1E-08	0.6		0.61014157	0.0503		0.01510034	0.0414		0.5950412	0.0651							0.4949	0.0345	0.5832	0.000141	
7E-09	0.4		0.37726233	0.0454		0.01547445	0.0414		0.3617879	0.0614							0.3514	0.0345	0.4141	0.002734	
3E-09	0.2		0.19472089	0.0411		0.0156162	0.0414		0.1791047	0.0584							0.202	0.0345	0.238	0.003466	
0	0		0.02009938	0.0366		0.01501202	0.0414		0.0050874	0.0552							0.0502	0.0345	0.0592	0.002928	
									RSME	0.2525										0.026263	

Figure D.6. Uncertainty analysis of pressure drop vs. flowrate for Air

APPENDIX E

UNCERTAINITY ANALYSIS FOR SINGLE PHASE FLOW- DI WATER

	A	B	C	D	E	F	G	H	I	J	K
1							Error Propagation				
2	FlowImag	MemPosit	Flowrate	Corrected	P (kPa)		Deflectior	P (kPa)	P differen	Combined	Error (Pa)
3	1	6.718658	0	0	0		0.5	0.01997	0.01997	0.040997	
4	2	6.914889	0.001	0.196231	0.007713		0.696231	0.028093	0.020381	0.041199	
5	3	7.070238	0.002	0.351581	0.013933		0.851581	0.034639	0.020706	0.041361	
6	4	7.296015	0.003	0.577358	0.023153		1.077358	0.044332	0.021178	0.0416	
7	5	7.360041	0.004	0.641383	0.025807		1.141383	0.047119	0.021312	0.041668	
8	6	7.382041	0.005	0.663383	0.026722		1.163383	0.048081	0.021358	0.041691	
9	7	7.369382	0.006	0.650724	0.026195		1.150724	0.047527	0.021332	0.041678	
10	8	9.598336	0.007	2.879678	0.129357		3.379678	0.155354	0.025997	0.044248	
11	9	7.234926	0.008	0.516268	0.020637		1.016268	0.041688	0.021051	0.041535	
12	10	7.394999	0.009	0.676341	0.027263		1.176341	0.048648	0.021386	0.041705	
13	11	7.298074	0.01	0.579416	0.023238		1.079416	0.044421	0.021183	0.041602	
14	12	7.181138	0.011	0.46248	0.018435		0.96248	0.039373	0.020938	0.041478	
15	13	7.73291	0.012	1.014252	0.041601		1.514252	0.063694	0.022093	0.042072	
16	14	7.657441	0.01	0.938784	0.038357		1.438784	0.060292	0.021935	0.04199	
17	15	7.554438	0.008	0.83578	0.033968		1.33578	0.055688	0.021719	0.041877	
18	16	7.616363	0.006	0.897705	0.036602		1.397705	0.05845	0.021849	0.041945	
19	17	7.471438	0.004	0.752781	0.030464		1.252781	0.05201	0.021546	0.041788	
20	18	7.520673	0.002	0.802015	0.032539		1.302015	0.054188	0.021649	0.041841	
21	19	7.402403	0	0.683745	0.027572		1.183745	0.048973	0.021401	0.041713	
22											

Figure E.1. Error analysis of Pressure drop vs. flowrate for downstream pressure tap

	A	B	C	D	E	F	G	H	I	J	K
1							Error Propagation				
2	FlowImag	MemPosit	Flowrate	Corrected	P (kPa)_Upper		Deflection	P (kPa)	P difference	Combined	Error (Pa)
3	1	8.084756	0	0	0		0.5	0.020794688	0.020794688	0.036011	
4	2	9.24577	0.001	1.161014	0.049808		1.661013606	0.072905289	0.023097361	0.037388	
5	3	10.24126	0.002	2.156502	0.096773		2.656502062	0.121844266	0.025071743	0.038639	
6	4	11.95753	0.003	3.872775	0.186973		4.372774936	0.21544822	0.028475678	0.04093	
7	5	13.12602	0.004	5.041266	0.255069		5.541266472	0.285862135	0.030793183	0.042574	
8	6	13.71835	0.005	5.633596	0.291657		6.133596096	0.323624816	0.031967968	0.043432	
9	7	14.92105	0.006	6.836296	0.370229		7.336296168	0.404582107	0.034353319	0.045216	
10	8	16.61572	0.007	8.530959	0.490679		9.030959405	0.528393151	0.037714395	0.04782	
11	9	16.99667	0.008	8.911909	0.519323		9.411909444	0.557793353	0.038469945	0.048418	
12	10	17.33065	0.009	9.245891	0.54491		9.745891169	0.584042296	0.039132341	0.048946	
13	11	18.30118	0.01	10.21643	0.621774		10.71642581	0.662831499	0.041057231	0.050498	
14	12	18.98364	0.011	10.89888	0.678061		11.39888091	0.720471425	0.042410765	0.051605	
15	13	19.97625	0.012	11.89149	0.763225		12.39149	0.807604504	0.044379436	0.053234	
16	14	18.64659	0.01	10.56184	0.650032		11.06183699	0.691773914	0.041742296	0.051057	
17	15	16.68182	0.008	8.597068	0.495608		9.097068485	0.533453905	0.037845511	0.047923	
18	16	14.85324	0.006	6.768483	0.365646		7.268482975	0.399864763	0.034218823	0.045114	
19	17	13.32591	0.004	5.241155	0.26726		5.741155245	0.298450025	0.031189628	0.042862	
20	18	11.19719	0.002	3.112438	0.145571		3.61243771	0.172538572	0.026967679	0.039895	
21	19	8.424693	0	0.339937	0.01403		0.839936717	0.035498734	0.021468894	0.036404	
22											

Figure E.2. Error analysis of Pressure drop vs. flowrate for upstream pressure tap

	A	B	C	D	E	F	G	H	I	J	K	L	M	N
1				L [m]	w [m]	h [m]	Dh [m]	mu [Pa-s]						
2				0.0196	0.00012	1.23E-04	1.21E-04	0.0010016						
3														
4	Flowrate (ml/min)	Flowrate (m^3/s)	Theoretical P (kPa)	Flowrate error	U_P_Flow	h error	U_P_h	w error	U_P_w	L error	U_P_L	Combined error		% error
5	0	0	0.000000	0	0.000000	1.24E-04	0.000000	0.0001201	0.000000	0.0197	0.000000	0		0
6	0.001	1.66667E-11	0.043012	1.73333E-11	0.001720		-0.000592		-0.000429		0.000215	0.00188		4.37458
7	0.002	3.33333E-11	0.086024	3.46667E-11	0.003441		-0.001184		-0.000857		0.000430	0.00376		4.37458
8	0.003	5E-11	0.129036	5.2E-11	0.005161		-0.001776		-0.001286		0.000645	0.00564		4.37458
9	0.004	6.66667E-11	0.172048	6.93333E-11	0.006882		-0.002368		-0.001715		0.000860	0.00753		4.37458
10	0.005	8.33333E-11	0.215060	8.66667E-11	0.008602		-0.002960		-0.002143		0.001075	0.00941		4.37458
11	0.006	1E-10	0.258072	1.04E-10	0.010323		-0.003552		-0.002572		0.001290	0.01129		4.37458
12	0.007	1.16667E-10	0.301084	1.21333E-10	0.012043		-0.004143		-0.003000		0.001505	0.01317		4.37458
13	0.008	1.33333E-10	0.344096	1.38667E-10	0.013764		-0.004735		-0.003429		0.001720	0.01505		4.37458
14	0.009	1.5E-10	0.387108	1.56E-10	0.015484		-0.005327		-0.003858		0.001936	0.01693		4.37458
15	0.01	1.66667E-10	0.430120	1.73333E-10	0.017205		-0.005919		-0.004286		0.002151	0.01882		4.37458
16	0.011	1.83333E-10	0.473132	1.90667E-10	0.018925		-0.006511		-0.004715		0.002366	0.0207		4.37458
17	0.012	2E-10	0.516144	2.08E-10	0.020646		-0.007103		-0.005144		0.002581	0.02258		4.37458
18	0.01	1.66667E-10	0.430120	1.73333E-10	0.017205		-0.005919		-0.004286		0.002151	0.01882		4.37458
19	0.008	1.33333E-10	0.344096	1.38667E-10	0.013764		-0.004735		-0.003429		0.001720	0.01505		4.37458
20	0.006	1E-10	0.258072	1.04E-10	0.010323		-0.003552		-0.002572		0.001290	0.01129		4.37458
21	0.004	6.66667E-11	0.172048	6.93333E-11	0.006882		-0.002368		-0.001715		0.000860	0.00753		4.37458
22	0.002	3.33333E-11	0.086024	3.46667E-11	0.003441		-0.001184		-0.000857		0.000430	0.00376		4.37458
23	0	0	0.000000	0	0.000000		0.000000		0.000000		0.000000	0		0

Figure E.3. Error propagation from theoretical calculation of rectangular channel

	A	B	C	D	E	F	G	H	I	J	K	L	M	N	O	P	Q	R	S	T	U	V
1	FlowImag	MemPosi	Flowrate	Correcte	P (kPa)_Uppe	Error		P (kPa)_Lowe	Error		Delta P (kPa)	Error		Theoretical P (kPa	Error	Theoretical P- Erro	Theoretical P+ Error		PT (kPa)	Error	PT corrected (kPa)	
2	1	8.0848	0	0	0	0.036		0	0.041		0	0.0545672		0.000000	0.000000	0.000000	0.000000		0	0.0345	0	0
3	2	9.2458	0.001	1.161	0.04980793	0.0374		0.0077127	0.0412		0.0420952	0.0556347		0.043012	0.001882	0.041130	0.044894		0.0231	0.0345	0.0272	0.0002
4	3	10.241	0.002	2.1565	0.09677252	0.0386		0.0139329	0.0414		0.0828396	0.0566011		0.086024	0.003763	0.082261	0.089787		0.0449	0.0345	0.0529	0.0009
5	4	11.958	0.003	3.8728	0.18697254	0.0409		0.0231512	0.0416		0.1638194	0.0583588		0.129036	0.005645	0.123391	0.134681		0.1057	0.0345	0.1245	0.0015
6	5	13.126	0.004	5.0413	0.25506895	0.0426		0.0258061	0.0417		0.2292623	0.0595718		0.172048	0.007526	0.164522	0.179575		0.1334	0.0345	0.1572	0.0052
7	6	13.718	0.005	5.6336	0.23165685	0.0434		0.0267235	0.0417		0.2643345	0.0602038		0.215060	0.009408	0.205652	0.224468		0.1877	0.0345	0.2211	0.0019
8	7	14.321	0.006	6.8363	0.37022879	0.0452		0.0261918	0.0417		0.3440336	0.0614344		0.258072	0.011290	0.246783	0.269362		0.2375	0.0345	0.2798	0.0041
9	8	16.616	0.007	8.531	0.49067876	0.0478		0.1293712	0.0442		0.3613216	0.0651505		0.301084	0.013171	0.287913	0.314255		0.3995	0.0345	0.4707	0.012
10	9	16.997	0.008	8.9119	0.51932341	0.0484		0.0206373	0.0415		0.4986861	0.063792		0.344096	0.015053	0.329043	0.359149		0.4589	0.0345	0.5407	0.0018
11	10	17.331	0.009	9.2459	0.54490996	0.0489		0.0272626	0.0417		0.5176473	0.0643043		0.387108	0.016934	0.370174	0.404043		0.3801	0.0345	0.4479	0.0049
12	11	18.301	0.01	10.216	0.62177427	0.0505		0.0232386	0.0416		0.5985361	0.0654276		0.430120	0.018816	0.411304	0.448936		0.381	0.0345	0.4489	0.0224
13	12	18.984	0.011	10.899	0.67806066	0.0516		0.0184352	0.0415		0.6536255	0.0662075		0.473132	0.020698	0.452435	0.493830		0.4079	0.0345	0.4806	0.032
14	13	19.976	0.012	11.891	0.76322507	0.0532		0.0416086	0.0421		0.7216242	0.0678527		0.516144	0.022579	0.493565	0.538724		0.4352	0.0345	0.5127	0.0436
15	14	18.647	0.01	10.562	0.65003162	0.0511		0.0383574	0.042		0.6116745	0.0661054							0.3965	0.0345	0.4672	0.0209
16	15	16.682	0.008	8.5971	0.49560839	0.0479		0.0339683	0.0419		0.46164	0.0636425							0.3375	0.0345	0.3977	0.0041
17	16	14.853	0.006	6.7685	0.36564594	0.0451		0.0366156	0.0419		0.3290444	0.0616008							0.2858	0.0345	0.3367	6E-05
18	17	13.326	0.004	5.2412	0.2672604	0.0429		0.0304642	0.0418		0.2367961	0.0598612							0.1988	0.0345	0.2342	7E-06
19	18	11.197	0.002	3.1124	0.14557089	0.0399		0.0325394	0.0418		0.1130315	0.0578125							0.122	0.0345	0.1437	0.0009
20	19	8.4247	0	0.3399	0.01402984	0.0364		0.0275717	0.0417		-0.013542	0.055365							0.0203	0.0345	0.0239	0.0014
21																						
22											RSME	0.0612397										0.0912

Figure E.4. Uncertainty analysis of pressure drop vs. flowrate for DI water